

Editorial corner – a personal view

Pharmaceuticals prepared by continuous polymer technologies

Gy. Marosi*

Organic Chemistry and Technology Department of Budapest University of Technology and Economics, H-1111 Budapest, Műegyetem rkp. 3, Hungary

Accelerating convergence between the polymer and pharmaceutical technologies is one of the most exciting examples of the cross-fertilization tendencies within the materials science in the 21st century. The extended use of polymers and the composite structure in solid pharmaceuticals should have been induced it earlier but the conservative approach (based on safety arguments) of pharmacists hindered the spread of continuous processes in this field. The next decades will, however, bring about the technology of pharmaceutical plants getting closer to that of the plastic factories. The roots of this change, i.e. pharmaceuticals produced by extrusion and electrospinning, appeared already in the scientific literature and patents. The innovation in the pharmaceutical industry can be accelerated this way rather than by the expensive development of new drugs. The current task is to clarify the advantages of such interdisciplinary cooperation. The last step of the synthesis (crystallization) is expected, for example, to be integrated with continuous formulation processes in the pharmaceutical plant of the future. Positive feedbacks of this radical change to the plastic industry can be noticed already nowadays. Special types of polylactic acid, polyhydroxybutyrate and other biodegradable polymers, the larger scale application of which was hindered by economic reasons, have found substantial market share in the pharmaceutical industry. After recovery of the investment costs these polymers can spread out in the plastic industry in optimized and well-controlled way. The remaining task is the

development of specific functional properties, such as the fire retardancy. Investment in the supercritical extrusion is also expected for pharmaceuticals, the heat sensitivity of which needs this gentle technology badly. These developments, coupled with in-line process control (required by real time release) will provide very positive influence to the traditional plastic industry as well. In-line process control accompanied by total management and continuous development of the technology, called ‘Process Analytical Technology (PAT)’, need the application of recently developed advanced mathematical (chemometric) algorithms, which, on the other hand, have been proven to be very useful tools for spectroscopic identification and classification of components of mixed polymer wastes.



Prof. Dr. György Marosi
Member of International Advisory Board

*Corresponding author, e-mail: gmarosi@mail.bme.hu
© BME-PT

Novel macroporous amphoteric gels: Preparation and characterization

S. Kudaibergenov^{1,2*}, Zh. Adilov¹, D. Berillo², G. Tatykhanova^{1,2}, Zh. Sadakbaeva¹, Kh. Abdullin¹, I. Galaev³

¹Laboratory of Engineering Profile, Kazakh National Technical University n/a K.I. Satpaev, Satpaev str. 22, 050013, Almaty, Republic of Kazakhstan

²Institute of Polymer Materials and Technology, Panfilov Str. 52/105, 050004, Almaty, Republic of Kazakhstan

³DSM Food Specialties B.V., PO Box 1, 2600 MA Delft, The Netherlands

Received 4 July 2011; accepted in revised form 26 November 2011

Abstract. Macroporous amphoteric gels based on allylamine, methacrylic acid and acrylamide crosslinked by N,N'-methylenebisacrylamide were synthesized by radical copolymerization of monomers in cryoconditions. The composition of cryogels was determined by combination of potentiometric and conductimetric titrations. The morphology of cryogels was evaluated by scanning electron microscope (SEM). Cryogels exhibited sponge-like porous structure with pore size ranging from 50 to 200 μm . The values of the isoelectric points (IEPs) determined from the swelling experiments arranged between 3.5 and 4.3. The high adsorption-desorption capacity of amphoteric cryogels with respect to mM and trace concentrations of copper, nickel, and cobalt ions was demonstrated. It was shown that the macroporous amphoteric cryogels are able to adsorb up to 99.9% of copper, nickel, and cobalt ions from $10^{-3} \text{ mol} \cdot \text{L}^{-1}$ aqueous solution.

Keywords: polymer gels, smart polymers, macroporous amphoteric cryogels, morphology, swelling

1. Introduction

Hydrogels can be in the form of macroscopic networks or confined to smaller dimensions such as microgels, which are crosslinked polymeric particles [1]. When the size of microgels is in the submicron range, they are known as nanogels [2]. According to the IUPAC definition, materials having pores of larger than 50 nm are called macroporous [3]. However, recently much attention is paid to the materials with pore sizes between 1–100 microns, and beyond. Such polymers sometimes are called supermacroporous polymers. According to the cryopolymerization concept macroporous gels are formed in moderately frozen solutions of monomeric and/or polymeric precursors. Contrary to conventional gels in which solvent is retained within the volume, the cryogels are heterophase systems where

solvent resides both inside the interconnected macropores and is bound to the polymer network. Comprehensive information on the structure, properties and application of cryogels based on natural and synthetic polymers can be found in a review article [4]. Recently published fundamental book [5] describes both the pioneering articles devoted to cryogels and gives an up-to-date compilation of modes of production of macroporous hydrogels, characterization of such materials, and applications with regard to both biotechnology and biomedicine.

Synthetic amphoteric gels belong to 'smart' materials due to their response to temperature, pH, ionic strength, water-organic solvent composition, electric field, etc. [6, 7]. In the last years the most attention was paid to amphoteric nanogels [8–15] and microgels [16–20] however, to our knowledge, there

*Corresponding author, e-mail: ipmt-kau@usa.net

© BME-PT

is no any available information on macroporous amphoteric gels of synthetic origin. Amphoteric cryogels as distinct from nonionic, anionic and cationic macroporous materials consist of both acidic and basic monomers.

In the present communication we report for the first time the preparation protocol and characterization of amphoteric cryogels that will have potential applications for the encapsulation of cells, immobilization of enzymes, purification and separation of proteins, recovery of metal ions and as catalysts.

2. Experimental part

2.1. Materials

Monomers and initiators – acrylamide (AAm, 99% purity, from Sigma-Aldrich Chemical Co., Milwaukee, WI, USA), allylamine (AA, 99% purity, from Sigma-Aldrich Chemical Co., Milwaukee, WI, USA), methacrylic acid (MAA, 99% purity, from Sigma-Aldrich Chemical Co., Milwaukee, WI, USA), N,N,N',N'-tetramethylethylenediamine (TMED, 99% purity, from Sigma-Aldrich Chemical Co., Milwaukee, WI, USA), ammonium persulfate (APS, 99% purity), and crosslinking agent N,N'-methylenebisacrylamide (MBAA, 99% purity, from Sigma-Aldrich Chemical Co., Milwaukee, WI, USA) – were purchased from Aldrich and used without further purification.

2.2. Synthesis of amphoteric cryogels

A mixture of AA (66 mg or 1.15 mmol), MAA (99 mg or 1.15 mmol), AAm (660 mg or 9.3 mmol), MBAA (82 mg) corresponding to molar ratio of monomers AA:MAA:AAm = 10:10:80 mol%/mol%/mol% was dissolved in 9.7 mL of deionized water, flushed

by nitrogen for 10 min and degassed in vacuo for about 5 min to eliminate the dissolved oxygen. After addition of 10 μ L of TMED the solution was cooled in an ice bath for 4–5 min. Then 0.1 mL of aqueous solution of APS (10 wt%) preliminary cooled in an ice bath for 4–5 min was added and the reaction mixture was stirred for 1 min. The total volume of reaction mixture was divided into 10 parts and each part containing 1 mL of reaction mixture was placed into the 10 plastic syringes with diameter 5 mm with closed outlet at the bottom. The solution in syringe was frozen within 10 min at -12°C and was kept frozen during 48 h. After completion of the reaction the sample was thawed at room temperature. The prepared cryogel sample was washed out thoroughly by distilled water every 2–3 hours during several days then successively washed out by 25, 50, 75 and 96% ethanol to dehydrate then dried in air and finally in vacuum oven to constant mass at room temperature. The amount of monomers in initial feed (in mg and mol%) used for synthesis of cryogels with different molar ratio of monomers at constant concentration of MBAA (82 mg or 10 wt%) is given in Table 1.

Thus a series of amphoteric cryogels (ACG) with initial molar ratios of AA:MAA:AAm = 10:10:80;

Table 1. Amount of AA, MAA and AAm in the feed used for synthesis of cryogels

Initial monomer feed					
[mg]			[mol%]		
AA	MAA	AAm	AA	MAA	AAm
131.3	197.8	460.6	20	20	60
197.0	296.7	327.0	30	30	40
262.7	395.6	163.5	40	40	20
328.3	494.5	0	50	50	0

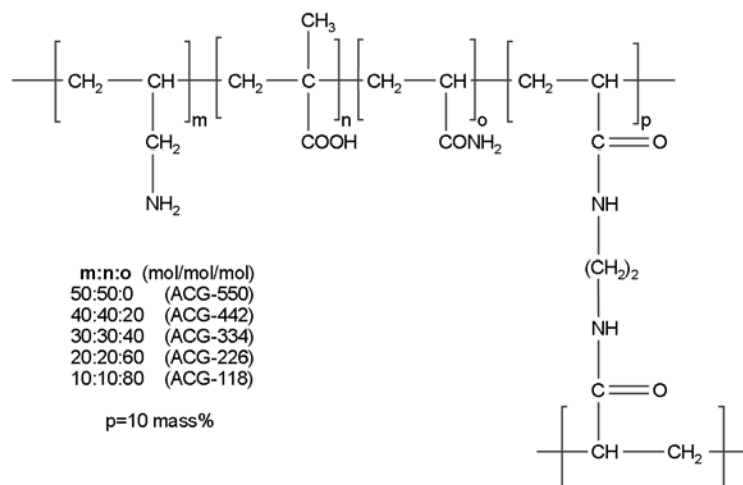


Figure 1. Structural units of amphoteric cryogels derived from AA, MAA and AAm crosslinked by MBAA

20:20:60, 30:30:40, 40:40:20 and 50:50:0 mol%/mol%/mol% were synthesized and abbreviated as ACG-118, ACG-226, ACG-334, ACG-442 and ACG-550 (Figure 1).

2.3. Potentiometric and conductimetric titrations

The fine powdered cryogel samples (10 mg) were put to 10 mL of distilled water, stirred 1 h and titrated by 0.1M HCl or KOH. Potentiometric and conductimetric titrations were carried out on the pH/conductivity meter 'Mettler Toledo MFC 227' (Switzerland) at room temperature. For calculation of pK_b of allylamine groups the Henderson-Hasselbalch equation $pOH = pK_b + n \cdot \log(\beta/(1 - \beta))$ (where β is the degree of ionization of primary amine groups of cryogels, n is the specific parameter for polyelectrolytes) was used.

2.4. Swelling experiments

The swelling capacity of cryogel samples as a function of pH was evaluated from the height measurements. For this dry gel sample with diameter 5 mm and height 10 mm was placed into a glass tube with diameter 10 mm the bottom of which was closed by Shott filter ended by valve. After passing of 100 mL of aqueous solutions through a gel sample with desired pH, that was adjusted by addition of 0.1 N HCl or KOH to distilled water to avoid the influence of buffer on swelling behavior, its height was accurately measured [16, 17]. Swelling experiments were repeated three times with experimental error not exceeding $\pm 5\%$. The ratio of L_s/L_0 (where L_s is the height of swollen gel, L_0 is the height of dry gel) on pH was plotted. The flow-rate of water passing through the cryogel samples was measured at a constant hydrostatic pressure equal to 100 cm of water column corresponding to a pressure of ca. 0.01 MPa as described in [21]. Measurements were repeated three times and the values averaged.

2.5. Sorption of metal ions

Sorption of Cu^{2+} , Ni^{2+} , and Co^{2+} ions by ACG-334 was performed as follows: a piece of dry sample with diameter 5 mm and height 10 mm was placed inside of the glass tube with diameter 5 mm and height 50 mm the bottom of which was closed by Shott filter ended by valve. Then 1000 mL of aqueous solution of metal salts or their mixture with

concentrations 10^{-3} or 10^{-5} mol/L was passed through the sample during 1 day. Desorption of metal ions was carried out by passing through gel sample 25 mL of 0.1 N HCl several times.

2.6. Methods

For SEM measurements cryogel samples were preliminary dehydrated by ethanol and dried at room temperature then in vacuum oven. The cylindrical sample with diameter 5 mm and height 10 mm was carefully cut by knife blade in parallel or perpendicular to the long axes and the longitudinal and cross sectional parts coated and uncoated with aluminum were examined on scanning electron microscope JSM5800 (Jeol, Japan). Probably due to the presence of electrically conducting amine and carboxylic groups we were able to observe the fine structure and longitudinal and cross sectional morphology of uncoated with aluminum cryogels samples. The concentration of adsorbed and desorbed metal ions was determined with the help of ion-plasma coupled emission spectrometer Optima 5100 DV (Perkin Elmer, USA). FTIR spectra were recorded on an Alpha-P (Bruker, Germany) in KBr pellets.

3. Results and discussion

Figure 2 shows the potentiometric and conductimetric titration curves of amphoteric cryogels. Gradual shifting of the inflection points to left side confirms overall decreasing of the content of carboxylic and amine groups in cryogels in the following order: ACG-550 > ACG-442 > ACG-334 > ACG-226 > ACG-118 and it is in good agreement with the variation of acid and base monomers in the feed. Compositions of amphoteric cryogels found from potentiometric and conductimetric titration curves together with ionization constant of allylamine groups (pK_b) and isoelectric pH (pH_{IEP}) are shown in Table 2.

For different samples the average molar composition of amphoteric cryogels found from the potentiometric titration curves is equal to 55.5 ± 2.0 mol% of COOH group and to 44.5 ± 2.0 mol% of NH_2 group while acid-base content found from conductimetric titration curves corresponds to 63 ± 4 mol% of COOH group and 37 ± 4 mol% NH_2 group. In spite of inconsistency of potentiometric and conductimetric titration data, they indicate that the composition of amphoteric cryogels is lightly enriched by

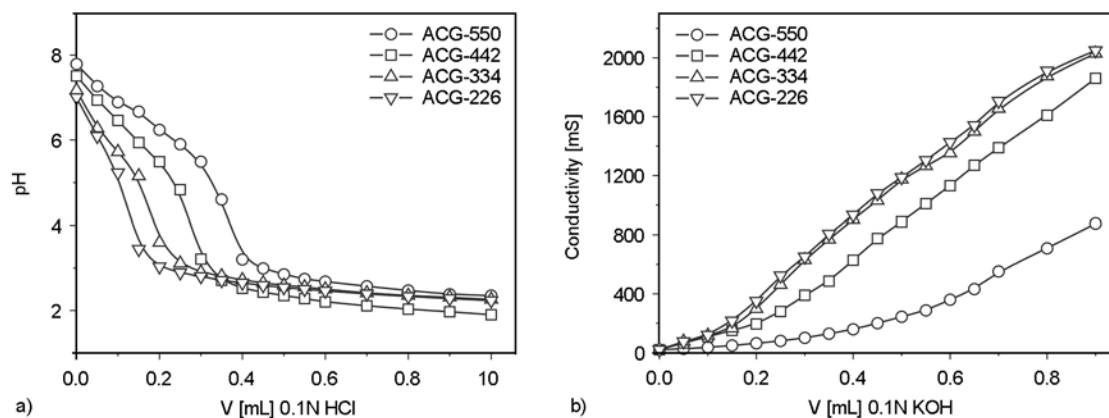


Figure 2. Potentiometric (a) and conductimetric (b) titration curves of amphoteric cryogels by 0.1M HCl (a) and KOH (b)

Table 2. Composition, ionization constant of allylamine groups (pK_b) and the isoelectric pH (pH_{IEP}) of cryogels

Cryogels	-NH ₂ groups [mol%]		-COOH groups [mol%]		pK_b	pH_{IEP}
	Potentiometric titration	Conductimetric titration	Potentiometric titration	Conductimetric titration		
ACG-550	46.7	41.0	53.3	59.0	5.44	4.0
ACG-442	42.4	37.0	57.6	63.0	5.25	4.1
ACG-334	43.3	33.3	56.7	66.6	5.78	4.2
ACG-226	–	41.4	–	58.6	5.62	4.3
ACG-118	–	38.5	–	61.5	–	3.5

acidic monomer probably due to relatively low activity of AA monomer in the copolymerization reaction [22].

The values of pK_b for ACG-550, ACG-442 ACG-334 and ACG-226 determined from Henderson-

Hasselbalch equation are equal to 5.44; 5.25; 5.78 and 5.62 respectively. Such values of pK_b suggest effective complexation of allylamine groups with transition metal ions and formation of coordination bonds.

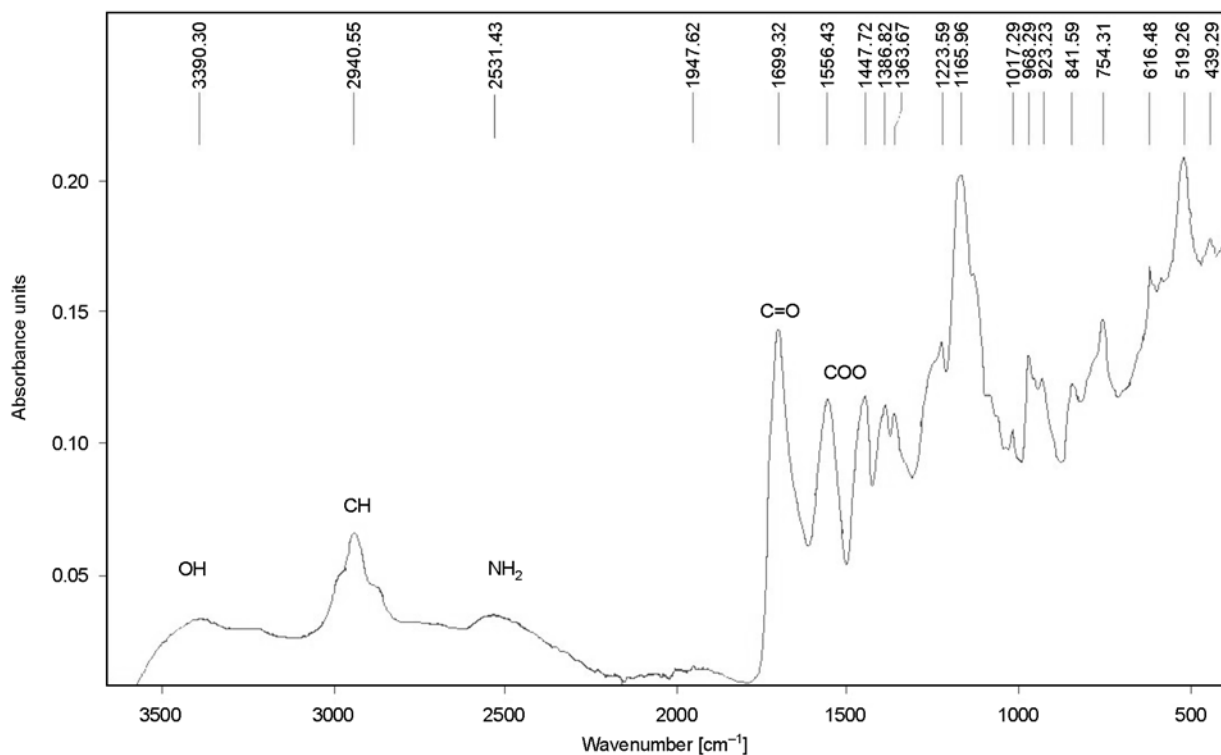


Figure 3. FTIR spectra of dry ACG-334

FTIR spectra of amphoteric cryogels show the characteristic bands of COO^- (1556 cm^{-1}), C=O (1699 cm^{-1}), NH_3^+ (2532 cm^{-1}), CH (2940 cm^{-1}), and OH (3390 cm^{-1}) groups (Figure 3). The appearance of the band at 3390 cm^{-1} can be attributed to OH groups of hydrated water tightly bonded to functional groups of cryogels. Coexistence of COO^- and NH_3^+ reveals the zwitterionic structure of cryogels due to the fact that partly transition of protons from carboxylic groups to amine one may take place.

According to a commonly adopted concept [4, 5] cryogels can contain closed-, open-, or through pores that permit liquid to fill them and ensure unhindered convectional flow of solutes within interconnected pores. Cross- and longitudinal sections of dry ACG-118 and ACG-442 show sponge-like porous structure with pore size ranging from 50 to $200\text{ }\mu\text{m}$ (Figure 4a–4d) and the interconnected channels (Figure 4b).

Dynamics of water flux through the cryogel samples with a diameter 5 mm and height 10 mm were evaluated (Table 2). Increasing of the content of

acidic and basic monomers in a series of ACGs leads to progressive decreasing of water flux. This phenomenon can probably be explained by different hydration degrees of ionic groups leading to ‘apparent’ decreasing of pore size of cryogels (Table 3).

One of the specific features of linear and crosslinked polyampholytes is the existence of so-called isoelectric points (IEPs) where intra- and intermolecular attractions of opposite fixed charges lead to pseudoneutral behavior and compact structure of amphoteric macromolecules [6, 7]. Figure 5 shows the swelling and deswelling of amphoteric cryogels as a function of pH. It is seen that the deswelling of amphoteric cryogels is minimal at the IEPs. The iso-

Table 3. Dynamics of water flow-rate through amphoteric cryogels

Amphoteric cryogels	Water flux [mL/min]
ACG-118	1.20 ± 0.10
ACG-226	0.35 ± 0.05
ACG-334	0.18 ± 0.05
ACG-442	0.05 ± 0.01
ACG-550	0.02 ± 0.01

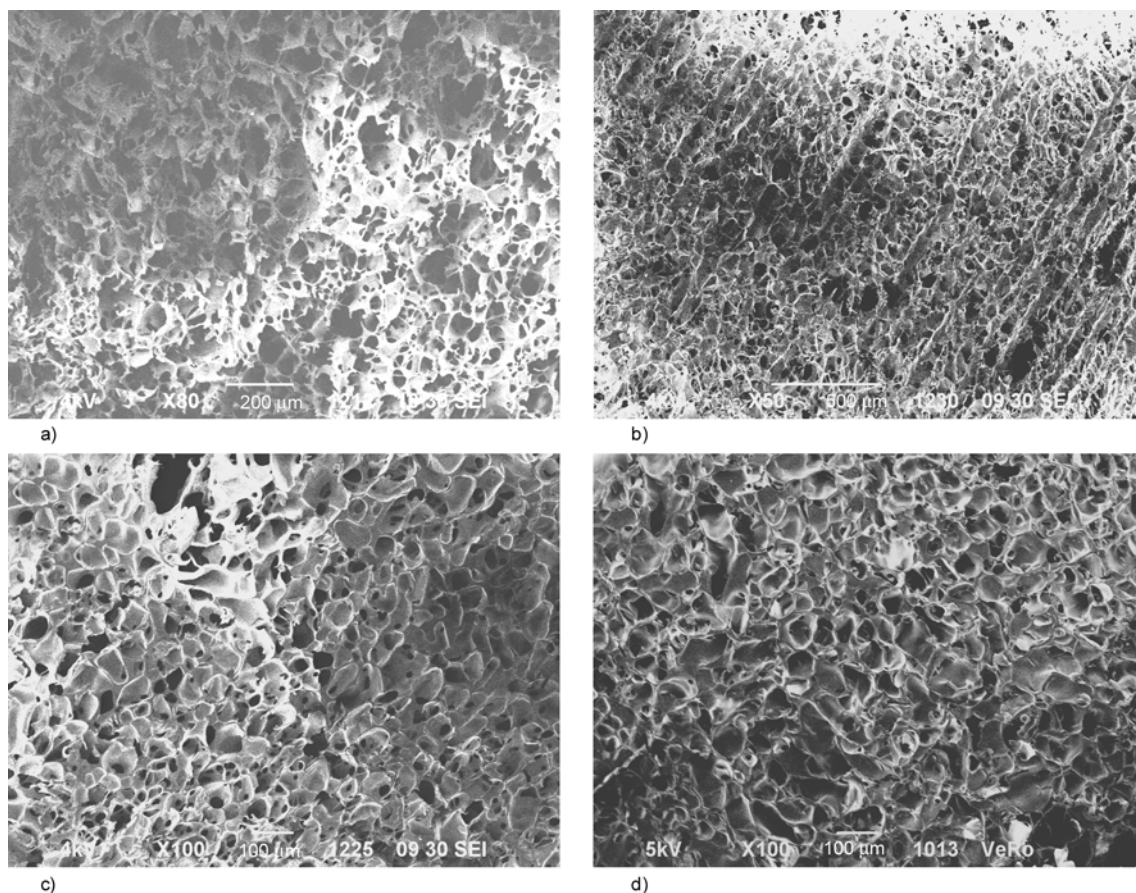


Figure 4. SEM images of cross (a, c, d) and longitudinal (b) sections of ACG-118 (a, b) and ACG-442 (c, d) uncoated (a, b, c) and coated (d) with aluminum

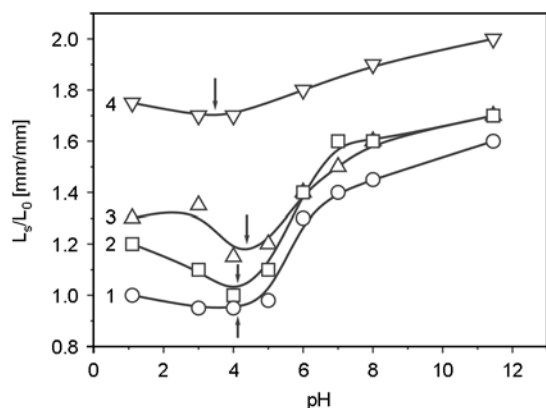


Figure 5. Swelling-deswelling curves of cryogels ACG-550 (curve 1), ACG-334 (curve 2), ACG-226 (curve 3), and ACG-118 (curve 4) on pH. Arrows show the IEPs

electric pH (pH_{IEP}) of amphoteric cryogels found from the swelling-deswelling measurements arranges between 3.5 and 4.3 (see Table 2).

The ability of cryogels to bind metal ions was also studied. Sorption of metal ions is accompanied by colorization of samples. This may be due both existing of free (uncomplexed) metal ions and metal ions coordinated with amine and/or carboxylic groups within cryogels (Figure 6). Involvement of allylamine groups into complexation reaction with transition metals ions and formation of chelate structure was studied earlier [23].

As seen from Table 4 the ACG-334 adsorbs up to 99.9% of metal ions from aqueous solution containing 10^{-3} mol/L of copper, nickel, and cobalt ions. In the course of passing of 1000 mL of metal ions with concentration of 10^{-5} and 10^{-3} mol/L through amphoteric cryogel ACG-334 gradually colorization of cryogel samples (especially for copper ions) was observed that is in favour of complexation reaction. The sorption capacity of ACG-334 with respect to

Table 4. Adsorbed and desorbed amounts of metal ions by ACG-334

Type of metal ions	Concentration of metal ions passed through ACG-334 [mol/L]	Adsorbed [%]	Desorbed [%]
Cu^{2+}	10^{-3}	99.9	51.4
Ni^{2+}		99.9	67.2
Co^{2+}		99.9	62.0
Cu^{2+}	10^{-5}	65.0	98.8
Ni^{2+}		73.0	95.2
Co^{2+}		72.3	91.1

10^{-3} mol/L of copper, nickel, and cobalt ions is equal to 634.9; 586.4; 588.7 mg respectively per 1 g of dry cryogel while the same parameter for 10^{-5} mol/L of copper, nickel, and cobalt ions is correspondingly equal to 41.3; 42.8 and 42.7 mg per 1 g of dry sample.

Desorption of metal ions by 0.1 N HCl is in the range from 51 to 67%. In spite of the fact that the adsorbed amount of metal ions from aqueous solution containing 10^{-5} mol/L is low, the desorbed amount of copper, nickel, and cobalt ions is high and equal to 98.8; 95.2 and 91.1% respectively. Preferentially adsorption of Cu^{2+} ions (79%) in comparison with Ni^{2+} (38%) and Co^{2+} ions (32%) from their mixture was also observed from aqueous solution containing 10^{-5} mol/L of metal ions indicating on the specific binding of copper ions. High adsorption capacity of amphoteric macroporous gels with respect to mM and trace metal ions may be perspective for purification of the wastewaters and analytical purposes. The reduction of cryogel-metal complexes by NaBH_4 leads to formation of nano- and micronsized particles of metals in reduced and oxidized forms [24, 25] immobilized on the inner and surface parts of amphoteric cryogels. The chemical composition of the Ni containing sample by energy dispersive X-ray

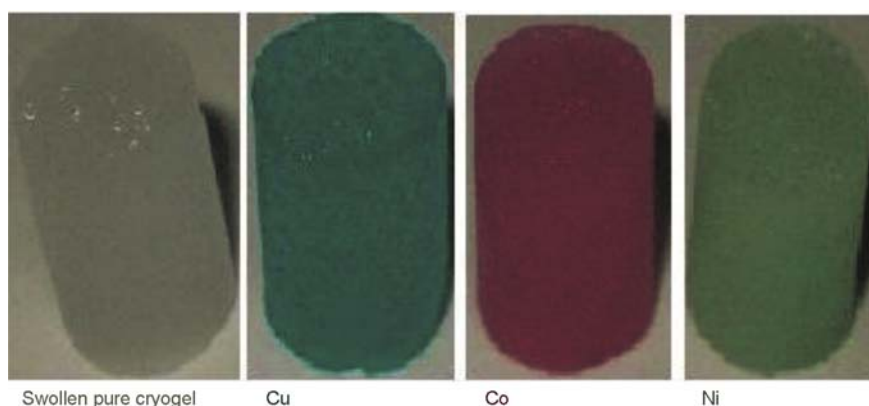


Figure 6. Adsorption of metal ions by macroporous amphoteric cryogel ACG-334

attached to SEM revealed that up to 34% mass % of Ni particles are formed. Thus amphoteric cryogels can serve as efficient heterogeneous supports for metal nanoparticles and as flow microreactors in catalysis.

4. Conclusions

SEM images of cross- and longitudinal sections of amphoteric cryogels show sponge-like porous structure and the interconnected channels. The content of acid-base groups determined by combination of potentiometric and conductimetric titrations is in favour of acidic groups. The isoelectric points of amphoteric cryogels found from the swelling measurements are arranged between 3.5 and 4.3. It has been shown that macroporous amphoteric cryogels are able to adsorb up to 99.9% of copper, nickel, and cobalt ions from 10^{-3} mol/L aqueous solution while to desorb from 91 to 98% metal ions from 10^{-5} mol/L aqueous solution. Desorption of metal ions by 0.1 N HCl ranges from 51 to 69%. Specific sorption of copper ions by amphoteric cryogel from the mixture of copper, nickel, and cobalt ions with concentration of 10^{-5} mol/L is also observed.

Acknowledgements

Financial support from the Ministry of Education and Science of the Republic of Kazakhstan is greatly acknowledged

References

- [1] Oh J. K., Drumright R., Siegwart D. J., Matyjaszewski K.: The development of microgels/nanogels for drug delivery applications. *Progress in Polymer Science*, **33**, 448–477 (2008).
DOI: [10.1016/j.progpolymsci.2008.01.002](https://doi.org/10.1016/j.progpolymsci.2008.01.002)
- [2] Graham N. B., Cameron A.: Nanogels and microgels: The new polymeric materials playground. *Pure and Applied Chemistry*, **70**, 1271–1275 (1998).
DOI: [10.1351/pac199870061271](https://doi.org/10.1351/pac199870061271)
- [3] Sing K. S. W., Everett D. H., Haul R. A. W., Moscou L., Pierotti R. A., Rouquérol J., Siemieniewska T.: Reporting physisorption data for gas/solid systems with special reference to the determination of surface area and porosity. *Pure and Applied Chemistry*, **57**, 603–619 (1985).
DOI: [10.1351/pac198557040603](https://doi.org/10.1351/pac198557040603)
- [4] Lozinskiy V. I.: Cryogels on the basis of natural and synthetic polymers: Preparation, properties and application. *Russian Chemical Reviews*, **71**, 489–511 (2002).
DOI: [10.1070/RC2002v071n06ABEH000720](https://doi.org/10.1070/RC2002v071n06ABEH000720)
- [5] Mattiasson B., Kumar A., Galaev I.: *Macroporous polymers: Production, properties and biotechnological/biomedical applications*. CRC Press, Boca Raton (2010).
- [6] Kudaibergenov S. E.: *Polyampholytes. Synthesis, characterization and application*. Kluwer Academic/Plenum Publishers, New York (2002).
- [7] Kudaibergenov S. E.: *Polyampholytes. Encyclopedia of polymer science and technology*. Wiley, New York (2008).
DOI: [10.1002/0471440264.pst562](https://doi.org/10.1002/0471440264.pst562)
- [8] Ogawa K., Nakayama A., Kokufuta E.: Preparation and characterization of thermosensitive polyampholyte nanogels. *Langmuir*, **19**, 3178–3184 (2003).
DOI: [10.1021/la0267185](https://doi.org/10.1021/la0267185)
- [9] Ogawa K., Nakayama A., Kokufuta E.: Electro-phoretic behavior of ampholytic polymers and nanogels. *The Journal of Physical Chemistry B*, **107**, 8223–8227 (2003).
DOI: [10.1021/jp022366z](https://doi.org/10.1021/jp022366z)
- [10] Deng L., Zhai Y., Guo S., Jin F., Xie Z., He X., Dong A.: Investigation on properties of P(MAA-co-DMAEMA)-g-EG polyampholyte nanogels. *Journal of Nanoparticle Research*, **11**, 365–374 (2009).
DOI: [10.1007/s11051-008-9391-2](https://doi.org/10.1007/s11051-008-9391-2)
- [11] Hu J., Yu S., Yao P.: Stable amphoteric nanogels made of ovalbumin and ovotransferrin via self-assembly. *Langmuir*, **23**, 6358–6364 (2007).
DOI: [10.1021/la063419x](https://doi.org/10.1021/la063419x)
- [12] Yu S., Hu J., Pan P., Yao P., Jiang M.: Stable and pH-sensitive nanogels prepared by self-assembly of chitosan and ovalbumin. *Langmuir*, **22**, 2754–2759 (2006).
DOI: [10.1021/la053158b](https://doi.org/10.1021/la053158b)
- [13] Miyake M., Ogawa K., Kokufuta E.: Light-scattering study of polyelectrolyte complex formation between anionic and cationic nanogels in an aqueous salt-free system. *Langmuir*, **22**, 7335–7341 (2006).
DOI: [10.1021/la060701v](https://doi.org/10.1021/la060701v)
- [14] Doi R., Kokufuta E.: On the water dispersibility of a 1:1 stoichiometric complex between a cationic nanogel and linear polyanion. *Langmuir*, **26**, 13579–13589 (2010).
DOI: [10.1021/la101852b](https://doi.org/10.1021/la101852b)
- [15] Wu W., Mitra N., Yan E. C. Y., Zhou S.: Multifunctional hybrid nanogel for integration of optical glucose sensing and self-regulated insulin release at physiological pH. *ACS Nano*, **4**, 4831–4839 (2010).
DOI: [10.1021/nn1008319](https://doi.org/10.1021/nn1008319)
- [16] Tan B. H., Ravi P., Tam K. C.: Synthesis and characterization of novel pH-responsive polyampholyte microgels. *Macromolecular Rapid Communications*, **27**, 522–528 (2006).
DOI: [10.1002/marc.200500830](https://doi.org/10.1002/marc.200500830)
- [17] Christodoulakis K. E., Vamvakaki M.: Amphoteric core-shell microgels: Contraphilic two-compartment colloidal particles. *Langmuir*, **26**, 639–647 (2010).
DOI: [10.1021/la902231b](https://doi.org/10.1021/la902231b)

- [18] Schachschal S., Balaceanu A., Melian C., Demco D. E., Eckert T., Richtering W., Pich A.: Polyampholyte microgels with anionic core and cationic shell. *Macromolecules*, **43**, 4331–4339 (2010).
DOI: [10.1021/ma100184h](https://doi.org/10.1021/ma100184h)
- [19] Ni H., Kawaguchi H., Endo T.: Preparation of amphoteric microgels of poly(acrylamide/methacrylic acid/dimethylamino ethylene methacrylate) with a novel pH–volume transition. *Macromolecules*, **40**, 6370–6376 (2007).
DOI: [10.1021/ma070358g](https://doi.org/10.1021/ma070358g)
- [20] Hoare T., Pelton R.: Charge-switching, amphoteric glucose-responsive microgels with physiological swelling activity. *Biomacromolecules*, **9**, 733–740 (2008).
DOI: [10.1021/bm701203r](https://doi.org/10.1021/bm701203r)
- [21] Arvidsson P., Plieva F. M., Savina I. N., Fexby S., Bülow L., Galaev I. Y., Mattiasson B.: Chromatography of microbial cells using continuous supermacroporous affinity and ion-exchange columns. *Journal of Chromatography A*, **977**, 27–38 (2002).
DOI: [10.1016/S0021-9673\(02\)01114-7](https://doi.org/10.1016/S0021-9673(02)01114-7)
- [22] Kabanov V. A., Topchiev D. A.: Polymerization of ionizing monomers. Nauka, Moscow (1975).
- [23] Bekturov E. A., Kudaibergenov S. E., Zhaimina G. M., Saltykov Y. P., Pel'menstein B. Y.: Complexation of polyallylamine with transition metal ions in aqueous solution. *Die Makromolekulare Chemie, Rapid Communications*, **7**, 339–343 (1986).
DOI: [10.1002/marc.1986.030070603](https://doi.org/10.1002/marc.1986.030070603)
- [24] Park B. K., Jeong S., Kim D., Moon J., Lim S., Kim J. S.: Synthesis and size control of monodisperse copper nanoparticles by polyol method. *Journal of Colloid and Interface Science*, **311**, 417–424 (2007).
DOI: [10.1016/j.jcis.2007.03.039](https://doi.org/10.1016/j.jcis.2007.03.039)
- [25] Liu X., Guo M., Zhang M., Wang X., Guo X., Chou K.: Effects of PVP on the preparation and growth mechanism of monodispersed Ni nanoparticles. *Rare Metals*, **27**, 642–647 (2008).
DOI: [10.1016/S1001-0521\(08\)60198-9](https://doi.org/10.1016/S1001-0521(08)60198-9)

Novel elastomer dye-functionalised POSS nanocomposites: Enhanced colourimetric, thermomechanical and thermal properties

S. Spoljaric*, R. A. Shanks

CRC for Polymers, RMIT University, GPO Box 2476V Melbourne, Victoria 3001, Australia

Received 29 September 2011; accepted in revised form 26 November 2011

Abstract. Nanocomposites consisting of poly(styrene-*b*-butadiene-*b*-styrene) (SBS) and polyhedral oligomeric silsesquioxanes (POSS) were prepared using a solvent dispersion method. POSS molecules were functionalised with two dichlorotriazine reactive dyes (CI Reactive Blue 4, CI Reactive Red 2) prior to compounding. Infrared spectroscopy confirmed functionalisation. Scanning electron microscopy revealed an increase in filler aggregation with concentration, with preferential phase selectivity. Ultraviolet spectroscopy and colourimetry confirmed colour uniformity and suggested that colour intensity could be controlled. Functionalised POSS improved thermal stability by imparting restrictions on SBS chain motions. Tensile stress-strain analysis revealed an increase in modulus with filler concentration, while creep deformation decreased and permanent strain increased with POSS content. Storage modulus, loss modulus and glass transition temperature increased with filler content due to effective SBS-POSS interaction. Nanocomposite properties were influenced by the phase the filler was dispersed throughout and the structure of the dye chromophore.

Keywords: polymer composites, polyhedral oligomeric silsesquioxanes, reactive dye, functionalisation, phase selectivity

1. Introduction

Coloured polymers are utilised in a variety of applications, particularly consumer products, packaging and building materials, due to improved appearance and aesthetic value. The traditional method of producing coloured polymer materials involves directly adding the dye or pigment into the polymer; however this process has several drawbacks. Conventionally coloured polymers can fade, lose colour or experience unexpected colour changes. Dyes may leach from the polymer matrix, lose intensity or bleach due to external factors, such as ultraviolet light, radiation and thermal degradation [1]. To further complicate matters, dispersion of dyes throughout a polymer is difficult, leading to swirling and variation in colour. Poor dispersion can lead to poor mechanical properties. Although compatibilisers

have been used to aid with dispersion, they are expensive and can also be detrimental to mechanical and thermal properties.

One solution is to covalently bond the dye to a stable media and disperse the dye-functionalised particles throughout the polymer. Functionalised-nanoparticles have been prepared by bonding reactive dyes with alumina [1] and silica [2, 3]. Another option is to use polyhedral oligomeric silsesquioxanes (POSS, empirical formula $\text{RSiO}_{1.5}$). These hybrid molecules consist of a rigid inorganic core made up of 8, 10 or 12 silicon atoms linked by oxygen atoms, with organic 'R' substituents attached at the corners of the silica cage. The central core is ceramic in nature, providing thermal stability and rigidity, while the organic groups compatibilise the molecule [4]. First synthesised in 1946 by Scott [5], POSS have begun

*Corresponding author, e-mail: s.spoljaric@student.rmit.edu.au

© BME-PT

to attract serious attention as a filler material within the last 10 to 15 years, encouraged by the significant improvement in composite properties the fillers provide. Furthermore, a variety of functional groups have been bonded directly onto POSS molecules [6–9]. By preparing dye-functionalised POSS nanoparticles and dispersing them throughout a polymer, the POSS can provide enhanced mechanical and thermal properties and overcome compatibility issues while the dye maintains its functionality, colouring the polymer matrix in the process. The hybrid-pigment will also encouraged dispersion, allowing a degree of control over the functionality and producing a more uniform, stable and visually pleasing material.

Block copolymers have received much academic and industrial attention since the early 1960's, due to low production costs and unique intrinsic properties. In recent times, focus has shifted towards nanotechnology applications, mainly due to the ability of these polymers to form self-assembled domains on the nanometre scale and the ease of which domain size/shape can be manipulated by altering the molecular weight or block concentration [10, 11]. This allows for potential in a number of applications, including biomedical, membrane formation, electronics and information technology [12]. A popular choice of block copolymer is poly(styrene-*b*-butadiene-*b*-styrene) (SBS), a linear triblock-elastomer consisting of hard, glassy polystyrene and soft, rubbery polybutadiene segments. SBS nanocomposites have received much attention in recent years, with fillers including silica, carbon black and montmorillonite clays being incorporated into the

SBS matrix [13–15]. While enhancements in composite properties have been achieved, molecular-level dispersion has been difficult, due to poor matrix-filler compatibility. This can lead to further complications when the objective is to disperse fillers within a particular phase. The incorporation of POSS into SBS has been limited [16–18]. Furthermore, SBS-POSS nanocomposites are usually prepared with grafting reactions. This leaves the opportunity of preparing these nanocomposites using physical blending and to determine whether adequate filler dispersion can be achieved. In addition, the benefit of dispersing the POSS throughout a copolymer, such as SBS, will allow the phase preference of the filler to be observed, due to the compatibilising organic 'R' groups on the POSS molecule.

The aim was to synthesis SBS-POSS nanocomposites via a physical blending process, where the POSS will favour a specific phase of the polymer matrix and enhance composite properties, while the functionality of the dye remains intact. Objectives included functionalising the POSS molecules with dichlorotriazine reactive dyes, preparing SBS-POSS nanocomposites using a solvent dispersion technique and characterising the thermal and mechanical properties of the nanocomposites.

2. Experimental

2.1. Materials

The poly(styrene-*b*-butadiene-*b*-styrene) used as matrix material was Kraton D-1102 (Kraton Polymers LLC). It is a pure, linear triblock copolymer with 29.5 wt% bound styrene and a density of

Table 1. POSS molecule characteristics

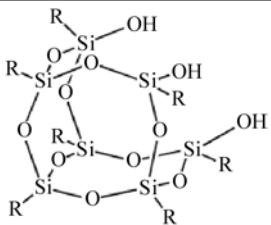
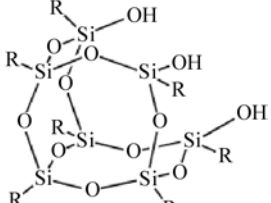
POSS	Structure	R group
TrisilanolisobutylPOSS		Isobutyl
TrisilanolphenylPOSS		Phenyl

Table 2. Dye characteristics

Colour index name	Trade name	Structure
CI Reactive Blue 4	Procion Blue MX-R	
CI Reactive Red 2	Procion Red MX-5B	

0.938 g·cm³. Two types of POSS were used as fillers; Trisilanophenyl POSS and Trisilanolisobutyl POSS. Both were supplied by Hybrid Plastics Inc. and their specifications are listed in Table 1. Two varieties of dichlorotriazine dye were reacted with the POSS molecules, CI Reactive Blue 4 (Procion Blue MX-R) and CI Reactive Red 2 (Procion Red MX-B5), obtained from Kraft Colour Pty Ltd., Whittlesea, Australia. The structures and details of the dyes are shown in Table 2. 3-aminopropyltriethoxysilane and diisopropylethylamine were obtained from

Aldrich Chemical Co., Milwaukee, USA. All chemicals were used as received.

2.2. Preparation of dye-functionalised POSS

2.2.1. Preparation of 3-amino treated POSS

Figure 1 shows the preparation of dye-functionalised POSS. 3-Aminopropyltriethoxysilane (10 mL) was dissolved in 100 mL of toluene. Trisilanol POSS was added while the solution was vigorously stirred. The reaction suspension was subjected to ultrasonic disruption (20 kHz, 10 min, 25°C) then refluxed for

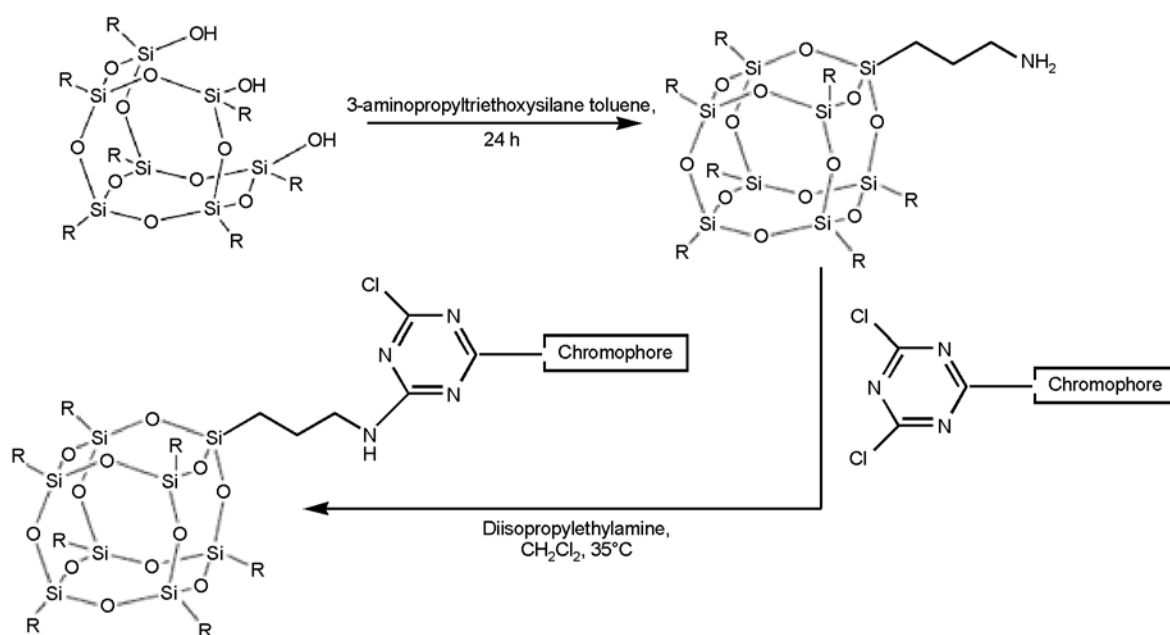


Figure 1. Preparation of dye-functionalised POSS

3 h. After being left at ambient overnight to allow the toluene to evaporate, the recovered POSS was washed with toluene, followed by methanol and acetone, respectively. The POSS was dried in a vacuum oven at 80°C for 12 h and kept in a desiccator over silica gel.

2.2.2. Reaction of dichlorotriazine dyes with treated POSS

To 50 mL of dichloromethane, the amino-functionalised POSS (5 g), dichlorotriazine dye (5 wt%) and diisopropylethylamine (5 mL) were added. The solution was stirred at 35°C for 1 h. The POSS-dye hybrid was filtered, washed with methanol and stored in a desiccator over silica gel.

2.3. Preparation of SBS-POSS nanocomposites

Nanocomposites with various functionalised-POSS concentrations (1, 5, 10, 20 wt%) were prepared using a solvent dispersion technique. SBS was dissolved in 150 mL of dichloromethane and vigorously stirred for 1 h at 25°C, until the polymer was completely dissolved. POSS was added to the solution and subjected to ultrasonic disruption (20 kHz, 10 min, 25°C) to ensure even distribution of the filler throughout the matrix. The solution was poured into an excess of cold methanol to precipitate the nanocomposite material and to restrict filler migration. The composite was isolated using suction filtration and dried in a desiccator overnight. Films for subsequent use were prepared using a heated press (IDM Instruments Inc., model number L0003-1). Films were heated to 150°C, 6 tonnes of pressure applied, held for 2 min and cooled to ambient.

The nomenclature for the nanocomposites is SBS-*x*POSS-*y z*, where *x* corresponds to the functional groups on the POSS (phenyl or isobutyl), *y* is the dye that POSS was reacted with (blue or red) and *z* equals the amount of POSS or functionalised POSS within the composite by wt%.

2.4. Characterisation of nanocomposites

2.4.1. Structural analysis

A Perkin-Elmer Spectrum 2000 FTIR spectrometer working in diffuse reflectance spectroscopy (DRIFTS) mode was used to characterise the molecular vibration of the functional groups in the POSS

and reactive dyes. Anhydrous potassium bromide (KBr) was used as dispersing material and all spectra were scanned within the range 400–4000 cm⁻¹, with a total of 20 scans and a resolution of 8 cm⁻¹.

2.4.2. Morphological analysis

Scanning electron microscopy (SEM) images of the nanocomposites were taken using a FEI Quanta 200 environmental scanning electron microscope (ESEM) operating at 20 kV. Composites with average dimensions ~4.00×4.00×0.70 mm³ were mounted to the specimen holder using carbon tape.

2.4.3. Thermal analysis

A Perkin-Elmer TGA-7 thermogravimetric analyser was used to analyse the thermal stability of the nanocomposites. Samples of ~10 mg were heated to 850°C at 20°C·min⁻¹ in an inert environment provided by a 20 mL·min⁻¹ nitrogen purge. The mass loss and its derivative were recorded as a function of temperature.

2.4.4. Visible spectroscopy

A Varian 50 Bio UV-visible spectrophotometer was used to analyse the absorbance properties of the nanocomposites. Composites were scanned over a wavelength range of 800 to 200 nm using a dual beam at a scan rate of 108 nm·min⁻¹. The composites had an average thickness of ~0.70 mm and the results presented are the average of five replicates.

2.4.5. Colourimetry

A Konica Minolta CR-400 Chroma Meter was used to analyse the colourimetric properties of the dye-functionalised nanocomposites. CIELAB (*L**, *a**, *b**) colour space coordinates were obtained, with results presented being the average of 10 measurements. A white ceramic tile (*Y* = 93.9, *x* = 0.3134, *y* = 0.3197) was used as a calibration reference.

2.4.6. Thermomechanical analysis

Thermomechanical analysis was performed using a TA Instruments Q800 Dynamic Mechanical Analyser in tensile mode to analyse the elastic properties of the composite films. Rectangular films of ~12.80 × 4.00 × 0.70 mm³ were subjected to stress-strain, creep-recovery and modulated force-thermomechanometry.

Stress-strain

Stress-strain (dynamic force-thermomechanometry, df-TM) analysis was performed using an initial force of 10 mN followed by an applied force increasing at a rate of $1 \text{ N} \cdot \text{min}^{-1}$, reaching a maximum of 18 N. Tests were conducted under ambient conditions (30°C) to determine the linear viscoelastic region and elastic modulus. Results presented are the average of triplicate measurements.

Creep-recovery

Creep-recovery (static force-thermomechanometry, sf-TM) analysis was performed by subjecting films to an applied stress of 0.5 MPa for 20 min, followed by a recovery period of 80 min with 0.01 MPa applied stress. The applied stress chosen was within the linear viscoelastic region of all the nanocomposites. Tests were conducted at ambient temperature (30°C) and all results presented are the average of triplicate measurements. The four-element model of Maxwell and Kelvin-Voigt (Figure 2) was used to interpret the creep component. The springs correspond to elastic sections with moduli E_1 and E_2 , while the dashpots represent the viscosity (η_1 , η_2). The overall deformation of the model is given in Equation (1):

$$\varepsilon(f) = \frac{\sigma_0}{E_1} + \frac{\sigma_0}{\eta_1} + \frac{\sigma_0}{E_2} (1 - e^{-t/(\eta_2/E_2)}) \quad (1)$$

The stretched exponential function of Kohlrausch, Williams and Watts [19] (KWW) was used to interpret the recovery behaviour and is given in Equation (2):

$$\phi = A \exp^{-(t/\tau)^\beta} \quad (2)$$

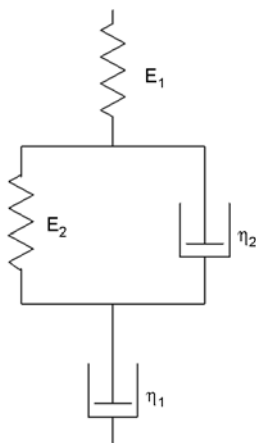


Figure 2. The four-element model

where A is the pre-exponential coefficient, t is time, τ is the retardation time and β is the non-linearity coefficient ($0 < \beta < 1$).

Elastic and viscoelastic properties

Modulated force-thermomechanometry (mf-TM) analysis was conducted using a static force of 500 mN, modulated force of 100 mN and frequency of 1 Hz. The storage modulus (E'), loss modulus (E''), loss tangent ($\tan \delta$) and associated glass transition (T_g) temperatures of the films were measured as a function of temperature from -100 to 110°C at a heating rate of $2^\circ\text{C} \cdot \text{min}^{-1}$.

3. Results and discussion

3.1. Chemical structure of dye-functionalised POSS

FTIR spectroscopy was used to confirm the chemical structure formed by the reaction of POSS and the reactive dyes, to determine whether bonding between the respective molecules was achieved. The infrared spectra of the untreated POSS and dyes are shown in Figure 3a. The pure POSS show several bands characteristic of their structure; 3154 cm^{-1} (hydroxyl (OH) stretching vibrations), 1100 and 890 cm^{-1} (Si–O–Si and SiOH stretching vibrations). TrisilanolphenylPOSS displays bands at 1594 , 1490 and 1430 cm^{-1} , corresponding to vibrational stretching of the C=C bonds within the phenyl 'R' groups. The three bands in this region confirm the presence of a conjugated phenyl system. Other bands corresponding to the trisilanolphenylPOSS structure include 3070 cm^{-1} (sp^2 CH stretching vibrations), 696 and 740 cm^{-1} (C–H bending vibrations). TrisilanolisobutylPOSS exhibits strong bands at 2950 , 2900 and 2868 cm^{-1} , corresponding to vibrational stretching of the CH_3 , CH_2 and CH groups of the isobutyl 'R' groups. Other peaks specific to isobutyl include those at 1462 , 1400 , 1366 and 1328 cm^{-1} , correlating to CH_2 and CH_3 bending vibrations and deformation.

The reactive dyes exhibited several bands indicative of the functionality/segments common in both structures; 3436 cm^{-1} (N–H stretching vibrations), 3064 cm^{-1} (C–N symmetric stretching), 2924 cm^{-1} (C–N asymmetric stretching), 1212 cm^{-1} (C–N stretching vibrations), 1042 cm^{-1} (S=O stretching vibrations) and 678 cm^{-1} (C–Cl stretching). CI Reactive Blue 4 displays additional bands specific

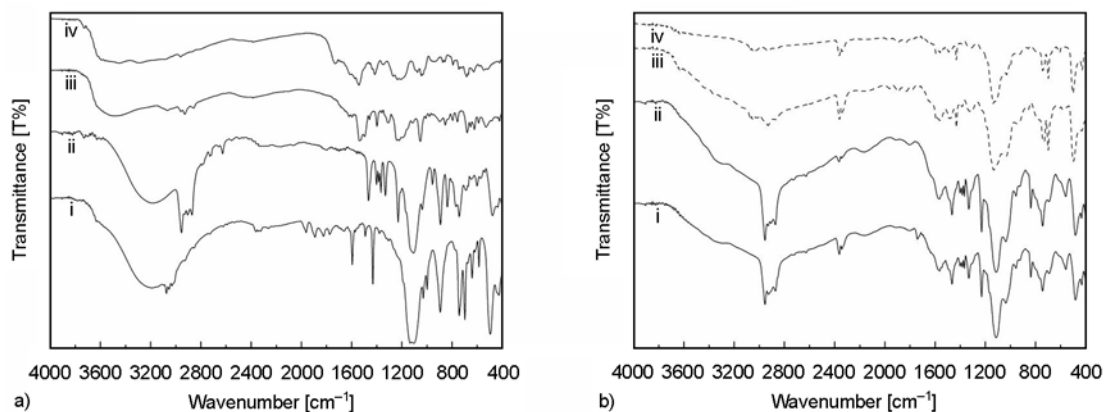


Figure 3. (a) Infrared spectrographs of raw materials; (i) TrisilanolphenylPOSS, (ii) TrisilanolisobutylPOSS, (iii) CI Reactive Red 2, (iv) CI Reactive Blue 4, (b) infrared spectrographs of functionalised POSS; (i) ibPOSS-blue, (ii) ibPOSS-red, (iii) phPOSS-blue, (iv) phPOSS-red

to its structure at 3258 cm^{-1} (N–H stretching vibrations for secondary amines), 1538 cm^{-1} (NH_2 scissoring), 1718 cm^{-1} (C=O stretching for saturated ketones) and 1404 cm^{-1} (SO_3H stretching vibrations). CI Reactive Red 2 displayed additional characteristic peaks at 1534 cm^{-1} (N=N stretching of the azo group), 862 and 964 cm^{-1} (NH_2 and NH wagging – shifts on H-bonding).

The infrared spectrographs of the dye-functionalised POSS nanoparticles are shown in Figure 3b. For all nanoparticles, a noticeable reduction in peak size is noticed at 3154 cm^{-1} . This indicates a reduction in the number of OH groups on the POSS molecules, suggesting that bonding has occurred with the reactive dyes. Strong peaks are observed at 1100 cm^{-1} , confirming the presence of Si–O bonds. Both isobutylPOSS pigments display bands at 2950 and 2868 cm^{-1} , confirming the presence of isobutyl groups. Similarly, phenylPOSS pigments displayed characteristic peaks at 3044 cm^{-1} (CH stretching vibrations) and 1580 , 1554 and 1542 cm^{-1} (C=C vibrational stretching of phenyl groups). The presence of the reacted dyes was confirmed by the occurrence of several characteristic peaks in all functionalised POSS; 3296 cm^{-1} (NH stretching vibrations), 1558 cm^{-1} (NH_2 scissoring), 1546 cm^{-1} (NH bending vibrations) and 700 cm^{-1} (C–Cl stretching). These observations confirm that covalent bonding has occurred between the amino-treated trisilanolPOSS and reactive dyes.

3.2. Morphology

Scanning electron microscopy (SEM) was employed to investigate the morphology of the nanocompos-

ites. The micrographs are presented in Figure 4. Incorporation of up to 5 wt% POSS into the SBS resulted in a relatively uniform distribution of filler throughout the matrix, with POSS clustering into small agglomerates with an average diameter of $\sim 0.08\text{--}0.1\text{ }\mu\text{m}$. As the concentration of POSS increased, so too did the occurrence of agglomeration, ranging from few small instances at 5 wt% (Figure 4a) to the formation of large agglomerates at 20 wt% with average diameters of $\sim 0.6\text{--}0.7\text{ }\mu\text{m}$ (Figure 4b). Despite utilising ultrasonic disruption to discourage filler clustering and polymer precipitation to ‘trap’ the filler in place, the micrographs indicate that at POSS concentrations greater than 5 wt%, interactions between the functionalised POSS nanoparticles are quite strong and can withstand physical methods used to encourage particle separation. These interactions are usually in the form of Coulomb and van der Waals forces.

Figure 4c and 4d display the micrographs of SBS-ibPOSS-red 5 and SBS-phPOSS-red 5, respectively. Incorporation of 5 wt% red-functionalised isobutylPOSS gives an even distribution of filler throughout the matrix, with small clusters of $\sim 0.1\text{--}0.2\text{ }\mu\text{m}$. Conversely, addition of phenylPOSS at the same concentration and functionalised with the same dye leads to an increase in the development of agglomeration, with larger clusters of $\sim 0.4\text{--}0.6\text{ }\mu\text{m}$ occurring. This behaviour is attributed to the corner ‘R’ groups on the silsesquioxane cages, which determine phase compatibility and, therefore, morphology. As noted previously, the bulk of the SBS matrix used consists of polybutadiene ($\sim 70.5\text{ wt}\%$), providing POSS cages with isobutyl ‘R’ groups a

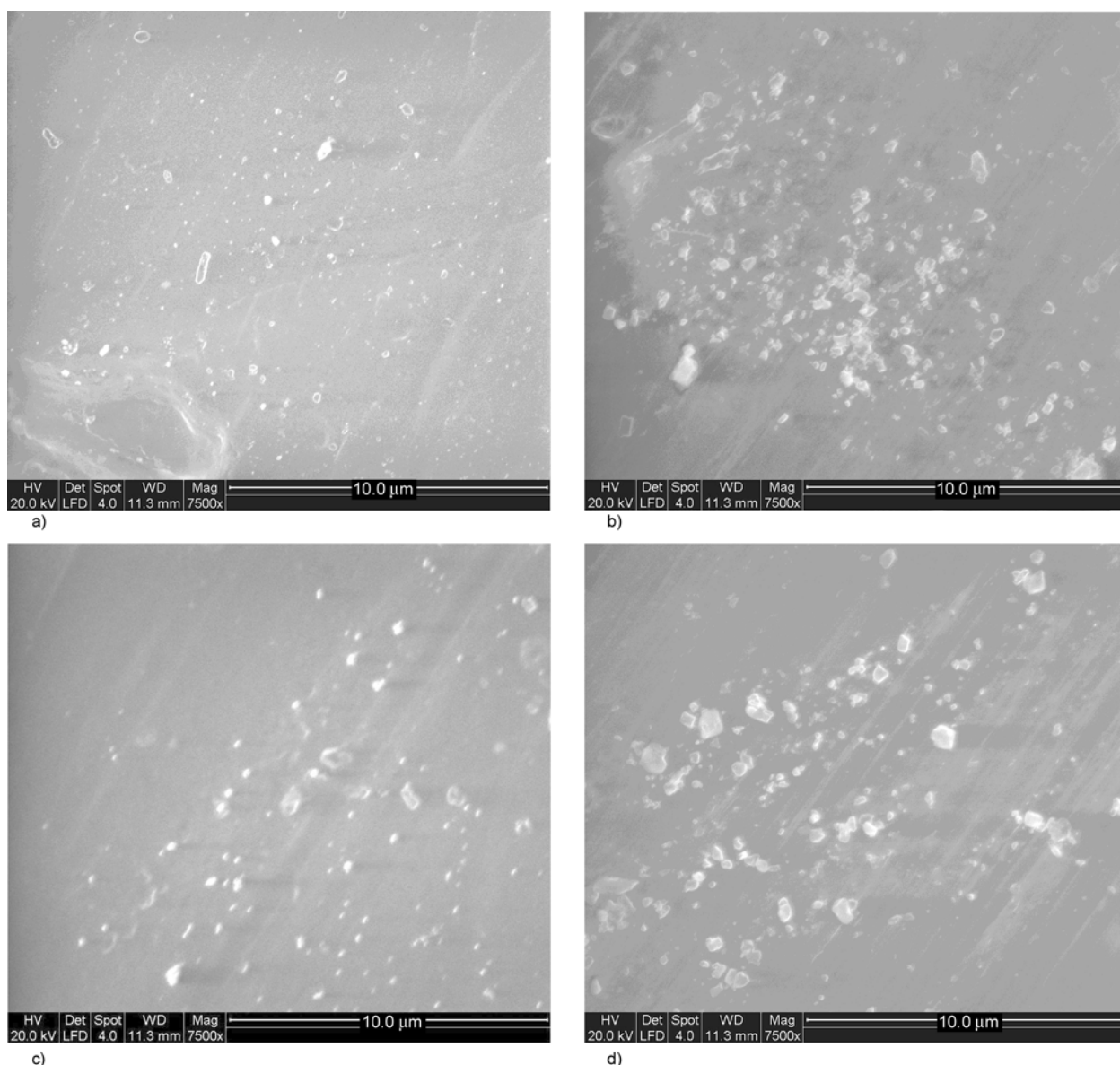


Figure 4. Scanning electron micrographs of SBS-POSS nanocomposites; (a) ibPOSS-blue 5, (b) ibPOSS-blue 20, (c) ibPOSS-red 5 (d) phPOSS-red 5

relatively large volume to disperse throughout and occupy. This was in contrast to phenylPOSS, which by comparison has a significantly smaller volume of polymer (styrene phase) to occupy, leading to increased interactions between the POSS molecules due to their proximity. This leads to the formation of larger agglomerates within the fewer styrene domains available and correlates to observations in SBS-dumbbell POSS composites. This provides complimentary details reinforcing the phase preference behaviour is still being maintained, even with the addition of dichlorotriazine reactive dyes.

3.3. Optical properties of SBS dye-functionalised POSS composites

3.3.1. Colourimetry

The CIELAB (L^* , a^* , b^*) colour space coordinates of SBS and the dye-functionalised nanocomposites are presented in Table 3. The L^* coordinate represents the whiteness of the material (0 = black, 100 = white). Pure SBS displayed an L^* value of 94.13, indicative of its transparency. The nanocomposites became more translucent and intense in colour with increasing functionalised-POSS content, which was characterised by a decrease in the value of L^* . This

Table 3. CIELAB colour space co-ordinates of SBS-POSS nanocomposites

Material	L^*	a^*	b^*
SBS	94.13	0.00	2.74
ibPOSS-blue 1	82.49	0.36	-10.78
ibPOSS-blue 5	44.43	6.49	-32.94
ibPOSS-blue 10	34.94	9.50	-36.42
ibPOSS-blue 20	23.87	14.23	-37.78
ibPOSS-red 1	80.38	25.21	-4.73
ibPOSS-red 5	53.09	59.17	1.70
ibPOSS-red 10	42.38	61.11	14.93
ibPOSS-red 20	30.22	62.80	16.37
phPOSS-blue 1	87.63	0.06	-4.02
phPOSS-blue 5	68.67	1.54	-24.56
phPOSS-blue 10	46.48	6.76	-31.22
phPOSS-blue 20	28.37	12.85	-35.87
phPOSS-red 1	88.67	9.14	-3.67
phPOSS-red 5	70.68	35.25	0.52
phPOSS-red 10	53.72	54.89	1.48
phPOSS-red 20	39.62	58.86	10.98

was expected since a higher filler concentration causes an increase in the number of bound-dye molecules dispersed throughout the polymer. Isobutyl-POSS nanocomposites yielded lower L^* than their phenylPOSS counterparts at the same concentration, attributed to the dispersion of POSS (and dye) throughout the continuous, polybutadiene phase. The a^* coordinate provides an indication of the colour's position between red and green (negative = green, positive = red) while the b^* coordinate gives the position between blue and yellow (negative = blue, positive = yellow). Nanocomposites containing POSS functionalised with CI Reactive Blue 4 displayed a^* values which gradually became more positive with filler content and b^* values which rapidly became negative. This correlated well with the increasing intensity of blue colour which developed throughout the polymer with the increase in functionalised-POSS concentration. Materials containing CI Reactive Red 2 functionalised-POSS yielded a^* and b^* values which both became positive. As with their blue dye counterparts, this behaviour was accompanied by an increase in colour intensity with filler content. In particular, b^* values leveled-off at higher filler loadings, due to limited dispersion throughout the SBS matrix.

Composites with filler loadings of 1 and 5 wt% visually displayed a uniform and even distribution of colour. As the concentration increased to 10 and 20 wt%, the quality of colourimetric properties began to decline, with pigment specks and minor

swirling being observed. This deterioration in visual appearance was more evident in phenylPOSS composites than those containing isobutylPOSS and can be attributed to the degree of filler dispersion. Furthermore, interactions between auxochromes (NH_2 , SO_3H and $\text{C}=\text{O}$ on CI Reactive Blue 4, SO_3Na and OH on CI Reactive Red 2) may result in filler agglomeration. Colour-producing ability is proportional to the amount of pigment surface that can interact with light. Thus, the ability of a pigment to selectively absorb specific wavelengths of light increases with decreasing particle size, reaching optimal values when the particle is completely penetrated by light [20]. Due to the structural composition of SBS, POSS containing isobutyl 'R' compatibilising groups have greater phase volume to disperse throughout compared with phenylPOSS. This greater degree of volume reduces the probability of agglomerate formation, particularly at higher filler loadings (10 and 20 wt%). The 'dye-functionalised POSS chromophores' are not transparent (the pure POSS particles are white) and lack optimal light-absorption properties, due to their tendency to cluster at higher filler loadings. The chromophores were not surface-treated for two reasons; (1) to leave the visual properties of the dye unchanged and (2) to not compromise the mechanical or thermal properties of the composite. The colourimetric results indicate that although the colour intensity can be increased, consistency and uniformity decrease at dye-functionalised POSS concentrations past 5 wt%.

3.3.2. UV-visible spectroscopy

The UV absorbance spectra of various SBS-POSS nanocomposites are shown in Figure 5. Nanocomposites containing CI Reactive Red 2-functionalised POSS (Figure 5a) displayed absorption spectra indicative of a red dye/pigment, with strong peaks at ~520 and 550 nm (green absorption) and a weaker band at ~370 nm (violet absorption). Little-to-no absorbance was observed across the red wavelength region (620–750 nm), indicative of the reflectance of red light by the chromophore. Absorbance intensity increased with filler concentration, due to the increased number of dye-functionalised POSS segments able to absorb and reflect light. The incorporation of CI Reactive Blue 4-functionalised POSS into SBS yielded strong peaks at

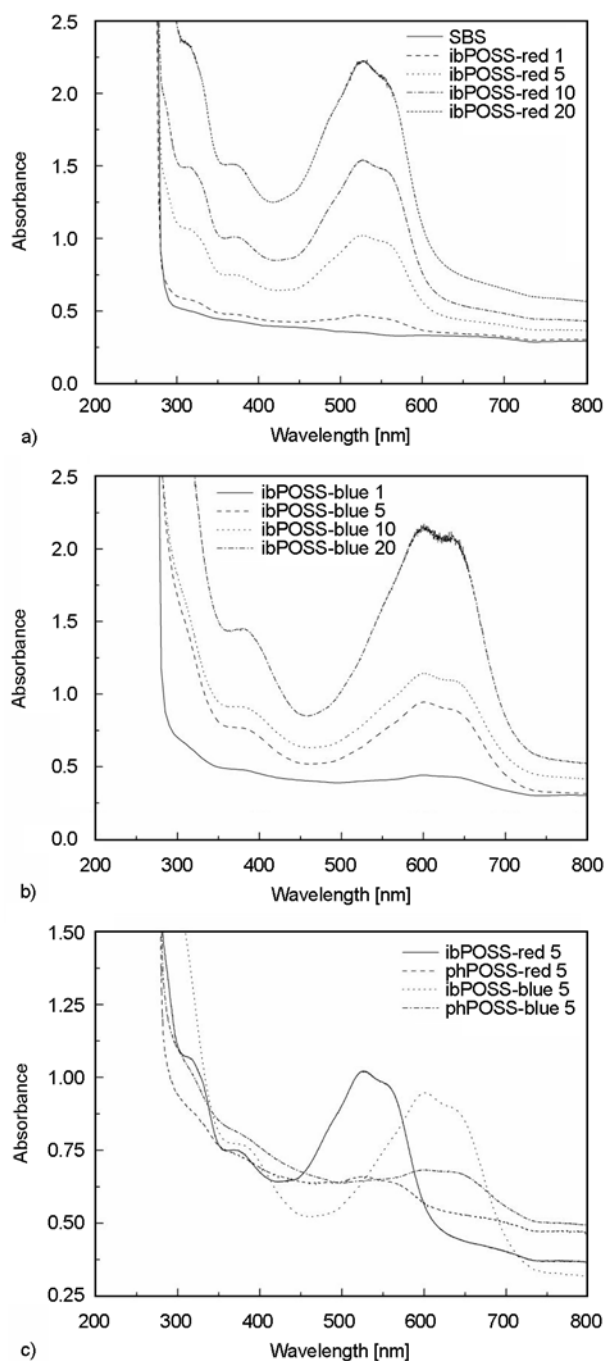


Figure 5. (a) Absorbance spectra of ibPOSS-red composites, (b) absorbance spectra of ibPOSS-blue composites, (c) absorbance spectra of 5 wt% filled composites

~600 and 630 nm (absorption of orange/red), with an additional weaker wavelength band at ~375 nm (violet absorption), as shown in Figure 5b. A large trough was observed at ~450 nm, indicating the reflectance of blue light. The intensity of the UV absorbance increased with filler concentration, which correlated with the increase in colour intensity observed at higher filler concentrations.

A significant difference in the absorbance properties of both blue- and red-dye functionalised materials was clearly observed in the nanocomposites derived from isobutylPOSS and phenylPOSS. Composites prepared with isobutylPOSS exhibited greater absorbance peaks compared with phenylPOSS, this behaviour attributed to the compatibility and dispersion of the respective functionalised fillers within SBS. Although ultrasonic disruption was used in an attempt to obtain a full dispersion of particles throughout the matrix, specific interactions between particles and phase preference limited the ability to obtain the optimal level of dispersion desired. Ideally, when adding dyes or pigments into a polymer, the goal is to achieve full dispersion of particles throughout the matrix, since this gives the highest possible colour strength [21].

IsobutylPOSS was observed to exhibit a stronger affinity to disperse throughout the butadiene phase, due to compatibility of the POSS ‘R’ groups, greater phase volume for dispersion and reduced probability of agglomerate formation. Similar behaviour of phase selectivity manifested, resulting in the UV-visible characteristics shown in Figure 5c. Materials containing dye-functionalised isobutylPOSS (both red and blue) exhibited greater absorbance intensity because of the smaller particle domains being dispersed within the main phase of SBS, allowing for a greater amount of light absorption. This yielded films with a fuller, more intense colour. In contrast, dye-functionalised phenylPOSS, with a preference for the styrene phase, have a more constrained local environment local environment to disperse the particles and may increase the likelihood of aggregate formation, leading to inferior light-absorption properties. Interactions between chromophores may also lead to filler clustering. The UV-visible spectroscopy results correlate to the increase in colour intensity observed using colourimetry and reiterate that filler dispersion is the primary factor which dictates visual properties.

3.4. Thermal stability

The mass loss versus temperature curves of pure SBS and nanocomposites are shown in Figure 6. The decomposition of SBS shows one degradation step at ~454°C. The thermal degradation mechanism of SBS consists of two main processes, namely chain scission and crosslinking [22]. As listed in

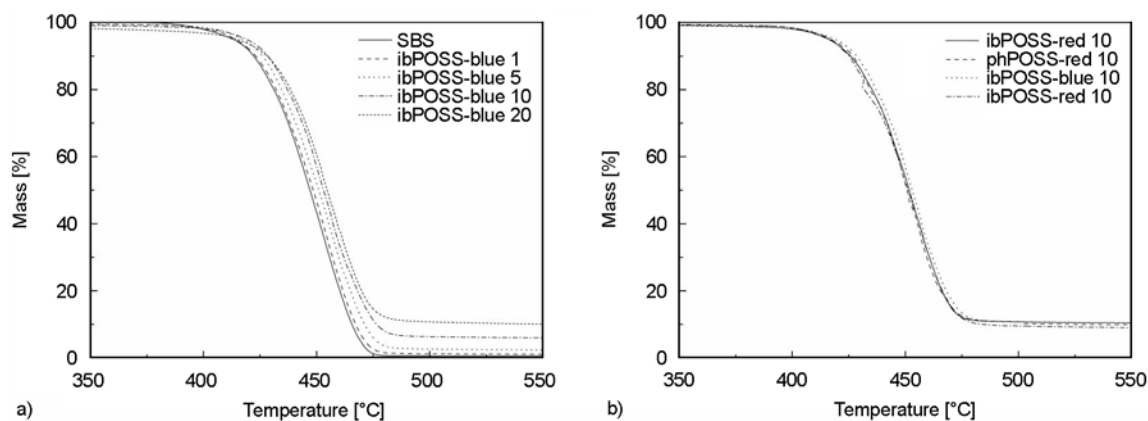


Figure 6. Mass loss curves of SBS-dye functionalised POSS composites; (a) ibPOSS-blue composites, (b) 10 wt% filled composites

Table 4. T_d values of SBS and SBS-POSS nanocomposites

Material	T_d [°C]
SBS	454
ibPOSS-blue 1	454
ibPOSS-blue 5	458
ibPOSS-blue 10	461
ibPOSS-blue 20	462
ibPOSS-red 1	455
ibPOSS-red 5	456
ibPOSS-red 10	458
ibPOSS-red 20	460
phPOSS-blue 1	456
phPOSS-blue 5	457
phPOSS-blue 10	457
phPOSS-blue 20	460
phPOSS-red 1	455
phPOSS-red 5	455
phPOSS-red 10	457
phPOSS-red 20	458

Table 4, incorporation of functionalised POSS into the SBS matrix increased the temperature at which the maximum rate of degradation occurs (T_d), with nanocomposites containing 1 wt% isobutylPOSS yielding T_d values ranging from 455–456°C. T_d continued to increase with filler content, reaching a maximum of 463°C in SBS-ibPOSS-blue-20. This behaviour is characteristic of the thermal stability of POSS which stems from its silicon-oxygen structure. A proposed mechanism of thermal reinforcement is that POSS molecules restrict polymer chain motions, due to polymer-filler interactions or by the large inertia exhibited by segments of polymer containing POSS [23, 24]. The compatibilising ‘R’ groups on the POSS encourage this interfacial interaction, allowing thermal reinforcement to be achieved. This is especially important given the

organic nature of the reactive dyes, which undergo thermal degradation at temperatures well below that of SBS. The improved thermal stability despite the presence of ‘volatile’ reactive dyes suggests effective matrix-POSS interactions and adequate thermal reinforcement by POSS molecules.

Negligible differences were observed between nanocomposites containing isobutylPOSS and phenylPOSS at concentrations of 1–5 wt%. At filler concentrations of 10 and 20 wt%, isobutylPOSS nanocomposites exhibited slightly higher T_d values than their phenylPOSS counterparts, as shown in Figure 6b. The behaviour is attributed to the dispersion of POSS within a particular phase of the SBS matrix. The thermal stability of SBS is dependent on the sensitivity of the double bonds within the continuous, butadiene phase [22, 25]. When dispersed throughout the rubber phase, POSS imparts added stiffness into the matrix by acting as crosslink points and reducing chain mobility [26, 27]. This provides thermal stability to the phase upon which the thermal degradation mechanism is dependent. Similarly, little difference was observed between materials containing blue and red dye-functionalised POSS at concentrations of 1–5 wt%. However, at higher filler loadings (10 and 20 wt%), nanocomposites containing POSS functionalised with CI Reactive Blue 4 displayed T_d values ~2–3°C higher than their CI Reactive Red 2 counterparts. Although TGA precision may account for the difference in thermal stability at higher filler concentrations, chromophore structures of the reactive dyes may also be a factor. The chromophore of CI Reactive Blue 4 is based on anthracene which is known to be quite thermally stable [28, 29]. In con-

trast, CI Reactive Red 2 contains a less-stable, naphthalene-based chromophore, which experiences thermal degradation at lower temperatures. These results indicate that thermal degradation behaviour is dependent on both the phase in which the POSS is dispersed and the structure of the bonded reactive dyes.

3.5. Thermomechanical analysis

3.5.1. Stress-strain analysis

The elastic moduli (E) of SBS and nanocomposites are presented in Figure 7. The matrix of SBS exhibited an E of 189 Pa. Addition of POSS had a positive effect on E , which increased with filler concentration, reaching a maximum at 5 wt% POSS content. The increase is characteristic of the reinforcement ability of POSS. The applied stress was transferred from the SBS matrix to the POSS filler resulting in increased strength and stiffness. This stress-transfer process was aided by sufficient interfacial adhesion between the matrix and filler, achieved through compatibilising 'R' groups on the POSS molecules. Furthermore, the dispersion obtained for these low filler nanocomposites throughout the SBS matrix contributed to the improved mechanical properties. Higher POSS concentrations (10 and 20 wt%) caused a decrease in E values. There are several possible reasons for the mechanical E reduction in higher filled nanocomposites. Verker *et al* [30] and Zhao and Schiraldi [31] attributed similar behaviour to a disruption of the polymer molecular (chain) structure brought on by POSS concentrations above 5 wt%. Liu and Zheng [32] suggested this observation is caused by a decrease in material density, due to an increase in nanocomposite porosity [33, 34]. Additionally, the crosslinking densities per unit vol-

ume can decrease with increasing POSS content, compromising the reinforcement mechanism as a consequence. The observed reduction in modulus is most probably caused by such reasons, that may be induced by filler agglomeration affecting the SBS-filler mechanisms that would normally provide good reinforcement. The agglomeration of pigment-pigment clusters, along with reduced effective crosslinking densities and potential voids deteriorate the mechanical properties, resulting in decreased modulus values [35, 36]. Furthermore, agglomerated pigment clusters can act as stress concentrators, causing premature mechanical failure. This correlates to the deterioration in optical properties associated with clustering at filler loadings above 5 wt%.

IsobutylPOSS composites yielded the greatest modulus values. This was attributed to the dispersion of POSS within the polybutadiene (rubber) phase of the SBS, facilitated by the isobutyl 'R' groups on the POSS molecule. The styrene domains within SBS act as cross-links, restricting the flow of the rubber phase and providing strength and durability. Incorporating POSS into the rubber phase provides additional reinforcement, allowing for greater amounts of stress to be transferred from the polybutadiene. The E increased with filler content, ranging from 278 and 283 Pa for 1 wt% composites of isobutyl-POSS-blue and isobutylPOSS-red, respectively, to 570 and 549 Pa for their respective 5 wt% counterparts. PhenylPOSS composites exhibited lower modulus values than composites containing isobutyl-POSS, due to the phenyl 'R' groups on the POSS molecules which provide an affinity towards the glassy, polystyrene segments within the SBS. This reduces the chance of POSS being dispersed throughout the continuous polybutadiene phase and providing adequate reinforcement. No clear distinction between the effects of the two dyes was observed. Figure 8 shows the tensile strength at yield of the nanocomposites. Similar trends were observed as per the elastic modulus, with the tensile strength at yield reaching a maximum value at 5 wt% for all nanocomposites. POSS concentrations up to and including 5 wt% provide enhanced toughness and strength by allowing sufficient stress transfer to occur. At higher concentrations, aggregation amongst the POSS particles occurred. This resulted in the possible formation of voids within the SBS-POSS

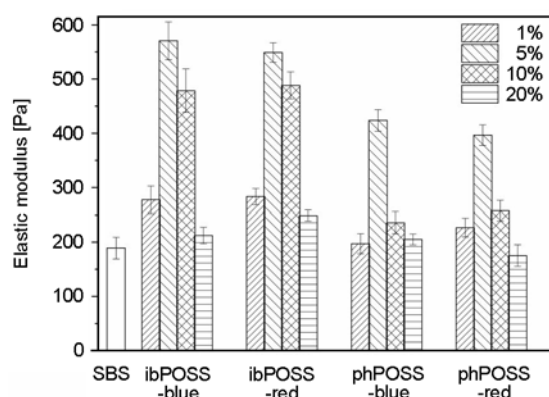


Figure 7. Elastic modulus of SBS and SBS-POSS nanocomposites

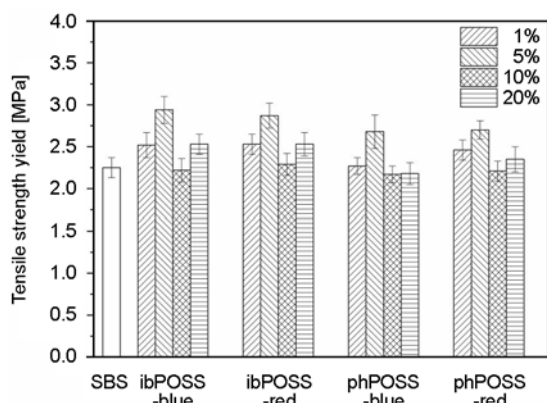


Figure 8. Tensile strength at yield of SBS and SBS-POSS nanocomposites

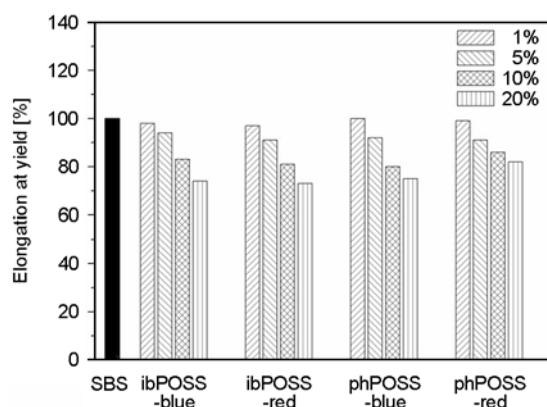


Figure 9. Elongation at yield of SBS and SBS-POSS nanocomposites

interface and the reduction in tensile strength [37]. Composites containing isobutylPOSS exhibited slightly higher values than their phenylPOSS equivalents, due to the increased reinforcement ability when POSS was dispersed throughout the continuous phase of the SBS. As a consequence of the higher modulus, elongation at yield (Figure 9) decreased with increasing POSS content for all nanocomposites. The incorporation of rigid nanoparticles into an

elastomer imparts stiffness, decreasing the elasticity and ductility.

3.5.2. Creep-recovery analysis

The creep-recovery curves of SBS and ibPOSS-red filled composites are shown in Figure 10a. Creep deformation decreased with increasing POSS content. This was expected of an elastomer filled with rigid reinforcement. Due to its ceramic silica structure, the presence of POSS imparts stiffness into the matrix. This restricts the molecular motions of the polybutadiene chains, resulting in less deformation. Furthermore, the compatibilising organic groups on the POSS encourage further interaction and adhesion between the matrix and filler, allowing for the nanocomposites to withstand greater levels of stress without experiencing deformation. At higher POSS loadings (10 and 20 wt%), nanocomposites exhibited flatter creep curves with a lower viscosity component, indicating a decrease of deformation of the elastic component. Nanocomposites containing isobutylPOSS exhibited less deformation than their phenylPOSS counterparts, which was in agreement with the stress-strain results. Since the polybutadiene chains which comprise the rubbery, continuous phase experience molecular rearrangement and motions under stress, it is more effective to disperse filler throughout this phase in order to reduce deformation.

When comparing the curves of the blue and red dye-nanocomposites (Figure 10b), a significant difference in creep behaviour is evident. Nanocomposites containing POSS functionalised with CI Reactive Blue 4 showed considerably less creep and deformation than those containing CI Reactive Red 2. This occurrence can be attributed to the dif-

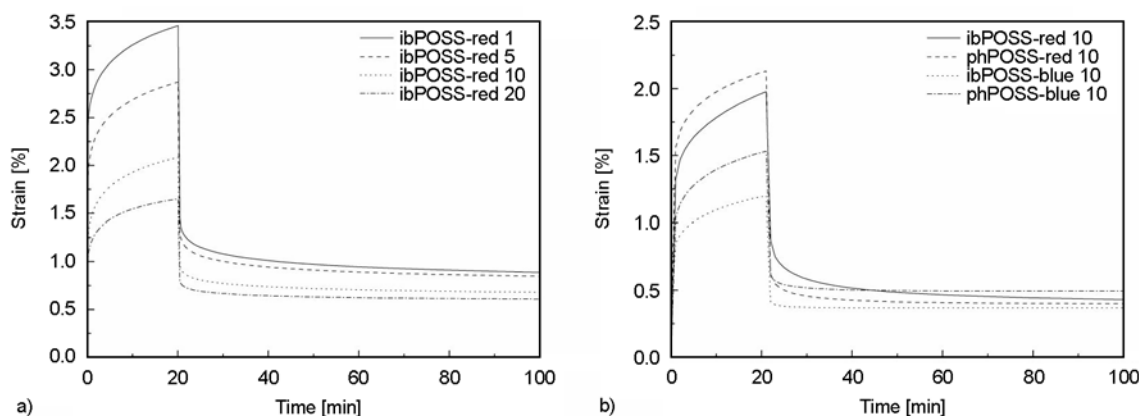


Figure 10. (a) Creep-recovery curves of ibPOSS-red nanocomposites, (b) creep-recovery curves of 10 wt% filled nanocomposites

ference in chromophore structure of the dyes (refer Table 2). The anthracene-based chromophore of CI Reactive Blue 4 is considerably bulkier and extends further from the dichlorotriazine reactive group than the naphthalene-based chromophore of CI Reactive Red 2. These features provide additional restraints on molecular motions, resulting in the matrix exhibiting less creep and deformation. Hence the dye can impart some physical constraints to dimensional stability.

The parameters of the four-element model were calculated for the creep component of SBS and the nanocomposites, which is presented in Table 5. The Maxwell modulus (E_1) was observed to increase with POSS content, confirming that the nano-sized fillers influence the flow of the SBS matrix. This behaviour correlates to an increase in Maxwell viscosity (η_1), which indicates improved resistance to deformation. Nanocomposites containing isobutyl-POSS displayed larger E_1 and η_1 values than their phenylPOSS counterparts treated with the same dye. Similarly, composites with CI Reactive Blue 4-functionalised POSS yielded higher values than those functionalised with CI Reactive Red 2. These parameters provide an accurate representation of what was observed experimentally. All materials displayed a certain proportion of unrecovered strain that is characteristic of viscoelastic materials such as SBS. This is due to irreversible chain entanglement slippage and detachment of styrene domains from the polybutadiene rubber-phase which occurs

during the application of load. Permanent deformation increased with POSS concentration, with nanocomposites containing blue-functionalised isobutyl-POSS displaying the largest values. Higher concentrations of filler, such as POSS, restrict the relaxation of SBS chains, causing irreversible chain slippage and unravelling. The Voigt viscosity (η_2) was observed to increase with POSS content, suggesting an increase in resistance of the SBS chains to uncoiling.

Increasing the POSS content caused the τ to decrease, suggesting that the nanocomposites become more solid-like in behaviour at higher filler concentrations. Similarly, highly filled composites exhibited flatter recovery curves, indicating a faster recovery of the viscoelastic component. Nanocomposites containing phenylPOSS displayed slightly longer τ than their isobutylPOSS counterparts treated with the same-coloured dye. When rubbery, polybutadiene chains are highly stretched under an applied load, phenylPOSS molecules can become detached from the glassy styrene domains for which they have an affinity. This can lead to dissimilar block-mixing occurring in interfacial regions, causing an increase in permanent deformation [38]. Nanocomposites functionalised with CI Reactive Blue 4 yielded longer τ than those functionalised with CI Reactive Red 2. This was once again attributed to the increased restrictions placed on segmental motions for relaxation by the bulkier, blue-coloured chromophore, causing the material to behave in a more solid-like nature. These results correlate well to the

Table 5. Creep-recovery data of SBS and SBS-POSS nanocomposites

Material	E_1 [MPa]	η_1 [MPa·s ⁻¹]	E_2 [MPa]	η_2 [MPa·s ⁻¹]	τ [min]	Permanent deformation [%]
SBS	0.22	67.91	0.35	3.31	9.46	18
ibPOSS-blue 1	0.26	77.04	0.74	6.17	8.33	23
ibPOSS-blue 5	0.34	85.06	1.24	8.79	7.09	29
ibPOSS-blue 10	0.57	103.79	1.58	13.65	6.94	33
ibPOSS-blue 20	0.81	154.36	2.48	16.37	6.60	37
ibPOSS-red 1	0.22	72.77	0.65	5.70	8.77	23
ibPOSS-red 5	0.26	78.84	0.87	7.03	8.08	25
ibPOSS-red 10	0.47	91.32	1.08	8.53	7.90	30
ibPOSS-red 20	0.47	138.25	1.62	11.43	7.05	34
phPOSS-blue 1	0.20	73.61	0.71	6.09	8.58	20
phPOSS-blue 5	0.31	80.81	1.14	8.53	7.48	28
phPOSS-blue 10	0.43	104.67	1.47	10.66	7.25	32
phPOSS-blue 20	0.71	145.64	2.16	14.95	6.92	34
phPOSS-red 1	0.21	70.92	0.48	4.35	9.06	19
phPOSS-red 5	0.22	72.24	0.73	6.58	9.01	21
phPOSS-red 10	0.35	89.31	0.99	8.37	8.45	24
phPOSS-red 20	0.44	133.70	1.33	10.97	8.24	29

Table 6. KWW parameters of SBS and SBS-POSS nanocomposites

Material	A	β	τ [s]
SBS	3.18	0.14	35.74
ibPOSS-blue 1	2.36	0.09	30.84
ibPOSS-blue 5	1.91	0.04	24.97
ibPOSS-blue 10	1.05	0.01	15.60
ibPOSS-blue 20	0.84	0.01	12.20
ibPOSS-red 1	2.66	0.10	27.60
ibPOSS-red 5	2.39	0.07	24.60
ibPOSS-red 10	2.48	0.05	23.40
ibPOSS-red 20	2.10	0.04	18.10
phPOSS-blue 1	2.54	0.11	32.90
phPOSS-blue 5	2.16	0.05	24.70
phPOSS-blue 10	1.56	0.03	20.40
phPOSS-blue 20	1.34	0.02	17.60
phPOSS-red 1	2.94	0.12	31.50
phPOSS-red 5	2.31	0.09	27.90
phPOSS-red 10	1.77	0.06	23.00
phPOSS-red 20	1.29	0.04	17.80

behaviour observed in the creep component and stress-strain analysis, with the time scale allowing the more subtle effects of phase preference, filler concentration and chromophore structure to become observable.

In order to further examine relaxation behaviour, the KWW stretched exponential function was applied to SBS and the nanocomposites. The results are presented in Table 6. In fitting the function, the pre-exponential constant and relaxation time decreased with increasing POSS content. This was to be expected since the relaxation provides an indication of the degree of mobility molecules within the polymer possess. The decreased relaxation time at higher POSS concentrations is indicative of the solid-like behaviour highly-filled nanocomposites exhibit and is in agreement with the creep data obtained using the four-element model. Correspondingly, the shape fitting parameter β changed with POSS content. The value of β is influenced by various factors, including structure, the presence of fillers, crosslinks and crystallinity [39]. These observations strongly suggest that the nanocomposites experience restricted flow, attributed to the incorporation of functionalised-POSS.

3.5.3. Modulated force-thermomechanometry

Figure 11 shows the storage modulus (E') of SBS and selected nanocomposites. Nanocomposites containing POSS displayed higher E' values than pure

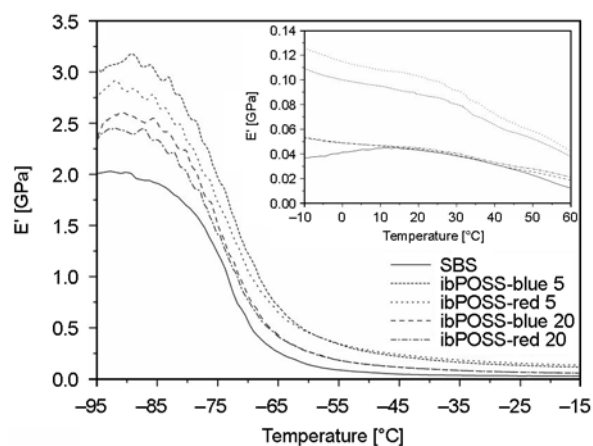


Figure 11. Storage modulus (E') curves across the polybutadiene glass-rubber transition of SBS and ibPOSS-filled composites. Inset shows the E' behaviour above the polybutadiene T_g

SBS. The E' modulus reached a maximum at POSS concentrations of 5 wt%, with SBS-ibPOSS-blue 5 and SBS-ibPOSS-red 5 exhibiting E' values of 3.1 and 2.8 GPa at -90°C , respectively. Similar observations were recorded before the styrene transition at 10°C , with maximum E' values of 0.11 and 0.10 GPa for SBS-ibPOSS-blue 5 and SBS-ibPOSS-red 5, respectively. These results are indicative of the additional stiffness imparted by POSS. As filler content was increased past 5 wt%, the modulus began to decrease, suggesting that after a critical concentration (~ 5 wt%), POSS begins to lose reinforcing ability in this nanocomposites system. Filler agglomeration at higher concentrations reduces the particle surface area available to interact with the polymer, resulting in less-effective reinforcement. Zucchi *et al.* [40] attributed this reduction in elastic modulus to a decrease in the cohesive energy density caused by higher POSS concentrations. POSS functionalised with blue dye and containing isobutyl compatibilising groups exhibited the highest modulus values, attributed to the influence of dye structure and phase preference, respectively, on mechanical properties. This influence of dye-structure on mechanical properties is in agreement with behaviour observed in creep-recovery analysis. At temperatures above the polybutadiene transition, composites displayed higher E' values compared to pure SBS, while an increase in E' reduction rate was observed at temperatures above the polystyrene glass transition.

The loss modulus (E'') of SBS and nanocomposites is shown in Figure 12, while T_g values are sum-

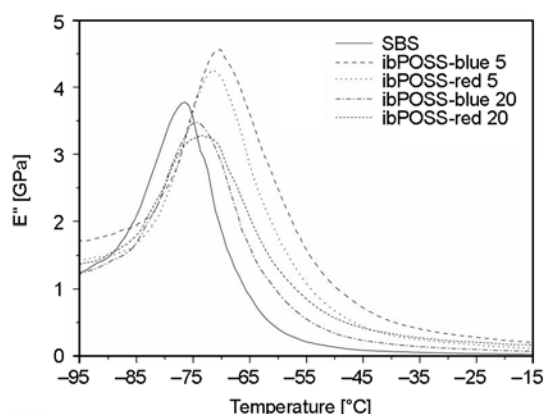


Figure 12. Loss modulus (E'') curves across the polybutadiene glass-rubber transition of SBS and ibPOSS-filled composites

marised in Table 7. The T_g is determined by the peak of the E'' curve (E''_{max}), since that is where maximum heat dissipation occurs. The curve of pure SBS displays two peaks, at -75 and 88°C . These peaks correspond to the T_g of the butadiene and styrene phases, respectively. Addition of POSS caused the T_g to increase in both phases, reaching a maximum at 5 wt%, before decreasing at higher concentrations. The initial increase in glass transition temperature is attributed to the ability of the functionalised-POSS to restrict molecular relaxation motions and bond rotations of the polymer chains. The decrease in loss (and storage) modulus at higher POSS concentrations has been observed previously [7, 35] and suggests that POSS exhibits a plasticising effect at sufficiently high levels. POSS agglomeration at concentrations greater than 5 wt% is also believed to be responsible for the decrease in moduli and T_g , as suggested by Kim *et al.* [35].

As displayed in Table 7, composites containing isobutylPOSS displayed the greatest increase in T_g for the butadiene phase, with ibPOSS-blue 5 and

ibPOSS-red 5 yielding T_g values of -70 and -71°C , respectively. Similarly, materials filled with phenyl-POSS exhibited higher T_g values in the styrene phase than their isobutylPOSS counterparts. This behaviour suggests that the compatibilising groups are providing an affinity for their corresponding phases, allowing the POSS to disperse throughout and entangle within a particular phase within the SBS. Despite being dispersed throughout the rubbery phase, isobutylPOSS increased the styrene phase T_g at concentrations up to 5 wt%, before decreasing with additional POSS content. Fu *et al.* [18] observed similar results, attributing the behaviour to an equal distribution of stress across both domains at temperatures near the styrene phase T_g ($\sim 88^\circ\text{C}$). This arises from the similar behaviour of the butadiene and styrene phases at this temperature, allowing the POSS molecules to act as physical crosslinks and reduce segmental relaxation. PhenylPOSS showed a similar, although less intense influence over the butadiene phase.

Nanocomposites functionalised with CI Reactive Blue 4 displayed slightly higher T_g values than those treated with CI Reactive Red 2. This was due to the bulkier structure of the blue-dye chromophore which allows for additional restraints on molecular motions. Nanocomposites exhibited glass transitions over a larger temperature range, as indicated by the broader E'' peaks. The increase in peak breadth is attributed to an increase in the segmental relaxation times of the matrix [41]. Peak breadth was observed to increase with POSS concentration, reaching maximum values at loadings of 10 and 20 wt%, suggesting an increase in the relaxation time due to segmental constraints, including polymer chain coupling and polymer-POSS interactions.

Table 7. Glass transition data of SBS and selected nanocomposites

Material	T_g from E'_{max} [$^\circ\text{C}$]		T_g from $\tan \delta_{max}$ [$^\circ\text{C}$]		E' [MPa]	
	α	β	α	β	-90°C	10°C
SBS	-75	88	-67	95	2.0	0.03
ibPOSS-blue 5	-70	89	-62	94	3.1	0.11
ibPOSS-blue 20	-73	85	-64	97	2.6	0.04
ibPOSS-red 5	-71	88	-63	93	2.8	0.10
ibPOSS-red 20	-72	86	-64	90	2.4	0.05
phPOSS-blue 5	-73	93	-65	99	2.5	0.05
phPOSS-blue 20	-76	90	-68	97	2.2	0.04
phPOSS-red 5	-73	92	-66	98	2.3	0.04
phPOSS-red20	-76	91	-69	98	2.2	0.04

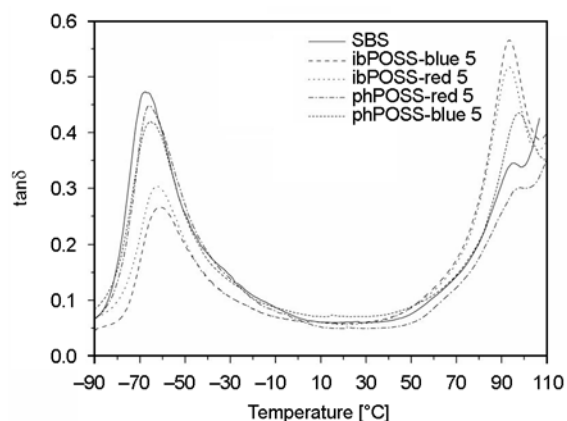


Figure 13. Loss tangent ($\tan\delta$) of SBS and 5 wt% filled composites

The loss tangent ($\tan\delta$) of SBS and several nanocomposites is shown in Figure 13. The maximum of the $\tan\delta$ curve can be used to determine T_g , although the E'' maximum is shown to be more consistent with other determinations of T_g . The $\tan\delta$ were ~ 6 – 9°C higher than T_g obtained from loss modulus curves (refer Table 6). The glass transition temperatures obtained from the loss tangent maximum displayed similar trends to those obtained from E''_{max} . Nanocomposites containing isobutylPOSS showed a reduction in butadiene-phase peak height, with 5 wt% exhibiting the greatest reduction. At concentrations above 5 wt%, the peaks began to increase towards the initial location of SBS. Conversely, the addition of isobutylPOSS caused an increase in the styrene-phase peak, reaching a maximum at 5 wt% before reducing at higher loadings. The amplitude of the $\tan\delta$ peak provides an indication of the number of kinetic units mobile enough to contribute to the glass transition [42]. The decrease in peak intensity indicates that isobutylPOSS molecules restrict motions of polymer chains within the butadiene phase, as indicated by the isobutylPOSS nanocomposites displaying T_g values higher than SBS. The increase peak height of the styrene phase indicates isobutylPOSS exerts a plasticising effect on the glassy domains, leading to composites displaying similar or lower T_g values than SBS. PhenylPOSS-blue nanocomposites experienced an increase in styrene-phase peak intensity, while a decrease was observed in phenylPOSS-red nanocomposites. This was particularly interesting since the blue-functionalised materials exhibited the greatest increase in T_g , which is usually characterised by a reduction in $\tan\delta$ peak intensity. The damping ability of a filled

polymer system is believed to be influenced by two factors; (a) the amount of free volume, (b) internal friction between the filler and matrix and between the filler particles themselves across the glass transition region [43]. The latter increases as the number of chain movements become greater, leading to an increase in damping ability. PhenylPOSS functionalised with bulkier CI Reactive Blue 4 experienced a greater amount of internal friction within the SBS matrix than its CI Reactive Red 2 counterpart, resulting in greater damping ability and internal friction.

The addition of phenylPOSS caused no increase in the butadiene-phase peak, which was expected since the styrene domains within SBS provide the polymer with rigidity and structure. As with the E'' curves, peak broadening of the $\tan\delta$ curves was observed at higher filler loadings. Since the peak breadth is an indication of structural heterogeneity (β parameter in KWW equation), the wider peaks suggest an increase in segmental relaxation time due to increased SBS-POSS interactions. The broader peaks are also indicative of the aforementioned increase in damping and internal friction.

4. Conclusions

POSS molecules were successfully functionalised with dichlorotriazine reactive dyes as indicated by FTIR and incorporated into SBS via physical blending. Agglomerate size and frequency increased with filler content, due to increased inter-POSS and inter-chromophore interactions. The morphology of the nanocomposites was dependent on the R groups on the POSS cages, with the amount of filler agglomeration being dependent on the relative volume of butadiene or styrene phase to disperse throughout. Colour intensity was able to be controlled by altering the functionalised POSS concentration. Films displayed uniform and smooth colour distribution at concentrations up to and including 5 wt%. Higher filler loadings resulted in colour swirling and fleck formation, due to increased filler diameters. Functionalised isobutylPOSS provided the greatest uniformity of colour, due to the greater amount of polymer (polybutadiene phase) which the POSS can be dispersed throughout. The use of dye-functionalised POSS as a pigment displayed limited success; at concentrations greater than 5 wt% surface treatment of the chromophore or further

processing (shear, greater ultrasonication, etc) are required to prevent filler agglomeration.

The thermal stability of SBS was enhanced by the addition of functionalised POSS. IsobutylPOSS had the greatest influence on thermal stability, due to its incorporation into the thermally-sensitive polybutadiene phase. POSS functionalised with CI Reactive Blue 4 exhibited a marginally better influence on thermal stability than its CI Reactive Red 2 counterpart, due to the thermal stability of the anthracene-based chromophore of CI Reactive Blue 4. The tensile modulus (E) of the nanocomposites increased with filler content, reaching a maximum at 5 wt%. Creep deformation decreased and permanent strain increased with POSS content, due to the restricted molecular motions caused by filler. Incorporation of POSS increased the storage modulus (E'), loss modulus (E'') and glass transition temperature (T_g), all reaching maximum values at filler concentrations of 5 wt%. The decrease in mechanical properties at POSS concentrations above 5 wt% was attributed to a disruption of the polymer molecular structure due to excess filler loading and reduction in material density. Three factors contributed to the mechanical properties of the nanocomposites; (a) POSS concentration, (b) the phase which the POSS was dispersed throughout, (c) chemical structure of the dye. The optimal POSS concentration was deemed to be 5 wt%.

Acknowledgements

The authors acknowledge financial support from the CRC for Polymers.

References

- [1] Bianchi C., Noor S., Mirley C. L., Bauer R., Yener D.: U.S. Patent 7479324, USA (2009).
- [2] Jeon Y-M., Lim T-H., Lee C-W., Cheon J-W., Gong M-S.: Preparation of fluorescent silica-core red fluorophore and their chemiluminescent properties in colloidal solution. *Journal of Industrial and Engineering Chemistry*, **13**, 518–522 (2007).
- [3] Winnik F. M., Keoshkerian B., Fuller J. R., Hofstra P. G.: New water-dispersible silica-based pigments: Synthesis and characterization. *Dyes and Pigments*, **14**, 101–112 (1990).
DOI: [10.1016/0143-7208\(90\)87010-Z](https://doi.org/10.1016/0143-7208(90)87010-Z)
- [4] DeArmitt C., Wheeler P.: POSS keeps high temperature plastics flowing. *Plastics Additives and Compounding*, **10**, 36–39 (2008).
DOI: [10.1016/S1464-391X\(08\)70134-X](https://doi.org/10.1016/S1464-391X(08)70134-X)
- [5] Scott D. W.: Thermal rearrangement of branched-chain methylpolysiloxanes. *Journal of the American Chemical Society*, **68**, 356–358 (1946).
DOI: [10.1021/ja01207a003](https://doi.org/10.1021/ja01207a003)
- [6] Froehlich J. D., Young R., Nakamura T., Ohmori Y., Li S., Mochizuki A., Lauters M., Jabbour G. E.: Synthesis of multi-functional POSS emitters for OLED applications. *Chemistry of Materials*, **19**, 4991–4997 (2007).
DOI: [10.1021/cm070726v](https://doi.org/10.1021/cm070726v)
- [7] Wheeler P. A., Fu B. X., Lichtenhan J. D., Weitao J., Mathias L. J.: Incorporation of metallic POSS, POSS copolymers, and new functionalized POSS compounds into commercial dental resins. *Journal of Applied Polymer Science*, **102**, 2856–2862 (2006).
DOI: [10.1002/app.24645](https://doi.org/10.1002/app.24645)
- [8] García O., Sastre R., García-Moreno I., Martín V., Costela A.: New laser hybrid materials based on POSS copolymers. *Journal of Physical Chemistry C*, **112**, 14710–14713 (2008).
DOI: [10.1021/jp8064097](https://doi.org/10.1021/jp8064097)
- [9] Hartmann-Thompson C., Keeley D., Pollock K. M., Dvornic P. R., Keinath S. E., Dantus M., Gunaratne T. C., LeCaptain D. J.: One- and two-photon fluorescent polyhedral oligosilsesquioxane (POSS) nanosensor arrays for the remote detection of analytes in clouds, in solution, and on surfaces. *Chemistry of Materials*, **20**, 2829–2838 (2008).
DOI: [10.1021/cm703641s](https://doi.org/10.1021/cm703641s)
- [10] Adhikari R., Michler G. H.: Influence of molecular architecture on morphology and micromechanical behavior of styrene/butadiene block copolymer systems. *Progress in Polymer Science*, **29**, 949–986 (2004).
DOI: [10.1016/j.progpolymsci.2004.06.002](https://doi.org/10.1016/j.progpolymsci.2004.06.002)
- [11] Park C., Yoon J., Thomas E. L.: Enabling nanotechnology with self assembled block copolymer patterns. *Polymer*, **44**, 6725–6760 (2003).
DOI: [10.1016/j.polymer.2003.08.011](https://doi.org/10.1016/j.polymer.2003.08.011)
- [12] Balsamo V., Lorenzo A. T., Müller A. J., Corona-Galván S., Trillo L. M. F., Quiteria V. R. S.: Structure, properties and applications of ABA and ABC triblock copolymers with hydrogenated polybutadiene blocks. in 'Block copolymers in nanoscience' (eds.: Lazzari M., Liu G., Lecommandoux S.) Wiley, Weinheim, 367–390 (2006).
- [13] Choi S-S.: Properties of silica-filled styrene-butadiene rubber compounds containing acrylonitrile-butadiene rubber: The influence of the acrylonitrile-butadiene rubber type. *Journal of Applied Polymer Science*, **85**, 385–393 (2002).
DOI: [10.1002/app.10614](https://doi.org/10.1002/app.10614)
- [14] Praveen S., Chattopadhyay P. K., Albert P., Dalvi V. G., Chakraborty B. C., Chattopadhyay S.: Synergistic effect of carbon black and nanoclay fillers in styrene butadiene rubber matrix: Development of dual structure. *Composites Part A: Applied Science and Manufacturing*, **40**, 309–316 (2009).
DOI: [10.1016/j.compositesa.2008.12.008](https://doi.org/10.1016/j.compositesa.2008.12.008)

- [15] Chen Z., Feng R.: Preparation and characterization of poly(styrene-*b*-butadiene-*b*-styrene)/montmorillonite nanocomposites. *Polymer Composites*, **30**, 281–287 (2009).
DOI: [10.1002/pc.20631](https://doi.org/10.1002/pc.20631)
- [16] Drazkowski D. B., Lee A., Haddad T. S., Cookson D. J.: Chemical substituent effects on morphological transitions in styrene-butadiene-styrene triblock copolymer grafted with polyhedral oligomeric silsesquioxanes. *Macromolecules*, **39**, 1854–1863 (2006).
DOI: [10.1021/ma0518813](https://doi.org/10.1021/ma0518813)
- [17] Drazkowski D. B., Lee A., Haddad T. S.: Morphology and phase transitions in styrene-butadiene-styrene triblock copolymer grafted with isobutyl-substituted polyhedral oligomeric silsesquioxanes. *Macromolecules*, **40**, 2798–2805 (2007).
DOI: [10.1021/ma062393d](https://doi.org/10.1021/ma062393d)
- [18] Fu B. X., Lee A., Haddad T. S.: Styrene-butadiene-styrene triblock copolymers modified with polyhedral oligomeric silsesquioxanes. *Macromolecules*, **37**, 5211–5218 (2004).
DOI: [10.1021/ma049753m](https://doi.org/10.1021/ma049753m)
- [19] Williams G., Watts D. C.: Non-symmetrical dielectric relaxation behaviour arising from a simple empirical decay function. *Transactions of the Faraday Society*, **66**, 80–85 (1970).
DOI: [10.1039/TF9706600080](https://doi.org/10.1039/TF9706600080)
- [20] Goldschmidt A., Streitberger H. J.: BASF handbook on basics of coating technology. Vincentz Network, Hannover (2003).
- [21] Markarian J.: Back-to-basics: Adding colour to plastics. *Plastics, Additives and Compounding*, **11**, 12–15 (2009).
DOI: [10.1016/S1464-391X\(09\)70106-0](https://doi.org/10.1016/S1464-391X(09)70106-0)
- [22] Xu J., Zhang A., Zhou T., Cao X., Xie Z.: A study on thermal oxidation mechanism of styrene-butadiene-styrene block copolymer (SBS). *Polymer Degradation and Stability*, **92**, 1682–1691 (2007).
DOI: [10.1016/j.polymdegradstab.2007.06.008](https://doi.org/10.1016/j.polymdegradstab.2007.06.008)
- [23] Liu Y. R., Huang Y. D., Liu L.: Effects of TriSilanolisobutyl-POSS on thermal stability of methylsilicone resin. *Polymer Degradation and Stability*, **91**, 2731–2738 (2006).
DOI: [10.1016/j.polymdegradstab.2006.04.031](https://doi.org/10.1016/j.polymdegradstab.2006.04.031)
- [24] Romo-Uribe A., Mather P. T., Haddad T. S., Lichtenhan J. D.: Viscoelastic and morphological behavior of hybrid styryl-based polyhedral oligomeric silsesquioxane (POSS) copolymers. *Journal of Polymer Science Part B: Polymer Physics*, **36**, 1857–1872 (1998).
DOI: [10.1002/\(SICI\)1099-0488\(199808\)36:11<1857::AID-POLB7>3.0.CO;2-N](https://doi.org/10.1002/(SICI)1099-0488(199808)36:11<1857::AID-POLB7>3.0.CO;2-N)
- [25] Lu L., Yu H., Wang S., Zhang Y.: Thermal degradation behavior of styrene-butadiene-styrene tri-block copolymer/ultrawalled carbon nanotubes composites. *Journal of Applied Polymer Science*, **112**, 524–531 (2009).
DOI: [10.1002/app.29414](https://doi.org/10.1002/app.29414)
- [26] Sim L. C., Ramanan S. R., Ismail H., Seetharamu K. N., Goh T. J.: Thermal characterization of Al₂O₃ and ZnO reinforced silicone rubber as thermal pads for heat dissipation purposes. *Thermochimica Acta*, **430**, 155–165 (2008).
DOI: [10.1016/j.tca.2004.12.024](https://doi.org/10.1016/j.tca.2004.12.024)
- [27] Zhang J., Feng S., Ma Q.: Kinetics of the thermal degradation and thermal stability of conductive silicone rubber filled with conductive carbon black. *Journal of Applied Polymer Science*, **89**, 1548–1554 (2003).
DOI: [10.1002/app.12277](https://doi.org/10.1002/app.12277)
- [28] Ma M., Sun G.: Antimicrobial cationic dyes: Part 2 – Thermal and hydrolytic stability. *Dyes and Pigments*, **63**, 39–49 (2004).
DOI: [10.1016/j.dyepig.2004.01.004](https://doi.org/10.1016/j.dyepig.2004.01.004)
- [29] Mahmoud A. S., Ghaly A. E., Brooks S. L.: Influence of temperature and pH on the stability and colorimetric measurement of textile dyes. *American Journal of Biochemistry and Biotechnology*, **3**, 33–41 (2007).
DOI: [10.3844/ajbbsp.2007.33.41](https://doi.org/10.3844/ajbbsp.2007.33.41)
- [30] Verker R., Grossman E., Gouzman I., Eliaz N.: TriSilanolPhenyl POSS-polyimide nanocomposites: Structure-properties relationship. *Composites Science and Technology*, **69**, 2178–2184 (2009).
DOI: [10.1016/j.compscitech.2009.06.001](https://doi.org/10.1016/j.compscitech.2009.06.001)
- [31] Zhao Y., Schiraldi D. A.: Thermal and mechanical properties of polyhedral oligomeric silsesquioxane (POSS)/polycarbonate composites. *Polymer*, **46**, 11640–11647 (2005).
DOI: [10.1016/j.polymer.2005.09.070](https://doi.org/10.1016/j.polymer.2005.09.070)
- [32] Liu H., Zheng S.: Polyurethane networks nanoreinforced by polyhedral oligomeric silsesquioxane. *Macromolecular Rapid Communications*, **26**, 196–200 (2005).
DOI: [10.1002/marc.200400465](https://doi.org/10.1002/marc.200400465)
- [33] Leu C-M., Reddy M., Wei K-H., Shu C-F.: Synthesis and dielectric properties of polyimide-chain-end tethered polyhedral oligomeric silsesquioxane nanocomposites. *Chemistry of Materials*, **15**, 2261–2265 (2003).
DOI: [10.1021/cm0208408](https://doi.org/10.1021/cm0208408)
- [34] Leu C-M., Chang Y-T., Wei K-H.: Polyimide-side-chain tethered polyhedral oligomeric silsesquioxane nanocomposites for low-dielectric film applications. *Chemistry of Materials*, **15**, 3721–3727 (2003).
DOI: [10.1021/cm030393b](https://doi.org/10.1021/cm030393b)
- [35] Kim E. H., Myoung S. W., Jung Y. G., Paik U.: Polyhedral oligomeric silsesquioxane-reinforced polyurethane acrylate. *Progress in Organic Coatings*, **64**, 205–209 (2009).
DOI: [10.1016/j.porgcoat.2008.07.026](https://doi.org/10.1016/j.porgcoat.2008.07.026)
- [36] Yang C-C., Chang F-C., Wang Y-Z., Chan C-M., Lin C-L., Chen W-Y.: Novel nanocomposite of epoxy resin by introduced reactive and nanoporous material. *Journal of Polymer Research*, **14**, 431–439 (2007).
DOI: [10.1007/s10965-007-9115-9](https://doi.org/10.1007/s10965-007-9115-9)

- [37] Lee S-I., Kim D-K., Sin J-H., Lee Y-S., Nah C.: Polyurethane/silica composites, prepared via in-situ polymerization in the presence of chemically modified silicas. *Journal of Industrial Engineering Chemistry*, **13**, 786–792 (2007).
- [38] Blackwell R. I., Mauritz K. A.: Mechanical creep and recovery of poly(styrene-*b*-ethylene/butylene-*b*-styrene) (SEBS), sulfonated SEBS (sSEBS), and sSEBS/silicate nanostructured materials. *Polymers for Advanced Technologies*, **16**, 212–220 (2005).
DOI: [10.1002/pat.574](https://doi.org/10.1002/pat.574)
- [39] Kaminski D., Shanks R.: Static creep and recovery of filled elastomers using thermomechanometry. in ‘32nd Condensed Matter and Materials Meeting’ Wagga Wagga, Australia, p4 (2008).
- [40] Zucchi I. A., Galante M. J., Williams R. J. J.: Surface energies of linear and cross-linked polymers based on isobornyl methacrylate and methacryl-heptaisobutyl POSS. *European Polymer Journal*, **45**, 325–331 (2009).
DOI: [10.1016/j.eurpolymj.2008.10.025](https://doi.org/10.1016/j.eurpolymj.2008.10.025)
- [41] Verghese K. N. E., Jensen R. E., Lesko J. J., Ward T. C.: Effects of molecular relaxation behavior on sized carbon fiber–vinyl ester matrix composite properties. *Polymer*, **42**, 1633–1645 (2001).
DOI: [10.1016/S0032-3861\(00\)00351-7](https://doi.org/10.1016/S0032-3861(00)00351-7)
- [42] Kennedy J. E., Lyons J. G., Geever L. M., Higginbotham C. L.: Synthesis and characterisation of styrene butadiene styrene-g-acrylic acid for potential use in biomedical applications. *Materials Science and Engineering C*, **29**, 1655–1661 (2009).
DOI: [10.1016/j.msec.2009.01.015](https://doi.org/10.1016/j.msec.2009.01.015)
- [43] Trakulsujaritchook T., Hourston D. J.: Damping characteristics and mechanical properties of silica filled PUR/PEMA simultaneous interpenetrating polymer networks. *European Polymer Journal*, **42**, 2968–2976 (2006).
DOI: [10.1016/j.eurpolymj.2006.07.028](https://doi.org/10.1016/j.eurpolymj.2006.07.028)

Side chain polysiloxanes with phthalocyanine moieties

T. Ganicz*, T. Makowski, W. A. Stanczyk, A. Tracz

Centre of Molecular and Macromolecular Studies, Polish Academy of Sciences, Sienkiewicza 112, 90-363 Lodz, Poland

Received 7 September 2011; accepted in revised form 30 November 2011

Abstract. Side chain polysiloxane with 5-(pentyloxy)-3-methyloxy-9,10,16,17,23,24-hexakis(octenyloxy)phthalocyanine moieties is synthesized by hydrosilylation reaction. The phase behavior and thermo-optical properties of the polysiloxane and starting 2-(pent-4-enyloxy)-3-methyloxy-9,10,16,17,23,24-hexakis(octenyloxy)phthalocyanine is examined by POM (Polarizing optical microscopy), TOA (thermo-optical analysis), DSC (differential scanning calorimetry), AFM (atomic force microscopy) and SAXS (small angle X-ray scattering) studies. The effect of the attachment of phthalocyanine to polysiloxane chains over phase transitions and phase morphology is discussed in details.

Keywords: thermal properties, polysiloxanes, phthalocyanines, electro-optical properties, polymer synthesis

1. Introduction

Phthalocyanines are one of the most studied classes of organic functional materials with high potential in electrooptics. Due to their 18-p electron macrocyclic aromatic system, closely related to that of the naturally occurring porphyrin ring, and relative facile tailoring of molecular structure by chemical modification, they found numerous commercial applications, among others: photoconductors in xerography [1], optical data storage [2], solar energy conversion [3], electrochromic and electroluminescent displays [4].

One of the most studied area of the application of phthalocyanines are organic thin film transistors (OTFT) as a potential replacement for silicon-based devices [5], as well as new electronic devices based on field transistor technology such as electronic paper [6] and various types of sensors [7].

Usefulness of low molecular phthalocyanines as a material for OTFT sensors has been already proved [8], however in many cases mechanical resistance of their thin films is not satisfactory. In order to improve mechanical properties of these materials it

is possible to polymerize them or attach them as a side chains to various polymer main chains. Such the polymers may also have an increased tendency to form columnar or calamitic mesophases which might help to obtain thin films with high order of molecular self-organization. However most of the phthalocyanine polymers studied till now, exhibit too high transition temperatures and too low solubility to be used for formation of thin films with good mechanical resistance [9].

Therefore, it was decided to attach phthalocyanines as side chains to polysiloxane, the backbone well known for its high flexibility, leading thus, to materials with lower transition temperatures compared to other polymers [10].

2. Experimental section

2.1. Materials and methods

2.1.1. Substrates

All organometallic syntheses were carried out under argon with exclusion of moisture. Catechol (Aldrich, Germany), Guajacol (Aldrich), bromine (‘Polskie Odczynniki Chemiczne’ – POCh, Poland), glacial

*Corresponding author, e-mail: tg@cbmm.lodz.pl

acetic acid (POCh), NaHCO₃ (POCh), K₂CO₃ (POCh) MgSO₄ (POCh), FeCl₃ (POCh), HCl aq. 37% (POCh), 1-bromo-octane (Aldrich), ethanol absolute (POCh), DBN (Aldrich), chloroform (POCh), poly(methylhydrosiloxane) 30cSt. (ABCR, Germany), 3,6-dihydroxyphthalonitrile (Aldrich) – have been used as supplied.

Methylene chloride (POCh), toluene (POCh), DMF (dimethylformamide, POCh) were dried by standard methods and stored over molecular sieves or sodium mirror [11].

4,5-dibromocatechol [12], 4,5-dihydroxyphthalonitrile [13], 4,5-dibromo-2-methoxyphenol [14], 4-hydroxy-5-methoxyphthalonitrile [12] were obtained as described elsewhere.

2.1.2. Spectroscopy

The ¹H-, ¹³C- and ²⁹Si-NMR spectra were recorded in CDCl₃ solutions with a Bruker AC 200 or a Bruker DRX 500 spectrometers. IR spectra were obtained with an ATI Mattson spectrometer for polymer solutions in sodium dried toluene.

2.1.3. Molecular weight measurement

Molecular weights were determined by gel-permeation chromatography (GPC) using a Waters system with Wyatt/Optilab 902 Interferometric Refractometer, calibrated for monodisperse polystyrene standards.

2.1.4. Thermo-optical analysis (TOA)

Changes of the transmission of polarized light in a function of temperature were recorded and visualized using a home made program. Simultaneously the morphology of thin layers was observed under optical microscope. Morphology of samples was studied using Nikon Eclipse E400 Pol microscope equipped with polarizing filters and an analog SANYO VCC-3770P camera. The images were acquired using Leadtek TV Tuner WinFast PVR2. Heating and cooling of the samples at a controlled rate was accomplished using Mettler FP82 hot stage equipped with an FP90 controller and a photo detector.

2.1.5. Differential scanning calorimetry (DSC)

Differential scanning calorimetry (DSC) studies were performed using TA Instruments DSC-2920 and DuPont DSC-910, calibrated with an indium standard.

2.1.6. Atomic Force Microscopy (AFM)

Atomic force microscopy (AFM) images were recorded under ambient atmosphere, at room temperature, using Nanoscope IIIa, MultiMode (Veeco, Santa Barbara, CA) microscope. The probes were commercially available rectangular silicon cantilevers (RTESP from Veeco) with nominal radius of curvature in the 10 nm range spring constant 20–80 N/m, a resonance frequency lying in the 264–369 kHz. The images were recorded with the highest available sampling resolution, that is, 512 × 512 data points.

2.1.7. Small angle X-ray scattering (SAXS)

For small angle X-ray scattering (SAXS) 0.5 m long Kiessig-type camera equipped with a pinhole collimator and a Kodak imaging plate as recording medium was used. The camera was coupled to the Philips PW 1830 X-ray generator (Cu K_α operating at 50 kV and 30 mA) consisting of a capillary collimator. Exposed imaging plates were read with PhosphorImager Si system (Molecular Dynamics). Thin layer of **Polymer 1** was deposited on a kapton foil.

2.2. Syntheses

4,5-Bis-octyloxy-phthalonitrile (*sub. 1*)

A mixture of 1.95 g (14.1 mmol) of K₂CO₃, 1.87 g (11.68 mmol) 4,5-dihydroxyphthalonitrile and 4.6 g (23.81 mmol) of 1-bromooctane in 80 ml of dry DMF was refluxed under argon for 7 hrs. After cooling to r.t. 150 ml of water and 150 ml of methylene chloride were added and the mixture was stirred for 30 min. The aqueous (top) layer was extracted with 100 ml of methylene chloride. Combined organic layers were washed with 50 ml of 5% NaHCO₃ aq. twice, and dried over MgSO₄ overnight. The mixture was filtered, and the solvent was evaporated. Brown residue was purified on silica column (eluent: chloroform/ethyl acetate) and dried in vacuum (60°, 1 mmHg, 3 hrs) leaving 3.15 g (yield: 70.1%) of white solid. M.p: 107°C, ¹H NMR (200 MHz, CDCl₃, δ): 0.88 (t, 6H, CH₃), 1.20–1.50 (m, 24 H, C–CH₂–C), 4.0 (t, 4H, CH₂–O), 7.24 (m, 2H, Ph-H), ¹³C NMR (200 MHz, standard proton decoupling, CDCl₃, δ): 14.1 (CH₃), 23.1, 26.2, 31.9, 29.3, 29.5, 26.4, 31.6, (–(CH₂)_x–CH₃), 69.8 (O–CH₂), 117.9 (aromatic carbons), anal. calcd for C₂₄H₃₆N₂O₂: C 74.96, H 9.44 N 7.28; found: C 75.2, H 9.2, N 7.3

4-Methoxy-5-pent-4-enyloxy-phthalonitrile (sub. 2)

The synthesis and purification were performed using the procedure described for 4,5-bis-octyloxy-phthalonitrile. A mixture of 3 g (17.22 mol) of 4-hydroxy-5-methoxy-phthalonitrile, 2.67 g (17.43 mmol) of 5-bromo-pent-1-ene and 2.87 g of K_2CO_3 in 150 ml of DMF after 7 hrs. of refluxing and purification yielded 3.21 g (77%) of white solid. M.p: 131°C, 1H NMR (200 MHz, $CDCl_3$ δ): 1.32 (m, 2H, O–C–CH₂), 1.98 (m, 2H, O–C–C–CH₂), 3.95 (s, 3H, CH₃), 4.07 (t, 2H, O–CH₂), 4.95–5.15 (m, 2H, HC=CH₂), 5.70–5.90 (m, 1H, HC=CH₂), 7.11, 7.26 (m, 2H, Ph-H), ^{13}C NMR (200 MHz, standard proton decoupling, $CDCl_3$, δ): 29.5 (CH₂–CH=CH₂), 31.1 (CH₂–CH₂–CH=CH₂), 56.1 (OCH₃), 69.2 (O–CH₂), 115.4 (CH=CH₂), 117.6, 118.2 (aromatic carbons), 137.8 (CH=CH₂), Anal. calcd for C₁₅H₁₆N₂O₂: C 70.29, H 6.29, N 10.93; found: C 69.9, H 6.1, N 11.1

2-(pent-4-enyloxy)-3-methyloxy-9,10,16,17,23,24-hexakis(octenyloxy)phthalocyanine (sub. 3)

A mixture of 7.9 g (20.5 mmol) of 4,5-bis-octyloxy-phthalonitrile, 1.65 g (6.8 mmol) of 4-methoxy-5-pent-4-enyloxy-phthalonitrile and 3.28 g of DBN in 70 ml of dry ethanol was refluxed for 36 hrs. After cooling down the mixture was diluted with 20 ml of chloroform. 300 ml of acetone was added and the mixture was stirred at r.t. for 30 min. The green precipitate was filtered, washed with acetone, dried and isolated on silica column (eluent: chloroform/methylene chloride). Yield: 1.3 g (13.7%). 1H NMR: (200 MHz, $CDCl_3$ δ): 0.88 (t, 18H, C–CH₃), 1.21–1.71 (m, 36H, –C–CH₂–C from octenyloxy side chains), 1.85–1.91 (m, 10H, –C–CH₂–C–O), 2.02 (m, C–CH₂–C=C), 3.35 (s, 3H, OCH₃), 3.95–4.12 (m, 14H, O–CH₂), 4.90–5.05 (m, 2H, HC=CH₂), 5.65–5.75 (m, 1H, HC=CH₂), 7.31–7.36 (8H, Phalocy-H), ^{13}C NMR (200 MHz, standard proton decoupling, $CDCl_3$, δ): 14.1 (CH₃–(CH₂)₇), 22.7, 26.9, 29.3, 29.8, 30.4, 31.8, (CH₃–(CH₂)₆–CH₂), 28.8, 30.4 (H₂C=CH–(CH₂)₂), 55.8 (OCH₃), 69.2 (H₂C=CH–(CH₂)₂–CH₂O), 69.5 (CH₃–(CH₂)₆–CH₂O), 95.3, 95.5, 102.7, 105.5, 106.9 (aromatic carbons), 115.4 (H₂C=CH), 138.7 (H₂C=CH), anal. calcd for C₈₆H₁₂₂N₈O₈: C 74.00 H 8.81 N 8.03; found: C 74, H 8.7, N 7.9

Hydrosilylation of 2-(pent-4-enyloxy)-3-methyloxy-9,10,16,17,23,24-hexakis(octenyloxy)phthalocyanine with polymethylhydrosiloxane (Polymer 1)

1 g (0.69 mmol) of 2-(pent-4-enyloxy)-3-methyloxy-9,10,16,17,23,24-hexakis(octenyloxy)phthalocyanine and 37 mg (0.62 mmol of [CH₃Si(H)O–]mers) of polymethylhydrosiloxane were dissolved in 15 ml of dry toluene and stirred under argon. Platinum tetramethyldivinylidissiloxane (PTDD) complex in xylenes (10^{-4} mol Pt/mol SiH) was added and the reaction mixture was stirred at 60°C. Reaction progress was followed by FTIR (disappearance of Si-H absorption band at 2150 cm^{-1}). After 24 hrs. of reaction the conversion was 94.4%. The reaction was stopped after 48 hrs, as there was no further progress after that time. Solvent was removed on vacuum, leaving green solid. The product was purified by multiple precipitation from dichloromethane/methanol and dried (75°C, 1 mmHg). Yield 0.75 g (72%). The structure was confirmed by 1H NMR, (Figure 1), ^{13}C NMR (200 MHz, standard proton decoupling, $CDCl_3$, δ): –0.18 (CH₃Si), 1.09 (SiCH₂), 14.11 (CH₃–(CH₂)₇), 18.23 (SiCH₂CH₂), 19.82 (SiCH₂CH₂CH₂), 22.68, 26.90, 29.28, 30.06, 30.42, 31.80 (CH₃–(CH₂)₆–CH₂), 27.14 (SiCH₂CH₂CH₂CH₂), 55.83 (OCH₃), 69.5 (Si–(CH₂)₄CH₂O), 77.24 (CH₃–(CH₂)₆–CH₂O), 95.17, 102.97, 105.29, 106.97 (aromatic carbons) and ^{29}Si NMR: (500 MHz, INEPT, $CDCl_3$ δ): –6 (–[Si(Me)(R)O]_n–), M_n = 6350, M_w = 9400 (GPC)

3. Results and discussion**3.1. Synthesis**

From synthetic point of view the most difficult step is obtaining phthalocyanines with a single terminal alkenyloxy substituent, which can be later attached to polysiloxanes as a side chain via hydrosilylation reaction (Figure 2).

The synthetic pathway to obtain phthalocyanines with various substituents was based on J. F. van der Pol paper from 1989 [14]. Unfortunately, all the starting aromatic nitriles are not available commercially and their synthesis is a multi-step process. The subsequent step of the synthesis was a coupling reaction (Figure 3) of the 3:1 mixture of bis-octenyloxy- and methoxy-5-pent-4-enyloxy substituted nitriles leading to a mixture of various phthalocya-

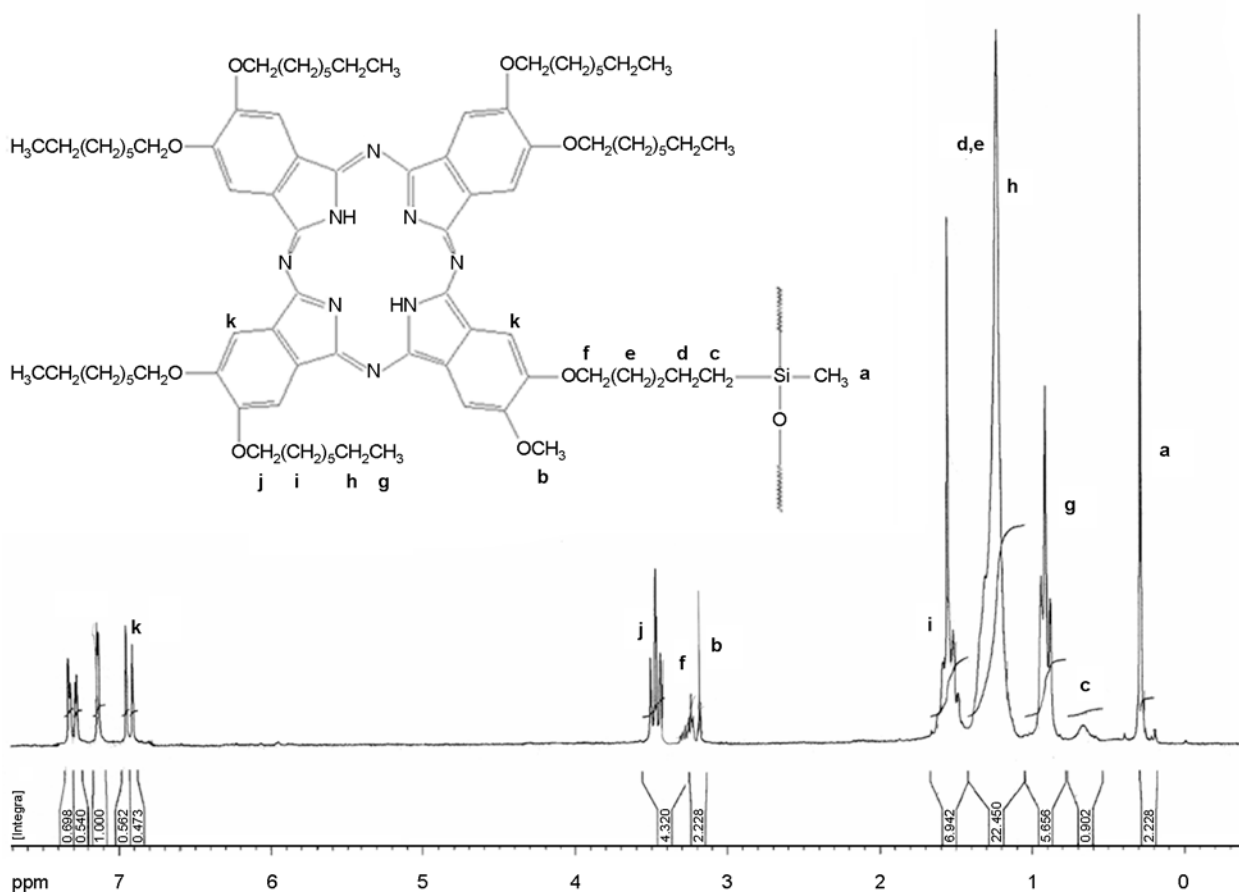


Figure 1. ¹H NMR (a) of Polymer 1

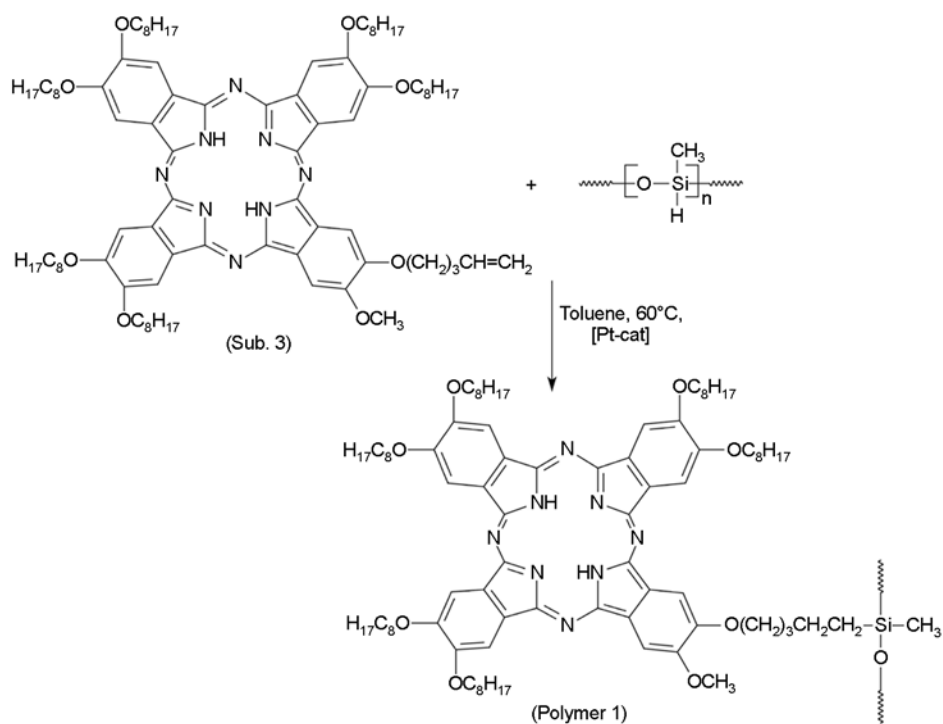


Figure 2. Synthetic pathway of side chain phthalocyanine substituted polysiloxane

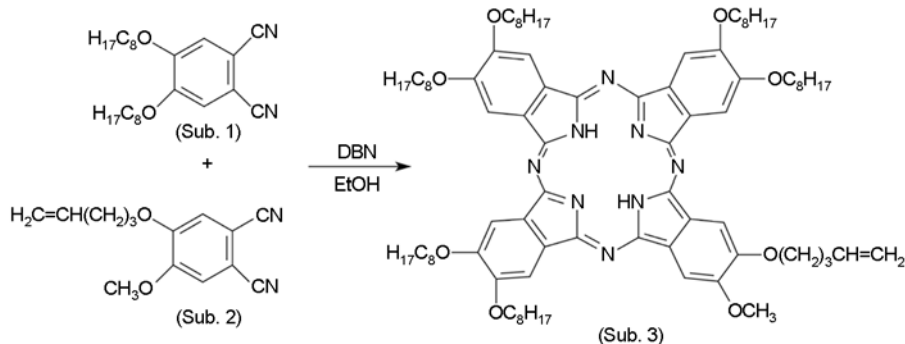


Figure 3. Synthetic route to of asymmetrically substituted phthalocyanines

nine products, which then had to be separated by column chromatography. The separation process was probably the main reason for low yields (11–13%) of the expected products. They were, however, close to that reported by van der Pol *et al.* [14] for analogous compounds.

The attachment of the side phthalocyanine groups to the polysiloxane were performed in typical hydrosilylation conditions (toluene, Karstedt's catalyst, 60–80°C). The conversion (94–95%) after 24 hrs (as proved by the disappearance of Si–H signal at 2150 cm^{-1} in FTIR) was in rather typical range for hydrosilylation of alkenes bearing bulky groups [15]. As a result of the size of phthalocyanines higher level of the addition could not be obtained even after extended time of reaction (48 hrs). Although the final product contained ~5% of the unreacted Si–H moieties, they were hydrolytically stable and we did not observe any crosslinking due to Si–H hydrolysis and condensation of silanol groups even if the samples were heated up to 150°C or washed with water.

3.2. Phase behaviour studies

DSC measurements of **Polymer 1**, at a heating rate of 5°C/min (curve 1 in Figure 4), revealed the endothermic phase transition at 70.8°C (enthalpy of 106.8 J/g). The transition corresponds to melting as confirmed by subsequent temperature optical analysis (TOA).

Upon cooling at rate of 5°C/min (curve 2 in Figure 4), the exothermic peak (enthalpy of 95 J/g) corresponding to transition from isotropic liquid to organized structure was observed after large supercooling, at the temperature of 32.7°C.

Polysiloxane used in the synthesis is amorphous, therefore the phase transition at 32.7°C must be

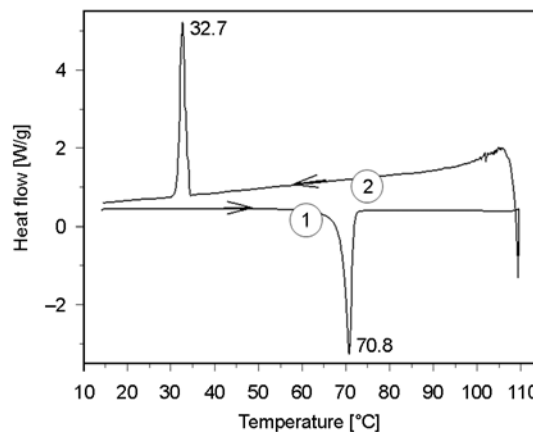


Figure 4. DSC thermogram of **Polymer 1**: curve 1 – heating; curve 2 – cooling

related to self-organization of phthalocyanine side groups. The result implies that the attachment of Pc *via* flexible spacer to the flexible polysiloxane does not preclude self-assembling of phthalocyanine discs.

It is worth noting that the enthalpy of the phase transitions at 70.8 and 32.7°C is much higher than usually observed for transitions of alkylated phthalocyanines from liquid crystalline state to isotropic melt and reverse [14, 16, 17]. It suggests the crystalline (not liquid crystalline) nature of **Polymer 1**. The phase transitions of **Polymer 1** was independently studied by means of thermo-optical analysis (TOA). Changes of the transmission of polarized light in function of temperature were recorded. Simultaneously the morphology of thin layers was observed under optical microscope. The layer of free, starting phthalocyanine compound (**sub. 3**) was also investigated for comparison.

The changes of the light intensity transmitted through layers of free phthalocyanine compound (**sub. 3**) and **Polymer 1** upon heating at a rate of 5°C/min and cooling at a rate of 5°C/min (and of

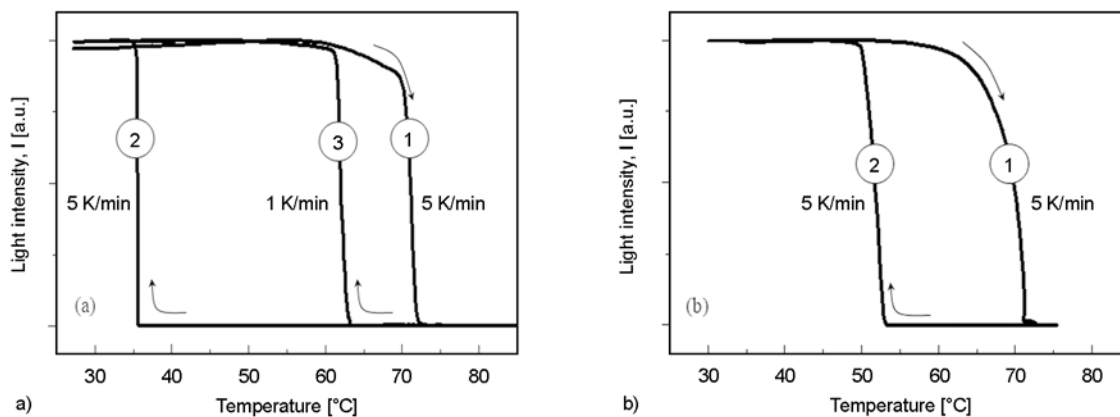


Figure 5. TOA curves for **sub. 3**. (a) and **Polymer 1** (b). Heating and cooling rates are indicated.



Figure 6. Room temperature morphology of thin **sub. 3** and **Polymer 1** layers (seen under crossed polarizes) after different thermal history: (a) – **sub. 3**, cooling rate of 5 K/min; (b) – **Polymer 1**, cooling rate of 5 K/min and (c) – **Polymer 1** cooling rate of 1 K/min

1°C/min) are shown in Figure 5). Images of samples showing morphology at room temperature (after cooling) are shown in Figure 6.

As one can see, upon heating of **Polymer 1** at the rate 5°C/min (curve 1 in Figure 5a) the intensity of the transmitted light starts to decrease slowly at 60°C. A fast decrease is observed at ca 70°C when the melting temperature is reached.

Similar behavior (upon heating at a rate of 5°C/min) was observed for free phthalocyanine compound **sub. 3** (compare curves 1 in Figure 5a and 5b).

It is worth noting that the melting temperatures for **sub. 3** and **Polymer 1** are practically identical. The results imply that the attachment of **sub. 3** to a flexible polysiloxane chain does not affect the melting temperature of self-assembled phthalocyanine discs.

The difference between the two systems appears during cooling.

In the case of free phthalocyanine compound (**sub. 3**), upon cooling at the rate of 5°C/min, the light transmittance rises rapidly below 53°C (curve 2 in Figure 5). It is correlated with the growth of dendritic, highly birefringent structures (Figure 6a). Their growth is completed at ca. 49°C.

Nucleation and growth of dendritic structures of **Polymer 1** during cooling (at the same rate of 5°C/min) occurs at higher supercooling as compared with free **sub. 3** (compare curves 2 in Figure 5a and 5b). The growth of dendritic structures of **Polymer 1** starts at much lower temperature of

36°C. The branches forming dendrites are much thinner as compared with dendrites of free **sub. 3**. This can be explained by their faster growth at higher supercooling under more diffusion limited conditions (compare Figure 6a and 6b). One can conclude that the attachment of **sub. 3** to polysiloxane chain does not preclude the self-organization of discs, however it makes it more difficult (slower).

The temperature when self-assembling of **Polymer 1** starts as well as the resulting morphology is strongly dependent on a cooling rate.

Upon cooling at lower rate of 1°C/min the supercooling of ca. 10°C is relatively small as compared with ca. 35°C for the cooling rate of 5°C/min (com-

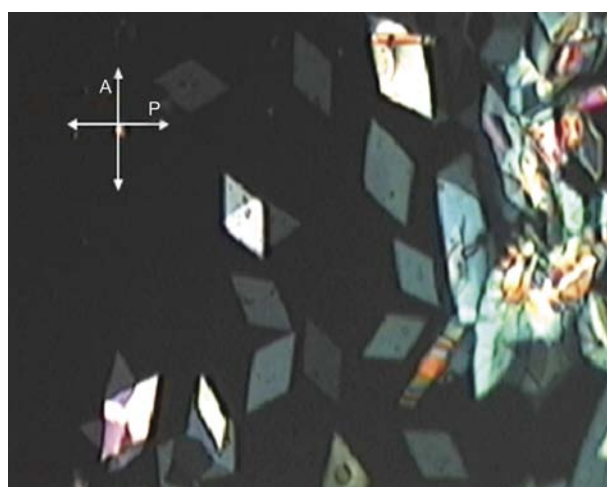
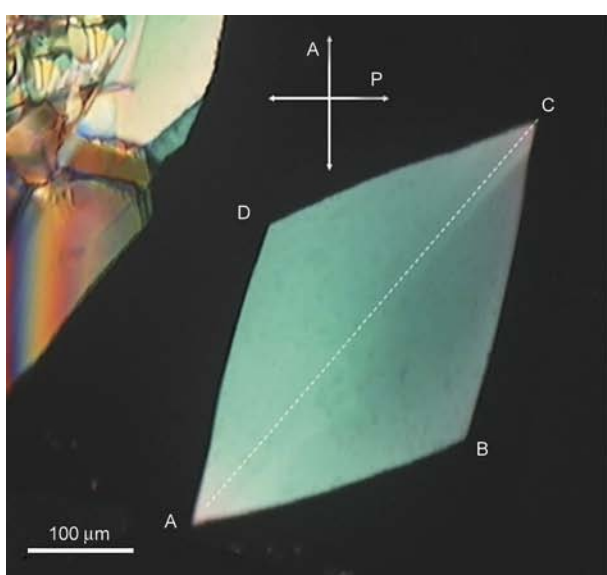
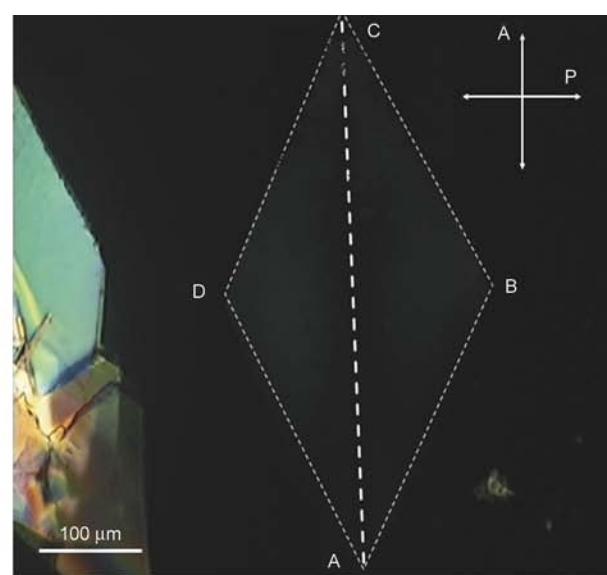


Figure 7. Rhomboidal plates of **Polymer 1** growing isothermally at 69°C viewed under cross-polarization. The growing plates are embedded in melted **Polymer 1** seen as a black medium.



a)



b)

Figure 8. The same rhomboidal plate of **Polymer 1** seen between crossed polarizers at different orientation: (a) 45° and (b) parallel to the polarizer

pare curves 2 and 3 in Figure 5). The growth of more equilibrium (but still highly branched) leaf-like structures (Figure 6c) is observed in the temperature range of 60–63°C

Under isothermal conditions, at small supercooling, at the temperature of 69°C, the growth of rhomboidal plates of **Polymer 1** is observed (Figure 7). Such rhomboidal shape is uncommon for liquid crystalline materials. The shape together with the mentioned earlier high enthalpy of the phase transition and relatively large supercooling suggest the crystalline nature of the **Polymer 1**.

The plates are highly birefringent. As one can see in Figure 7 the light intensity transmitted by the plates under crossed polarizers strongly depends on their orientation.

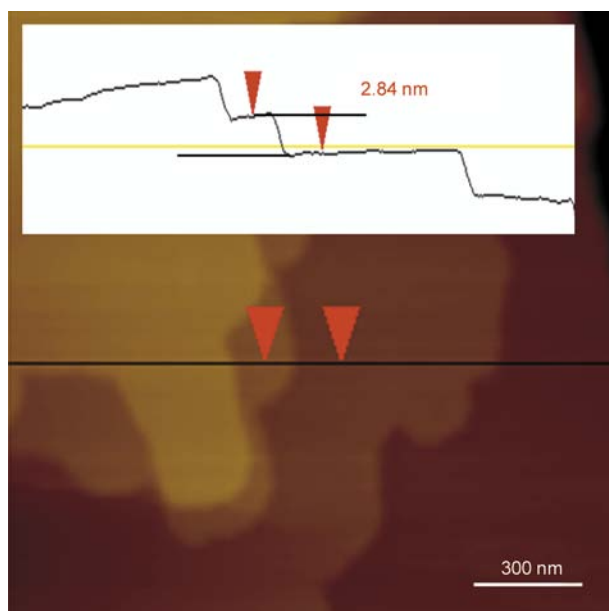


Figure 9. AFM image of the surface of **Polymer 1** plate

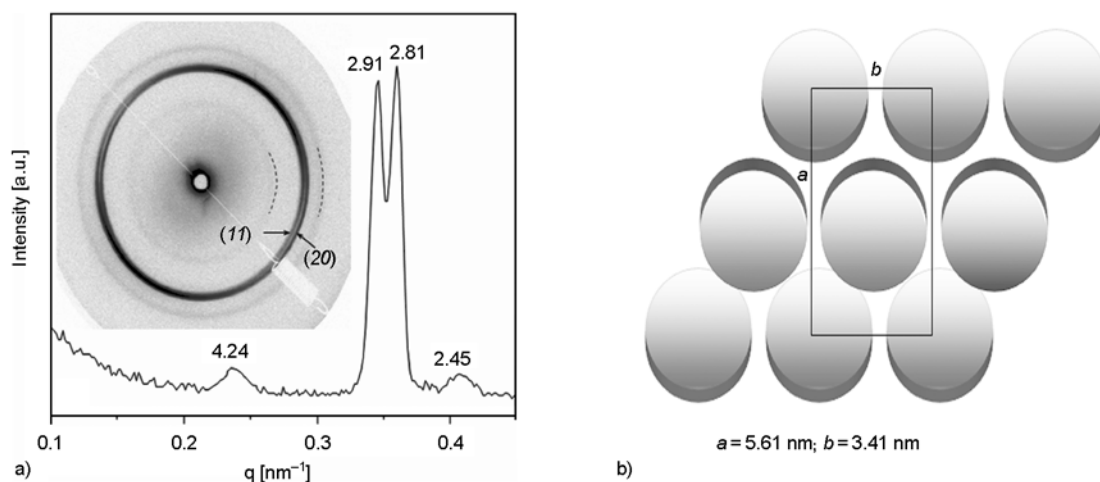


Figure 10. (a) – small X-ray diffraction pattern of layer of **Polymer 1** deposited on kapton foil. (b) – proposed unit cell viewed along c-axis.

Images of the same rhomboidal crystalline plate ‘ABCD’ differently oriented with respect to polarized light are shown in Figure 8. The transmitted light intensity is the highest when the plate is oriented its diagonal AC at an angle of 45° with respect to polarizer (Figure 8a). No sectors are then visible, which means that phthalocyanine discs are uniformly organized within the plate (unique optical axis).

The plate is hardly seen when its diagonal is parallel to the polarizer (Figure 8b). It means that the optical axis is oriented parallelly or perpendicularly to the diagonal AC.

One can expect that phthalocyanine discs, even attached as side groups to polymer chain *via* flexible spacer, form columns [14]. The result shown in Figure 8 implies that columns are uniformly oriented parallelly or perpendicularly to diagonal of the plate.

Despite our experience in imaging columns of discotic materials [18, 19] using AFM, we could not visualize columnar structure in the case of **Polymer 1**. We could however reveal the layer-like structure of the rhomboidal plates. The thickness of layers of ca. 2.9 nm was determined (Figure 9).

Thickness of ca. 2.9 nm (corresponding to the thickness of a single sheet of columns) is in a reasonable agreement with earlier measurements performed on layers of other similar phthalocyanines forming columns [19–22].

Postulated columnar structure of **Polymer 1** was confirmed by preliminary X-ray diffraction studies. The result of small angle X-ray diffraction of thin layer of **Polymer 1** at room temperature is shown in

Figure 10a. The diffraction pattern is dominated by two peaks corresponding to periodicities of 2.91 and 2.81 nm. These peaks can tentatively be ascribed to reflections from (11) and (20) planes assuming rectangular unit cell parameters $a = 5.61$ nm and $b = 3.41$ nm (Figure 10b).

One can also see two much weaker peaks corresponding to distances of 4.25 and 2.45 nm. They can be assigned to hexagonal phase since $4.25 \approx \sqrt{3} \cdot 2.45$.

There is, probably, a small amount of polymeric phthalocyanine which contains some defects which does not allow formation of crystalline phase.

Unambiguous classification of the unit cell and orientation of columns forming awaits completion by further X-ray studies.

4. Conclusions

The synthetic pathway of which the most difficult step was preparation of phthalocyanine bearing single terminal alkenyloxy groups has been proven successful. According to our best knowledge it is the very first synthesis of polysiloxanes bearing side phthalocyanine moieties ever published.

Transition temperatures determined by TOA correspond to those determined by DSC. Therefore TOA can be considered as a very efficient and complementary tool for studies of phase transition of some discotic systems. Moreover smaller amount of the material (layers of thickness smaller than 1 μm can be investigated) is required for TOA experiments.

Attachment of phthalocyanine to polysiloxane chain via flexible spacer does not preclude formation of columnar organization. The spacer effectively decouples the motions of the phthalocyanine groups from the main chain. Thus the columnar ordering of the side groups is possible.

The attachment of phthalocyanine derivatives to polymer chain slows down the kinetics of self-organization (crystallization) in comparison with corresponding free phthalocyanine.

Acknowledgements

Scientific work financed by the Polish government's budget for science in the years 2010–2013. Grant of the Ministry of Science and Higher Education No 5155/B/T02/2010/39

References

- [1] Law K. Y.: Organic photoconductive materials: Recent trends and developments. *Chemical Reviews*, **93**, 449–486 (1993). DOI: [10.1021/cr00017a020](https://doi.org/10.1021/cr00017a020)
- [2] Emmelius M., Pawlowski G., Vollmann H. W.: Materials for optical data storage. *Angewandte Chemie International Edition in English*, **28**, 1445–1471 (1989). DOI: [10.1002/anie.198914453](https://doi.org/10.1002/anie.198914453)
- [3] Deng H., Mao H., Lu Z., Xu H.: Influence of molecular aggregation and orientation on the photoelectric properties of tetrasulfonated gallium phthalocyanine self-assembled on a microporous TiO_2 electrode. *Thin Solid Films*, **315**, 244–250 (1998). DOI: [10.1016/S0040-6090\(97\)00753-0](https://doi.org/10.1016/S0040-6090(97)00753-0)
- [4] Mortimer R. J.: Organic electrochromic materials. *Electrochimica Acta*, **44**, 2971–2981 (1999). DOI: [10.1016/S0013-4686\(99\)00046-8](https://doi.org/10.1016/S0013-4686(99)00046-8)
- [5] Li L., Tang Q., Li H., Hu W., Yang X., Shuai Z., Liu Y., Zhu D.: Organic thin-film transistors of phthalocyanines. *Pure and Applied Chemistry*, **80**, 2231–2240 (2008). DOI: [10.1351/pac200880112231](https://doi.org/10.1351/pac200880112231)
- [6] Wisnieff R.: Display technology: Printing screens. *Nature*, **394**, 225–227 (1998). DOI: [10.1038/28278](https://doi.org/10.1038/28278)
- [7] Crone B. K., Dodabalapur A., Sarpeshkar R., Gelperin A., Katz H. E., Bao Z.: Organic oscillator and adaptive amplifier circuits for chemical vapor sensing. *Journal of Applied Physics*, **91**, 10140–10146 (2002). DOI: [10.1063/1.1476084](https://doi.org/10.1063/1.1476084)
- [8] Bouvet M.: Phthalocyanine-based field-effect transistors as gas sensors. *Analytical and Bioanalytical Chemistry*, **384**, 366–373 (2006). DOI: [10.1007/s00216-005-3257-6](https://doi.org/10.1007/s00216-005-3257-6)
- [9] McKeown N. B.: Phthalocyanine-containing polymers. *Journal of Materials Chemistry*, **10**, 1979–1995 (2000). DOI: [10.1039/b000793p](https://doi.org/10.1039/b000793p)
- [10] Ganicz T., Stańczyk W.: Side-chain liquid crystal polymers (SCLCP): Methods and materials. An overview. *Materials*, **2**, 95–128 (2009). DOI: [10.3390/ma2010095](https://doi.org/10.3390/ma2010095)
- [11] Armarego W. L. F., Chai C. L. L.: Purification of laboratory chemicals. Elsevier, Amsterdam (2003).
- [12] Baugh S. D. P., Yang Z., Leung D. K., Wilson D. M., Breslow R.: Cyclodextrin dimers as cleavable carriers of photodynamic sensitizers. *Journal of the American Chemical Society*, **123**, 12488–12494 (2001). DOI: [10.1021/Ja011709o](https://doi.org/10.1021/Ja011709o)
- [13] Van der Pol J. F., Neeleman E., Zwikker J. W., Drenth W., Nolte R. J. M.: Evidence of an ordered columnar mesophase in peripherally octa-*n*-alkoxy-substituted phthalocyanines. *Recueil des Travaux Chimiques des Pays-Bas*, **107**, 615–620 (1988). DOI: [10.1002/recl.19881071102](https://doi.org/10.1002/recl.19881071102)

- [14] Van der Pol J. F., Neeleman E., Nolte R. J. M., Zwikker J. W., Drenth W.: Asymmetrically substituted liquid-crystalline phthalocyanines and side-chain polymers derived from them. *Die Makromolekulare Chemie*, **190**, 2727–2745 (1989).
DOI: [10.1002/macp.1989.021901107](https://doi.org/10.1002/macp.1989.021901107)
- [15] Marciniak B.: *Comprehensive handbook on hydrosilylation*. Pergamon Press, Oxford (1992).
- [16] Geerts Y. H., Debever O., Amato C., Sergeev S.: Synthesis of mesogenic phthalocyanine-C₆₀ donor-acceptor dyads designed for molecular heterojunction photovoltaic devices. *Beilstein Journal of Organic Chemistry*, **5**, 49/1–49/9 (2009).
DOI: [10.3762/Bjoc.5.49](https://doi.org/10.3762/Bjoc.5.49)
- [17] Sergeev S., Pouzet E., Debever O., Levin J., Gierschner J., Cornil J., Aspe R. G., Geerts Y. H.: Liquid crystalline octaalkoxycarbonyl phthalocyanines: Design, synthesis, electronic structure, self-aggregation and mesomorphism. *Journal of Materials Chemistry*, **17**, 1777–1784 (2007).
DOI: [10.1039/B617856a](https://doi.org/10.1039/B617856a)
- [18] Breiby D. W., Bunk O., Pisula W., Sølling T. I., Tracz A., Pakula T., Müllen K., Nielsen M. M.: Structure of zone-cast HBC-C₁₂H₂₅ films. *Journal of the American Chemical Society*, **127**, 11288–11293 (2005).
DOI: [10.1021/Ja042355e](https://doi.org/10.1021/Ja042355e)
- [19] Tracz A., Makowski T., Masirek S., Pisula W., Geerts Y. H.: Macroscopically aligned films of discotic phthalocyanine by zone casting. *Nanotechnology*, **18**, 485303/1–485303/5 (2007).
DOI: [10.1088/0957-4484/18/48/485303](https://doi.org/10.1088/0957-4484/18/48/485303)
- [20] Anokhin D. V., Rosenthal M., Makowski T., Tracz A., Bras W., Kvashnina K., Ivanov D. A.: Comparative structural study of thin films of a columnar liquid crystal aligned by mechanical shearing and zone casting. *Thin Solid Films*, **517**, 982–985 (2008).
DOI: [10.1016/j.tsf.2008.07.012](https://doi.org/10.1016/j.tsf.2008.07.012)
- [21] Tant J., Geerts Y. H., Lehmann M., De Cupere V., Zucchi G., Laursen B. W., Bjørnholm T., Lemaure V., Marcq V., Burquel A., Hennebicq E., Gardebien F., Viville P., Beljonne D., Lazzaroni R., Cornil J.: Liquid crystalline metal-free phthalocyanines designed for charge and exciton transport. *The Journal of Physical Chemistry B*, **109**, 20315–20323 (2005).
DOI: [10.1021/Jp054778o](https://doi.org/10.1021/Jp054778o)
- [22] Tant J., Geerts Y. H., Lehmann M., De Cupere V., Zucchi G., Laursen B. W., Bjørnholm T., Lemaure V., Marcq V., Burquel A., Hennebicq E., Gardebien F., Viville P., Beljonne D., Lazzaroni R., Cornil J.: Liquid crystalline metal-free phthalocyanines designed for charge and exciton transport (Correction). *The Journal of Physical Chemistry B*, **110**, 3449 (2006).
DOI: [10.1021/Jp060109e](https://doi.org/10.1021/Jp060109e)

Hydrogels based on chemically modified poly(vinyl alcohol) (PVA-GMA) and PVA-GMA/chondroitin sulfate: Preparation and characterization

E. G. Crispim¹, J. F. Piai¹, A. R. Fajardo¹, E. R. F. Ramos², T. U. Nakamura², C. V. Nakamura², A. F. Rubira¹, E. C. Muniz^{1*}

¹Grupo de Materiais Poliméricos e Compósitos (GMPC), Departamento de Química, Universidade Estadual de Maringá (UEM) – Av. Colombo 5790; CEP 87020-900 – Maringá, Paraná, Brazil

²Laboratório de Microbiologia Aplicada aos Produtos Naturais e Sintéticos, Departamento de Análises Clínicas, Universidade Estadual de Maringá (UEM) – Av. Colombo 5790; CEP 87020-900 – Maringá, Paraná, Brazil

Received 10 September 2011; accepted in revised form 30 November 2011

Abstract. This work reports the preparation of hydrogels based on PVA-GMA, PVA-GMA is poly(vinyl alcohol) (PVA) functionalized with vinyl groups from glycidyl methacrylate (GMA), and on PVA-GMA with different content of chondroitin sulfate (CS). The degrees of swelling of PVA-GMA and PVA-GMA/CS hydrogels were evaluated in distilled water and the swelling kinetics was performed in simulated gastric and intestinal fluids (SGF and SIF). PVA-GMA and PVA-GMA/CS hydrogels demonstrated to be resistant on SGF and SIF fluids. The elastic modulus, E , of swollen-hydrogels were determined through compressive tests and, according to the obtained results, the hydrogels presented good mechanical properties. At last, the presence of CS enhances the hydrogel cell compatibility as gathered by cytotoxicity assays. It was concluded that the hydrogels prepared through this work presented characteristics that allow them to be used as biomaterial, as a carrier in drug delivery system or to act as scaffolds in tissue engineering as well.

Keywords: polymer gels, poly(vinyl alcohol), chondroitin sulfate, hydrogels, drug delivery

1. Introduction

By the most used definition, hydrogels are polymer networks, which are capable of absorbing and retaining large amounts of water and biological fluids [1, 2]. The physical and chemical features of hydrogels are extremely important for choice of their specific applications. Normally, the behavior of hydrogels depends of external conditions in which such materials are exposed. Thus, it is important to characterize the hydrogel properties in conditions similar to that it will be applied [3].

An often and important characteristic of hydrogels is the biocompatibility. Because of this, hydrogels had been applied in biomedical field. For instance,

as prolonged or controlled drug delivery systems, contact lenses, biosensors, catheters, and tissue engineering and organ reconstruction scaffolds are exceedingly common [4, 5].

Hydrogels can be formed by either chemical or physical cross-linking process or just by entangling of polymer chains. Galactomannan, dextran, alginate, pectin, and chondroitin sulfate are good examples of natural polymers applied on hydrogel formulations. Among the synthetic ones, poly(vinyl alcohol) (or PVA), poly(hydroxyethyl methacrylate) (or polyHEMA), poly(ethylene oxide) (or PEO) and poly(*N*-isopropylacrylamide) (or PNIPAAm) may be cited [6, 7] from a plenty of others.

*Corresponding author, e-mail: ecmuniz@uem.br

By combining synthetic and natural polymers through either interpenetrating (IPN) or semi-interpenetrating (semi-IPN) networks, both the hydrogel physical and biocompatibility properties can be improved [8]. Furthermore, this approach may induce on hydrogel specific properties such as pH- and/or temperature-sensitivity [6].

PVA is a synthetic hydrophilic polymer widely used in various areas, including foods, lacquers, resins and cosmetics industries [9–11]. In the pharmaceutical field, PVA acts as drug coating agent [12] and as material for surgical sutures. This wide applicability of PVA in such fields is due its low toxicity (LD_{50} , 15–20 $g \cdot kg^{-1}$), not showing mutagenic, or clastogenic characteristics [10, 11]. PVA has large oral ingestion, and it is not absorbed by the gastrointestinal tract, enabling its application in the obtainment of drug carriers.

Specifically, PVA-based hydrogels may be prepared by either chemical or physical cross-linking. As a rule, multifunctional moieties capable of reacting with the PVA hydroxyl groups can be used as cross-linking agents for obtaining 3D PVA networks [13]. Although PVA can be easily cross-linked by contact with glutaraldehyde in acidic medium [14] such process presents limitations due to non-uniformity of the obtained matrix and to the severe toxicity of glutaraldehyde. PVA can also be physically cross-linked by repeated freezing-thawing cycles in aqueous solution, creating crystalline clusters that actuate as reticules [15, 16]. The advantage of this process is the absence of moieties that could obliterate the biocompatibility. However, the PVA hydrogels obtained through freezing-thawing process are mechanically poorer and less thermally stable than those obtained by chemical cross-linking [15]. In addition, it is difficult to obtain physical gels *in situ* using this methodology.

PVA and several polysaccharides have been modified with acrylates and methacrylates by different ways [17–20]. The addition of unsaturations to polymers allows the reticulation of modified polymers without the addition of cross-linking agents [21–26]. The reaction may be carried out through the radical initiator pathway or by UV-light [27]. The esterification of part of hydroxyl groups of PVA by reaction with glycidyl methacrylate has been often used in our lab for modifying PVA obtaining PVA-GMA. The cross-linking reaction of PVA-

GMA in presence of CS, which is a mucopolysaccharide present in tissues and ligaments and a key component of cartilage [27], results in a semi-IPN hydrogel type.

In the present work, different 3D PVA-GMA matrices with CS entrapped were prepared aiming to tailor some mechanical properties as compared to respective PVA-GMA matrix. The initial expectance is that the presence of CS enhanced mechanical properties and the cell viability. Therefore, the goals were to prepare hydrogels based on PVA-GMA and semi-IPN hydrogels based on PVA-GMA/CS and to characterize their mechanical properties, water uptake capacity at pH 1.2 and 7.5 buffers solutions and cytotoxicity to potentize their application in biomedical uses.

2. Experimental

2.1. Materials

Poly(vinyl alcohol) (M_w 13–23 $kg \cdot mol^{-1}$, CAS 9003-20-7), *N,N,N',N'*-tetramethylethylenediamine (TEMED, CAS 110-18-9) and sodium persulfate (SP, CAS 7775-27-1) were purchased from Aldrich; Glycidyl methacrylate (GMA, CAS 106-91-2) was purchased from Acros Organics (Belgium). Chondroitin sulfate (CS, CAS 9007-28-7) was kindly supplied by Solabia (Maringá, Brazil). Cell culture medium Dulbecco's Modified Eagle Medium (DMEM, Gibco, Invitrogen Corporation, New York, USA) and trypan blue (Sigma Chemical Co., St. Louis, Missouri, USA) were also used. All the reagents were used as received.

2.2. PVA characterization

PVA molar masses (M_w and M_n) were determined through gel size-exclusion chromatography (SEC) in an Ultra-hydrogel linear column attached to a HPLC Shimadzu apparatus with a refraction index detector. Aqueous solution of $NaNO_3$ (0.1 $mol \cdot L^{-1}$) was used as mobile phase at 0.5 $mL \cdot min^{-1}$ flow rate. Pullulan from Sodex Denko (Japan) was used as standard. The obtained value for M_w was 23.4 $kg \cdot mol^{-1}$ and for M_n was 11.3 $kg \cdot mol^{-1}$; thus, the raw PVA presented a polydispersity ca. 2.07.

The molar mass of CS was obtained by diluted solution-viscometry at 25°C using the Mark-Houwink-Sakurada Equation ($[\eta] = kM^a$) in aqueous solution with ionic strength of 0.2 M. The k and a constants used were equal to $5 \cdot 10^{-6}$ and 1.14,

respectively [28]. The obtained M_v value for CS was $19.9 \text{ kg}\cdot\text{mol}^{-1}$.

2.3. PVA modification

The procedures for chemical modifying of PVA with GMA were adopted according to previously published work [29]. Briefly, the modification of PVA was performed through the insertion of methacryloyl groups from GMA on the PVA chains, utilizing different molar $[-\text{OH}(\text{PVA})/\text{GMA}]$ ratios, at controlled temperature (62°C) during 6 h. The modification reaction was carried out in dimethyl sulfoxide (DMSO) and the obtained material was purified in acetone for removing the GMA not reacted. The reaction of PVA with GMA producing PVA-GMA was confirmed through ^1H NMR spectroscopy (data not shown here). The different degrees of substitution (DS) were calculated from ^1H NMR spectra obtained for the PVA-GMA according to work reported by Crispim *et al.* [29].

2.4. Preparation of PVA-GMA and PVA-GMA/CS hydrogels

Membrane and cylinder forms of PVA-GMA or PVA-GMA/CS hydrogels were prepared using PVA-GMA at different DS (2.5, 3.5 and 5.0%) and requested amounts of CS. The amounts of PVA-GMA and CS applied to form the hydrogels are described in Table 1.

Each hydrogel sample was prepared by mixing of aqueous solutions of PVA-GMA and CS, containing the amounts of PVA-GMA and CS described in Table 1, except for PVA-GMA100 sample. Furthermore, 0.2 mL of $0.57 \text{ mol}\cdot\text{L}^{-1}$ TEMED aqueous solution, as a catalytic agent, was introduced in each sample preparation. The mixtures were deoxygenated by N_2 bubbling for 15 min under stirring. After this, 0.15 mL of aqueous solution of SP ($\text{Na}_2\text{S}_2\text{O}_8$, $0.2 \text{ g}\cdot\text{L}^{-1}$) was added in each mixture under strong stirring, and then each solution was quickly inserted between two acrylic plates sepa-

rated by a 3 mm thick rubber gasket (to obtain membranes) or quickly transferred to 5 and 10 mL syringes (to obtain hydrogels with cylindrical shape). The hydrogels were stored by 24 h at room temperature (ca. 25°C) for complete cross-linking. After, the hydrogels were washed in distilled water several times to remove the not reacted moieties. The procedures to prepare the hydrogels for PVA-GMA with DS equal to 2.5, 3.5, and 5.0% were the same.

2.5. Fourier transformed infrared spectroscopy (FTIR)

The samples PVA-GMA100, PVA-GMA90/CS10 and PVA-GMA67/CS33, with DS equal to 5.0%, and pure CS were characterized by FTIR technique using an equipment (Shimadzu Scientific Instruments, Japan, Model 8300) operating in the region from 4000 to 500 cm^{-1} with resolution of 4 cm^{-1} . Before the spectrum acquisition, each dried sample was blended with KBr powder and pressed into tablets.

2.6. Degree of swelling

The degree of swelling (q) was estimated from the weight ratio (in grams) of the swollen hydrogel sample up to 48 h (at the equilibrium) related to its dry weight (in grams) according to Equation (1):

$$q = \frac{w_i - w_0}{w_0} \quad (1)$$

where w_i is the weight of the swollen hydrogel samples and w_0 is the weight of the dry ones. So, the cylindrical hydrogels samples were deposited in a container with 50 mL of distilled water. After achieved the swelling equilibrium, the hydrogels were collected and maintained in an oven for 48 h, at 40°C . Next, they were transferred to desiccators under reduced pressure for 72 h or until constant weight. The measurements of q were made in triplicate ($n = 3$).

Table 1. Amounts of PVA-GMA and CS applied to prepare the PVA-GMA and PVA-GMA/CS hydrogels, at a fixed DS

Hydrogel	Amounts		Mass ratio	Total Mass
	PVA-GMA [g]	CS [g]	PVA-GMA:CS [%]	PVA-GMA + CS [g]
PVA-GMA100	2.50	0.000	100:0	2.500
PVA-GMA90/CS10	2.50	0.278	90:10	2.778
PVA-GMA80/CS20	2.50	0.625	80:20	3.125
PVA-GMA67/CS33	2.50	1.250	67:33	3.750

2.7. Determination of swelling kinetics in simulated gastric fluid (SGF) and simulated intestinal fluid (SIF)

The hydrogel swelling kinetics was investigated in SGF (pH 1.2±0.1) and SIF (pH 7.5±0.1). SGF and SIF were prepared according to the United States Pharmacopeia (USP) [30], except the use of enzymes. For these tests, cylindrical hydrogels with approximately 15 cm diameter and 15 mm thickness were dried under reduced pressure until constant weight. Each sample was dipped in 50 mL of either SGF or SIF at 37°C. So, each sample was weighed from 5 min after immersion in the desired time span up to constant weight. Swelling kinetics was evaluated using the Equation (2) [31]:

$$\frac{M_t}{M_\infty} = kt^n \quad (2)$$

where M_t and M_∞ are the fluid mass absorbed by the hydrogel up to time t and at equilibrium, respectively. The values of k and n for each run were determined from the coefficients (linear and slope, respectively) of the curve $\ln(M_t/M_\infty)$ versus $\ln t$.

2.8. Compressive measurements

Compressive tests were performed in hydrogels membranes using a texture analyzer (TA.TXT2 Stable Micro System, Haslemere, Surrey, UK) equipped with a 5 kg load cell. The maximum sample deformation was fixed at 1.0 mm. Compressive tests were carried out by moving down a cylindrical probe with 12.7 mm diameter at 0.2 mm·s⁻¹. The test (sample adjustment and compression) must be performed in less than 50 s for avoiding water loss by the hydrogel during the experiment. Prior to the tests, the hydrogel-membranes (30 mm × 50 mm and thickness ≈ 3 mm) were immersed in distilled water for 48 h at 25°C. The compressive tests using the swollen samples were carried out at 25°C. For each sample, duplicate ($n = 2$) were performed and average value was calculated. The data generated by the equipment are force (F) and strain (ΔL). Stress (σ) was obtained through Equation (3):

$$\sigma = \frac{F}{A} \quad (3)$$

where A is the cross-sectional area of the probe. The value of the compressive modulus (E) of each hydrogel was calculated through Equation (4):

$$E = \frac{\sigma}{\alpha - \alpha^{-2}} = RT\nu_e \left(\frac{\varphi_{2,r}}{\varphi_{2,s}} \right)^{2/3} \varphi_{2,s} \quad (4)$$

from the initial linear portion of the curves of σ versus $(\alpha - \alpha^{-2})$, where α is the de ratio of strain given by $\alpha = (L_0 + \Delta L)/L_0 < 1.10$, being L_0 the sample initial thickness.

The values of cross-linking density, ν_e , and the molar mass between two consecutive cross-links, M_c , of PVA-GMA hydrogels without CS (or PVA-GMA100) were calculated from the G modulus using Equations (5) and (6):

$$\nu_e = \frac{G}{RT \left(\frac{\varphi_{2,r}}{\varphi_{2,s}} \right)^{2/3} \varphi_{2,s}} \quad (5)$$

$$M_c = \frac{\rho_2}{\nu_e + \frac{2\rho_2}{M_n}} \quad (6)$$

where $G = 3/E$ [32], ρ_2 and M_n are the density and molecular mass of the polymer, respectively. The parameters $\varphi_{2,s}$ and $\varphi_{2,r}$ calculated with the respective Equations (7) and (8):

$$\varphi_{2,s} = \frac{V_0}{V_s} = \frac{\frac{W_0}{\rho_0}}{\frac{W_0}{\rho_0} + \frac{W_s - W_0}{\rho_{H_2O}}} \quad (7)$$

$$\varphi_{2,r} = \frac{V_0}{V_r} = \frac{\frac{W_0}{\rho_0}}{\frac{W_0}{\rho_0} + \frac{W_r - W_0}{\rho_{H_2O}}} \quad (8)$$

where V and W are volume and mass, respectively, and subscripts 0, s , and r mean dry, equilibrium-swelling, and relaxed (just after polymerization) states of hydrogel. The density of the dry hydrogel, ρ_0 , was considered as being the density of atactic PVA, 1.269 g·cm⁻³ [33].

2.9. Hydrogels morphologies

The morphologies of hydrogels were evaluated through SEM images. PVA-GMA100, PVA-GMA90/CS10 and PVA-GMA80/CS20 cylindrical hydrogels surface images were obtained in an 8 keV scanning electron microscope (SEM, Shimadzu, model SS550). The hydrogels were firstly immersed in distilled water at room temperature (ca. 25°C) up to

swelling at equilibrium (ca. 48 h). Next, the samples were removed and immediately frozen by dipping in liquid nitrogen. Thereafter, the frozen samples were fractured and lyophilized in a freeze dryer (Christ Gefriertrocknungsanlagen) at -55°C for 24 h. The lyophilized hydrogels were gold-coated by sputtering before the observation by SEM.

2.10. Evaluation of cytotoxicity

Hydrogel cytotoxicity was evaluated according to the ASTM-F813-01 [34] procedure in a similar way had done by Malmonge *et al.* [35]. Cylindrical hydrogels samples with 10 mm diameter and the controls, silicon (as positive) and HDPE plate (as negative), were cut in disc shape with 2 mm of thickness. The samples were swelled in distilled-deionized water for 48 h. The water content was renewed every 6 h. The hydrogels and controls were sterilized in autoclave (121°C for 15 min). Each sample was placed in a cover slip in a Leighton tube and kept in 2 mL of DMEM medium supplemented with 10% Fetal Bovine Serum (FBS) for 24 h at 37°C in humidified 95% air 5% CO_2 (v/v) before the inoculation. An aliquot of Vero cell line (1 mL – conc. equal to 10^5 cells $\cdot\text{mL}^{-1}$) was transferred to each Leighton tube and cultivated in DMEM containing 10% FBS. The samples were incubated at 37°C for 48 h in humidified 95% air 5% CO_2 . After a period of 48 h from the incubation, the culture media were collected and unviable cells were assessed by trypan blue dye (conc. equal to 0.1% in 0.9% salt) exclusion test in a Neubauer chamber.

3. Results and discussion

All hydrogels synthesized in this work show opacity, indicating that PVA-GMA is less hydrophilic than raw PVA is. All PVA-GMA67/CS33 hydrogel preparation runs resulted in irregular bubbly material, which was attributed to the high viscosity of the feed solutions used for the synthesis. In this way, the obtained PVA-GMA67/CS33 hydrogels were very fragile. Thus, tests for determinate the mechanical properties and the swelling kinetics assays on PVA-GMA67/CS33 hydrogel were not performed. According to our laboratory's previous work [29], in the optimized conditions (62°C and 6 h) the achieved DS for the chemical modification of PVA with GMA was 4.63% while the expected

was 4.85% [29]. Additionally, it was found that in these optimized conditions the DS changed linearly with the $[-\text{OH}(\text{PVA})/\text{GMA}]$ ratio up to 1/0.25 [29]. Thus, in this work, it was assumed that the DS of the all PVA-GMA used in the hydrogel synthesis was the same as the nominal ones.

3.1. FTIR spectroscopy

The Figure 1a–d shows the FTIR spectra of PVA-GMA100, PVA-GMA90/CS10, PVA-GMA67/CS33 hydrogels, and pure CS, respectively. The FTIR spectroscopy technique was applied to characterize the insertion of CS within the hydrogel matrix. For this reason, FTIR spectra of the hydrogels with the higher and lower amounts of CS (PVA-GMA90/CS10 and PVA-GMA67/CS33) were obtained. The FTIR spectrum of PVA-GMA100 hydrogel (Figure 1a) presents a broad band at 3421 cm^{-1} assigned to the $-\text{OH}$ stretching, a band at 2936 cm^{-1} assigned to C–H vibrational stretching, and a band at 1094 cm^{-1} assigned to C–O vibrational stretching. Moreover, the bands at 1727 and 1642 cm^{-1} , which are assigned to C=O and C=C stretching, proceeding from methacrylate groups of GMA used for modifying PVA [36].

The FTIR spectrum of CS (Figure 1d) shows a broad band between $3100\text{--}3600\text{ cm}^{-1}$ assigned to $-\text{OH}$ and to N–H vibrational stretching in which the $-\text{OH}$ stretching overlaps the N–H one. The bands close to 1650 and 1050 cm^{-1} were assigned to amide bands and to C–O vibration stretching respectively. A quite broad band appears at 1424 cm^{-1} , which was assigned to C–O stretching and O–H angular coupling vibration. This band indicates the exis-

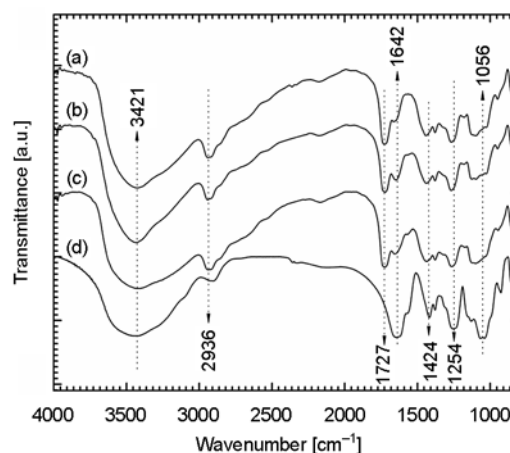


Figure 1. FTIR spectra of (a) PVA-GMA100, (b) PVA-GMA90/CS10, (c) PVA-GMA67/CS33 hydrogels and (d) pure CS

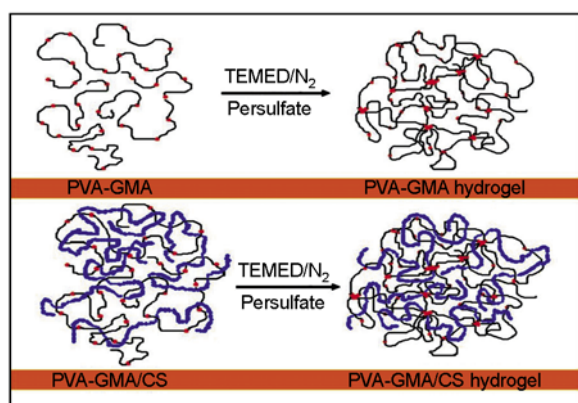


Figure 2. Scheme for the synthesis of PVA-GMA hydrogel (above) and PVA-GMA/CS semi-IPN hydrogel (below)

tence of free carboxyl groups. The band assigned to the vibrational stretching of S=O bonds from sulfate groups, characteristic of CS, appears at 1254 cm^{-1} . Figure 1b–c shows the FTIR spectra of PVA-GMA90/CS10, PVA-GMA67/CS33 hydrogels and comparing with the PVA-GMA100 spectrum it was not observed significant changes caused by CS insertion within the hydrogel matrix. It was observed an enlargement of the band assigned to –OH stretching according to increase of the amount of CS in the hydrogel formulation. Furthermore, an increase in the intensity of the band at 1642 cm^{-1} , assigned to the amide bands from CS, was observed. The semi-IPN hydrogel is formed by the crosslinking of PVA-GMA and the CS remains in linear form within the matrix, as sketched in the Figure 2. For this reason, great changes on PVA-GMA/CS FTIR spectra related to PVA-GMA100 FTIR spectrum were not observed.

3.2. Degree of swelling

All hydrogels samples achieve the equilibrium swelling at immersion times lower than 48 h. The dependence of q to DS of parent PVA-GMA for PVA-GMA100, PVA-GMA90/CS10, PVA-GMA80/CS20, and PVA-GMA67/CS33 hydrogels, at 25°C , is shown in Figure 3. As expected, the q values decrease as the DS increases. This fact was attributed to the augment in the degree of cross-linking in the hydrogel matrix due to DS rising. Higher DS means high amount of methacrylate groups attached on PVA chains. These reactive groups are likely to react during gelling reaction, as they react with each other to form a cross-linking point. The increase in

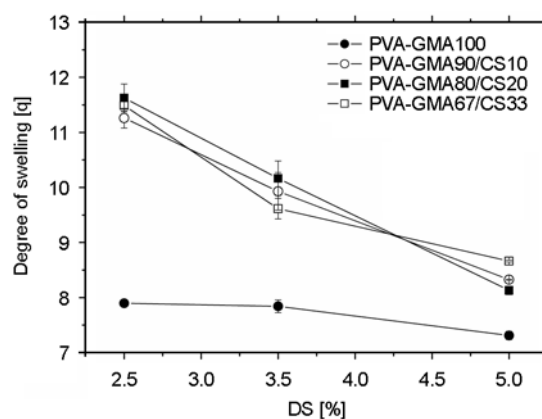


Figure 3. Degree of swelling as a function of DS of PVA-GMA presents in the hydrogel samples: PVA-GMA100, PVA-GMA90/CS10, PVA-GMA80/CS20, and PVA-GMA67/CS33

the cross-linking degree limits the matrix expansion and then lesser water amount is absorbed, reducing the q value.

The reduction in q as the DS increases is less significant in PVA-GMA100 hydrogels than those containing CS. At a fixed DS, the hydrogels containing CS presented high q values comparatively to the respective PVA-GMA100, fact attributed to the substantial hydrophilic character of CS. This is a detachable feature presented by the glycosaminoglycans, that constitutes the extracellular matrix and conjunctive tissues, which presents excellent water uptake and retention capabilities [27]. However, no significant difference was observed in q values for PVA-GMA/CS hydrogels, at fixed DS, even using different amounts of CS ($10 < \text{CS} < 33\text{ wt}\%$).

The swelling data allow inferring that the mobility of PVA-GMA chains governs the effect of CS on q values of PVA-GMA/CS hydrogels. In this case, using the PVA-GMA with low DS would let the hydrogel to have both large chain mobility and high water uptake. However, the PVA-GMA chain mobility itself (absence of CS) is not enough to raise the q value as occurred when CS is present in the matrix. It should be highlighted that the CS chains are not covalently bound to the PVA-GMA matrix. Based on Figure 3, it can be inferred that highly cross-linked PVA-GMA/CS hydrogels would present q values closer to those of their respective PVA-GMA. Therefore, in highly cross-linked PVA-GMA/CS the effect of CS in q was weakened.

3.3. Hydrogel mechanical properties

The curves of compressive stress (σ) as a function of $(\alpha - \alpha^{-2})$ for PVA-GMA100 and PVA-GMA90/CS10 hydrogels are presented in the Figures 4a and 4b, respectively, at three different DS [DS = 2.5, 3.5 and 5.0%] of PVA-GMA.

The curves are almost linear, which indicates that the compressive tests produce predominantly elastic (reversible) deformations in the studied range of strain ($0 \leq \alpha \leq 1.10$). Thus, the value of elastic modulus, E , for each hydrogel was obtained from the slope of the σ vs. $(\alpha - \alpha^{-2})$ curve, as those shown in the Figures 4a and 4b. Figure 5 shows the dependence of E to the nominal DS of PVA-GMA for PVA-GMA100, PVA-GMA90/CS10, and PVA-GMA80/CS20. The values of E ranged from 63 to 126 kPa. Peppas and Merrill [37] obtained wider range for E values (31 to 340 kPa) using PVA hydrogels cross-linked by electron beam irradiating 10 wt% polymer aqueous solution. These authors observed that for those polymers the value of E depends on the radiation dose due to its effect in the degree of cross-linking.

The PVA-GMA hydrogels obtained using PVA-GMA with DS = 5.0% were more rigid and thus presented high E values. Compared to PVA-GMA hydrogels, the presence of CS in the hydrogels lowered the values of E modulus, which agrees with the

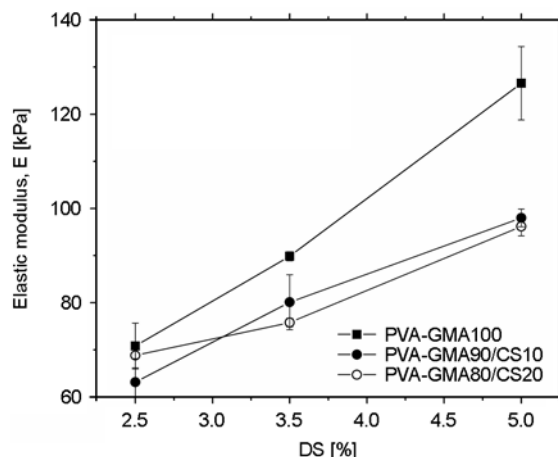


Figure 5. Elastic modulus, E , as a function of DS to PVA-GMA100, PVA-GMA90/CS10 and PVA-GMA80/20 hydrogels samples

swelling data presented in the Figure 3. Figure 5 shows that E of PVA-GMA100 increases by ca. 80% as the DS of PVA-GMA changes from 2.5 to 5.0%, while the Figure 3 shows that, for the same hydrogels and DS range, the variation in q values is only 7%. Therefore, besides the PVA-GMA DS has little and negative effect on the q of PVA-GMA100 hydrogels it induces a strong rise in their elastic modulus.

The cross-linking density, ν_e , and the molar mass between two consecutive cross-links, M_c , were calculated with Equations (5) and (6), respectively.

Table 2. Cross-linking density, ν_e , molar mass between cross-links, M_c , shear modulus, G , and volumetric fractions ($\phi_{2,r}$ and $\phi_{2,s}$) of PVA-GMA100 at different DS values measured at 25°C

DS [%]	$\phi_{2,r}$	$\phi_{2,s}$	G [kPa]	ν_e [mol·m ⁻³]	M_c [g·mol ⁻¹]
2.5	0.1051±0.0002	0.1026±0.0003	23.60±1.62	91.4±6.3	4590±104
3.5	0.1049±0.0017	0.1033±0.0016	29.95±0.32	115.9±3.0	4214±43
5.0	0.1122±0.0015	0.1110±0.0012	42.19±2.59	152.4±11.2	3762±125

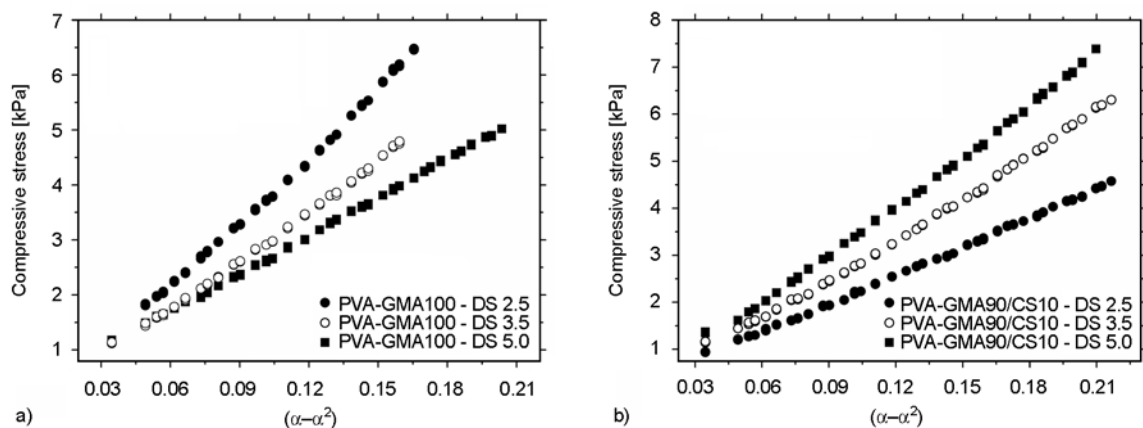


Figure 4. Compressive stress as a function of $(\alpha - \alpha^{-2})$ of PVA-GMA100 (a) and PVA-GMA90/CS10 (b) at DS equal to 2.5, 3.5, and 5.0%

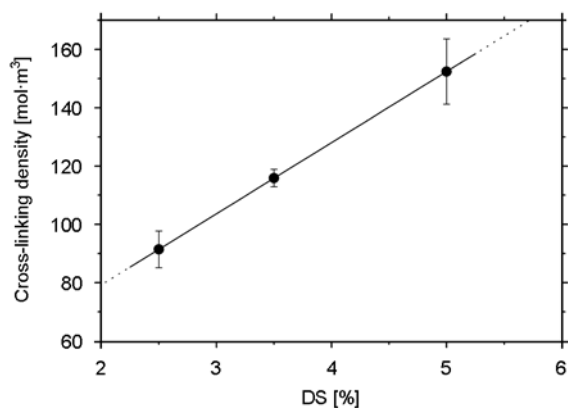


Figure 6. Cross-linking density, v_c , as function of DS of PVA-GMA100 hydrogels

Table 2 shows the v_c and M_c values of PVA-GMA100 hydrogels along with the values of $\varphi_{2,r}$ and $\varphi_{2,s}$. The v_c and M_c for PVA-GMA/CS hydrogels were not calculated due to the ambiguity on calculation caused by contribution of CS to these parameters. The plot of v_c of PVA-GMA100 hydrogels as a function of the DS values of parents PVA-GMA

produced a straight line (see Figure 6). The line extrapolated for DS equal to 0 provides the net contribution of PVA-GMA chain entanglements to v_c^0 which was ca. $30.5 \text{ mol}\cdot\text{m}^{-3}$. It should be emphasized that the chain entanglements affect positively the E values and, consequently, improve the hydrogel mechanical properties as well [38].

3.4. Swelling kinetics

The curves of q as a function of immersion time in SGF (pH 1.2) for PVA-GMA100, PVA-GMA90/CS10 and PVA-GMA80/CS20 hydrogels are presented in the Figure 7a (DS = 2.5%) and in the Figure 7b (DS = 5.0%). By comparison of the different curves of q vs. immersion time presented in the Figure 7a (SGF, pH 1.2), a negative effect on q values caused by presence of CS can be observed. This effect is opposite to that observed for immersion of hydrogels in pure water (see Figure 3) and is attributed to ionization of carboxylic groups of CS in water, while the lowering the amount of charged

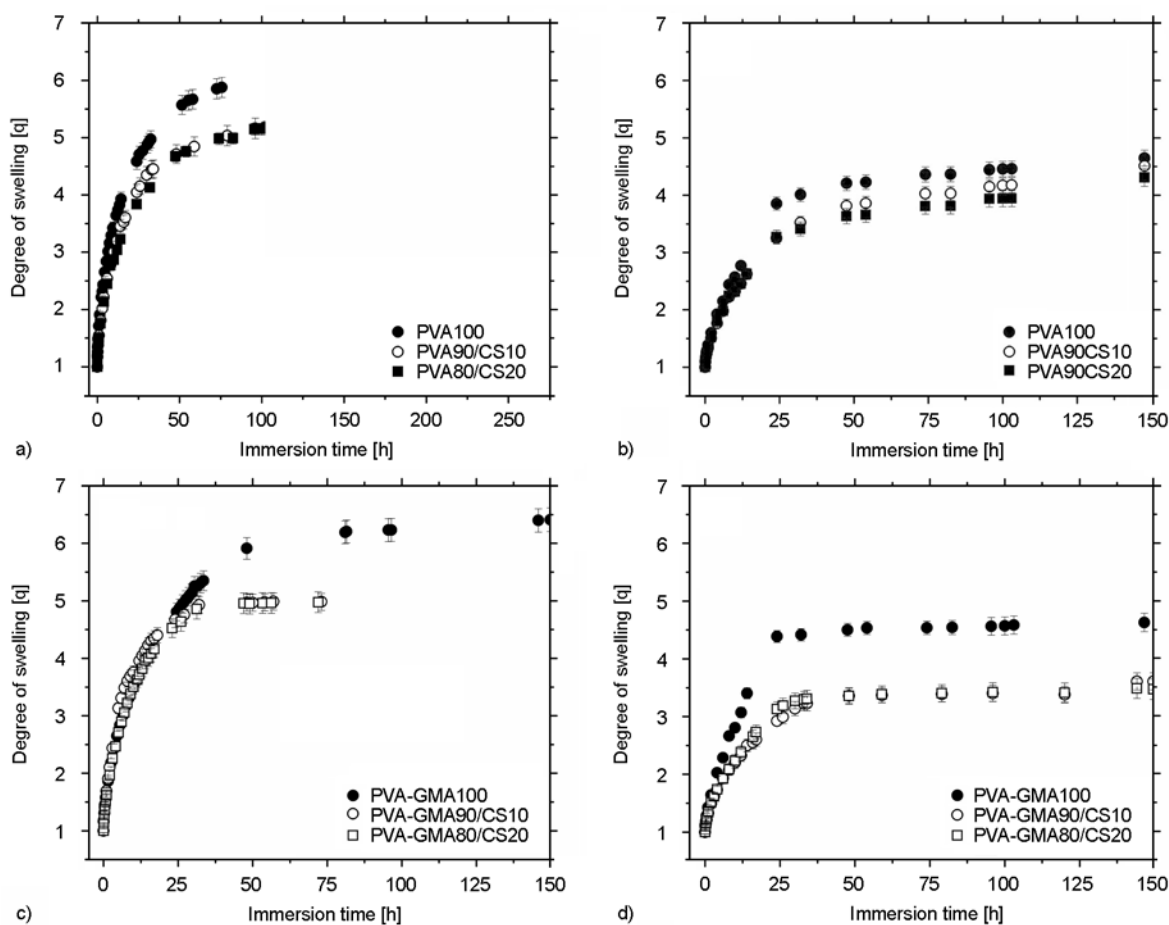


Figure 7. Degree of swelling as a function of immersion time in SGF (pH 1.2) at 37°C of PVA-GMA100, PVA-GMA90/CS10, and PVA-GMA80/CS20 hydrogels samples with DS = 2.5 (a) and 5.0% (b) and in SIF (pH 7.5) at 37°C of PVA-GMA100, PVA-GMA90/CS10, and PVA-GMA80/CS20 hydrogels samples (c) DS = 2.5 and (d) DS = 5.0%

moieties on CS at pH 1.2. In this situation, there is no significant repulsion among the CS segments. A common characteristic of ionic hydrogels is the repulsion of charged segments, which enhances the water, and other fluids, uptake capacity [39]. Curves similar to those shown in the Figure 7a were also obtained for PVA-GMA100, PVA-GMA90/CS10, and PVA-GMA80/CS20 hydrogels at DS = 3.5% (not shown here). However, the profile of q vs. immersion time of PVA-GMA and PVA-GMA/CS hydrogels as the DS of parent PVA-GMA was fixed at 5.0% is noticeably different, as shown in the Figure 7b. The q values at DS = 5.0% are remarkably lower and the equilibrium swelling is reached faster than at DS = 2.5%. The increase in cross-linking density of ca. $60 \text{ mol}\cdot\text{m}^{-3}$ for a DS change from 2.5 to 5.0% (see Figure 6) accounts for the additional matrix compaction and leads to an opposite net effect on swelling.

The curves of q as a function of immersion time in SIF (pH 7.5) for PVA-GMA100, PVA-GMA90/CS10 and PVA-GMA80/CS20 hydrogels are presented in the Figure 7c (DS = 2.5%) and the Figure 7d (DS = 5.0%). At the beginning, being the carboxylic groups either totally or partially charged in SIF we expected an enhancement in q compared to SGF. In fact, the results show that equilibrium q values in SIF are almost the same as compared to the respective ones when swelled in SGF, but the equilibrium reached faster in SIF as compared to SGF.

It was expected that the swelling degree in Figure 7d for SIF would be higher than at SGF (Figure 7b). This unexpected finding is under investigation. There are two different possibilities: one of

them is the degradation of matrix (no apparent signal of degradation was observed). Another would be the release of chondroitin sulfate out of 3D matrix (the authors also have no evidence for that). It should be emphasized that PVA-GMA100 and PVA-GMA/CS hydrogels did not present apparent degradation under SIF or SGF swelling during 150 h after the immersion. The values of k and n obtained from Equation (2) for SGF and SIF are shown in Tables 3 and 4 for SGF (pH 1.2) and SIF (pH 7.5), respectively. The k values at SIF are higher than those calculated at SGF. This indicates a higher speed in swelling at higher pH-condition. The main reason is the complete ionization of side groups on CS leading to repulsion among the CS chains at SIF. In spite of that, the PVA-GMA/CS hydrogels presented almost the same q values in SGF as compared to SIF.

The values of n for the hydrogels ranged from 0.54 to 0.59 as swelled in SGF and from 0.55 to 0.62 as swelled in SIF. As pointed out by Ritger and Peppas [40], n values ranged from 0.45 to 1.0 for cylindrical hydrogels indicate anomalous mechanisms of transport during swelling. In this case, both diffusion and chain relaxation govern the fluid transport into hydrogel [40]. Drugs are more easily released out from hydrogel as the matrix is highly swelled than as compacted. Therefore, it is important to know the kinetic of swelling in drug carrier systems because the drug release rate is related to.

3.5. Hydrogel morphology by SEM

The effect of CS on hydrogel porosity relative to their respective PVA-GMA100 matrix, as control, was analyzed by SEM. Figure 8 presents the images

Table 3. Swelling kinetics parameters, k and n , for PVA-GMA100, PVA-GMA90/CS10, and PVA-GMA80/CS20 hydrogels samples in SGF (pH 1.2) at 37°C

DS [%]	PVA-GMA100		PVA-GMA90/CS10		PVA-GMA80/CS20	
	k [10^{-1}]	n	k [10^{-1}]	n	k [10^{-1}]	n
2.5	1.50±0.16	0.535±0.013	1.16±0.10	0.567±0.001	1.22±0.13	0.552±0.004
3.5	1.69±0.56	0.593±0.024	1.19±0.07	0.572±0.001	1.25±0.09	0.546±0.005
5.0	1.18±0.09	0.581±0.004	1.19±0.23	0.563±0.002	1.29±0.26	0.554±0.010

Table 4. Swelling kinetics parameters, k and n , for PVA-GMA100, PVA-GMA90/CS10, and PVA-GMA80/CS20 hydrogels samples in SIF (pH 7.5) at 37°C

DS [%]	PVA-GMA100		PVA-GMA90/CS10		PVA-GMA80/CS20	
	k [10^{-1}]	n	k [10^{-1}]	n	k [10^{-1}]	n
2.5	1.33±0.07	0.560±0.002	1.55±0.26	0.589±0.039	1.39±0.21	0.582±0.016
3.5	1.11±0.01	0.558±0.008	1.36±0.01	0.553±0.002	1.32±0.11	0.578±0.010
5.0	1.47±0.24	0.616±0.023	1.39±0.16	0.572±0.004	1.43±0.14	0.585±0.010

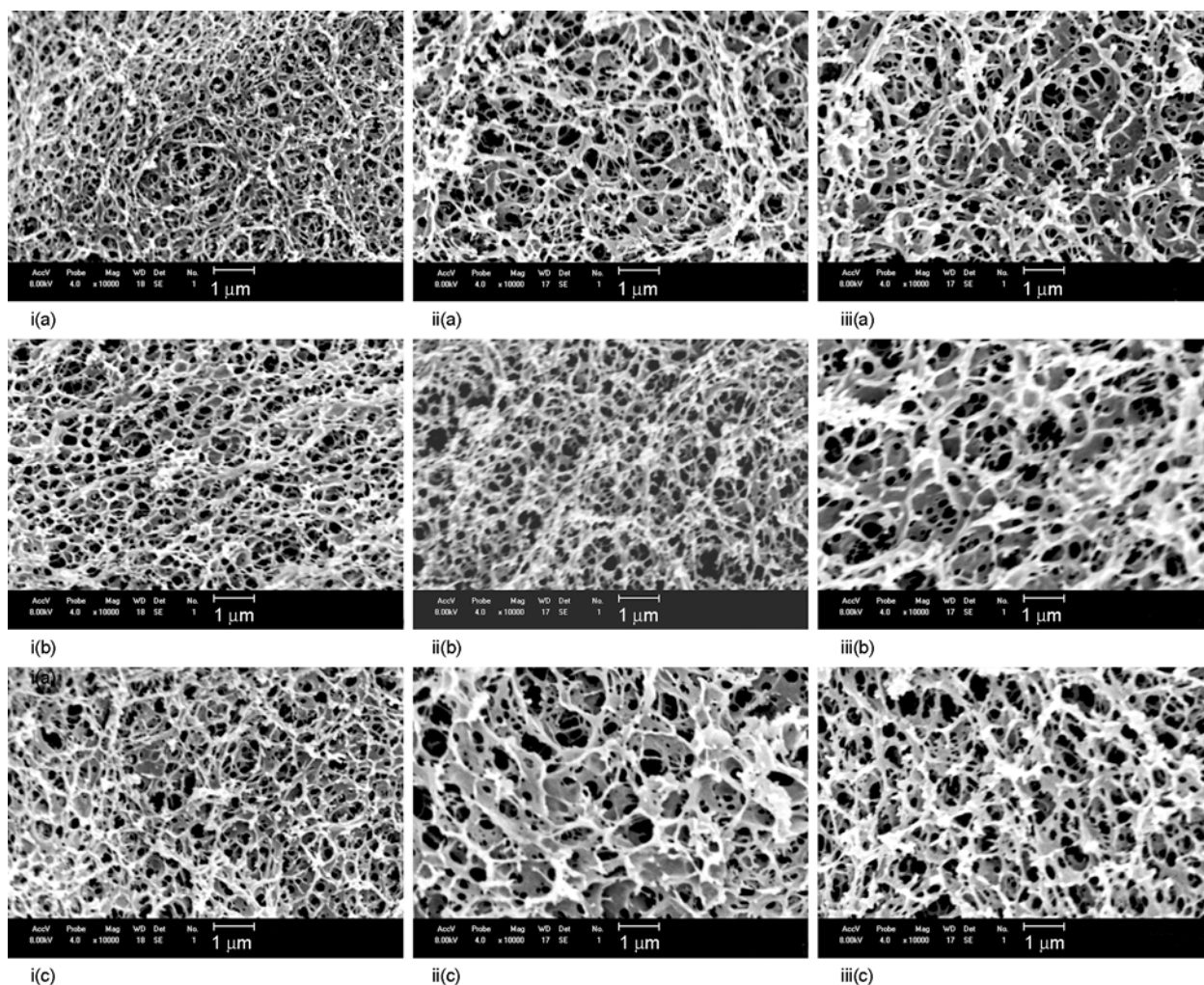


Figure 8. SEM images of PVA-GMA100 (i(a–c)), PVA-GMA90/CS10 (ii(a–c)), PVA-GMA80/CS20 (iii(a–c)) at DS 2.5% (i–iii(a)), 3.5% (i–iii(b)), and 5.0% (i–iii(c)). Magnification: 10 000 \times .

obtained at 10 000-fold magnification of PVA-GMA100 (i(a–c)), PVA-GMA90/CS10 (ii(a–c)), PVA-GMA80/CS20 (iii(a–c)) hydrogels made from precursor PVA-GMA with DS = 2.5% (i–iii(a)), 3.5% (i–iii(b)), and 5.0% (i–iii(c)). As can be seen, the presence of CS causes pore enlargement; however, the distribution remains inhomogeneous in all cases. For PVA-GMA90/CS10 and PVA-GMA80/CS20 hydrogels at DS 5.0%, the morphology seems to be foliaceous. At DS 2.5 and 3.5%, it was expected to obtain less porous hydrogels than the respective PVA-GMA100 but it was not verified. The reason for that is as follows: the PVA-GMA100 hydrogel at DS = 5.0% gels up to 30 s after the addition of persulfate, while the PVA-GMA100 hydrogels at DS = 2.5 and 3.5% gel ca. 3 min after the addition of persulfate. In this way, PVA-GMA hydrogels at DS 5.0% tend to present higher heterogeneity in pore sizes. Another possible contributing factor is

the buildup in viscosity due to the presence of CS in PVA-GMA/CS hydrogels. Micro-heterogeneity enhances pore size in hydrogels [41]. Plenty of hydrogels with different porous sizes have been published in the literature [42] and in smart-hydrogels, the porous size can be controlled by external stimuli as temperature [43], pH [44], electrical discharge [45], to notice only few of them.

From the SEM images showed in Figure 8, the average pore size of each hydrogel samples was estimated through the computational software Size Meter[®], version 1.1 with differentiation threshold set according to the image scale. Since the pore shape was undefined, the measurements were taken between the extreme points of the pores. The average was calculated from the measurement of 100 randomly selected pores. The results are shown in Table 5.

Table 5. Average pore size of the hydrogel samples

Sample	DS	Average Pore Size[μm]
PVA-GMA100	2.5	0.2617 \pm 0.0107
PVA-GMA90/CS10	2.5	0.3177 \pm 0.0445
PVA-GMA80/CS20	2.5	0.3683 \pm 0.0238
PVA-GMA100	3.5	0.3053 \pm 0.0123
PVA-GMA90/CS10	3.5	0.3009 \pm 0.0096
PVA-GMA80/CS20	3.5	0.3670 \pm 0.0443
PVA-GMA100	5.0	0.3195 \pm 0.0176
PVA-GMA90/CS10	5.0	0.3650 \pm 0.0306
PVA-GMA80/CS20	5.0	0.4376 \pm 0.0400

3.6. Evaluation of hydrogel cytotoxicity

The evaluation of cytotoxicity on PVA-GMA100, PVA-GMA90/CS10, PVA-GMA80/CS20 and PVA-GMA67/CS33 hydrogels at DS 2.5, 3.5, or 5.0% were done through *Vero* cells culturing. Figure 9 presents the percentage of cell growth inhibition for each case, considering the number of cells in the positive control as 100% of inhibition.

Figure 9 evidences that the hydrogels are mostly non-toxic for *Vero* cells growth. In fact, PVA-GMA/CS hydrogels presented lower inhibition capability than the PVA-GMA100 hydrogels did. The more intense effect was observed on hydrogel at high CS content. Such effect was attributed to the biological nature of CS, which is often found in animal extracellular matrix proteoglycans and considered as responsible for cell adherence and fixation. However, comparatively to the controls, cytotoxicity was slightly increased in hydrogels prepared at the precursor PVA-GMA.

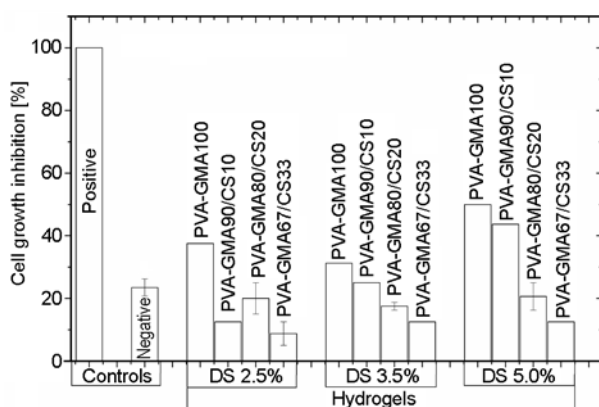


Figure 9. Cell growth inhibition (in %) evaluated by non-viable cultured *Vero* cells count on the different hydrogels samples and controls as substrates

4. Conclusions

Hydrogels were prepared in presence of chondroitin sulfate (CS) at 0, 10, 20 and 33wt-% by gelling of chemically modified poly(vinyl alcohol) (PVA-GMA). Different degrees of substitution, DS, on PVA-GMA [2.5, 3.5 and 5.0%] were achieved. The presence of CS into the hydrogels enhanced their hydrophilic feature and improved its cell viability. In addition, the hydrogels presented improved handling, except for PVA-GMA67/CS33. The values of elastic modulus, E , spread from 63 to 126 kPa and are proportional to the DS of parent PVA-GMA, but they decrease slightly with the presence of CS. The hydrogels presented anomalous water uptake mechanism. Thus, Fickian diffusion and polymer chain relaxation govern the swelling of these hydrogels. PVA-GMA100 and PVA-GMA/CS hydrogels are resistant at pH 1.2 (SGF) and pH 7.5 (SIF). This interesting feature allows the hydrogels acting as a carrier for drug releasing in both media, protecting the drug against a degradation process, for example. Compared to the negative (polyethylene) and positive (silicon), used as controls, the presence of CS enhances the hydrogel-cell compatibility, results from cell viability tests. These results indicate the potential application of these materials as scaffolds in cell culture. Therefore, the PVA-GMA100 and PVA-GMA/CS hydrogels developed and characterized in this work present characteristics that allow them to be used as biomaterial, as a carrier in drug delivery system or to act as scaffolds in tissue engineering as well.

Acknowledgements

The authors thank Dep. de Ciência e Tecnologia de Alimentos (UEL, Londrina, Brazil) for the use of (TA.TXT2 Stable Micro System). The authors also thank to CNPq/Capes, Brazil, by the fellowships and financial support [Proc. 308611/2006-3].

References

- [1] Hoffman A. S.: Hydrogels for biomedical applications. *Advanced Drug Delivery Reviews*, **54**, 3–12 (2002). DOI: [10.1016/S0169-409X\(01\)00239-3](https://doi.org/10.1016/S0169-409X(01)00239-3)

- [2] Byrne E. M., Park K., Peppas N. A.: Molecular imprinting within hydrogels. *Advanced Drug Delivery Reviews*, **54**, 149–161 (2002). DOI: [10.1016/S0169-409X\(01\)00246-0](https://doi.org/10.1016/S0169-409X(01)00246-0)
- [3] Krupa I., Nedelčev T., Račko D., Lacik I.: Mechanical properties of silica hydrogels prepared and aged at physiological conditions: Testing in the compression mode. *Journal of Sol-Gel Science and Technology*, **53**, 107–114 (2010). DOI: [10.1007/s10971-009-2064-5](https://doi.org/10.1007/s10971-009-2064-5)
- [4] Oliveira J. T., Martins L., Picciochi R., Malafaya P. B., Sousa R. A., Neves N. M., Mano J. F., Reis R. L.: Gellan gum: A new biomaterial for cartilage tissue engineering applications. *Journal of Biomedical Materials Research Part A*, **93**, 852–863 (2010). DOI: [10.1002/jbm.a.32574](https://doi.org/10.1002/jbm.a.32574)
- [5] Qiu Y., Park K.: Environment-sensitive hydrogels for drug delivery. *Advanced Drug Delivery Reviews*, **53**, 321–339 (2001). DOI: [10.1016/S0169-409X\(01\)00203-4](https://doi.org/10.1016/S0169-409X(01)00203-4)
- [6] Gutowska A., Bae Y. H., Jacobs H., Feijen J., Kim S. W.: Thermosensitive interpenetrating polymer networks: Synthesis, characterization, and macromolecular release. *Macromolecules*, **27**, 4167–4175 (1994). DOI: [10.1021/ma00093a018](https://doi.org/10.1021/ma00093a018)
- [7] Cascone M. G., Barbani N., Giusti P., Cristallini C., Ciadelli G., Lazzeri L.: Bioartificial polymeric materials based on polysaccharides. *Journal of Biomaterials Science, Polymer Edition*, **12**, 267–281 (2001). DOI: [10.1163/156856201750180807](https://doi.org/10.1163/156856201750180807)
- [8] Chiellini E., Cinelli P., Chiellini F., Imam S. H.: Environmentally degradable bio-based polymeric blends and composites. *Macromolecular Bioscience*, **4**, 218–231 (2004). DOI: [10.1002/mabi.200300126](https://doi.org/10.1002/mabi.200300126)
- [9] Zhang L., Yu P., Luo Y.: Dehydration of caprolactam–water mixtures through cross-linked PVA composite pervaporation membranes. *Journal of Membrane Science*, **306**, 93–102 (2007). DOI: [10.1016/j.memsci.2007.08.036](https://doi.org/10.1016/j.memsci.2007.08.036)
- [10] DeMerlis C. C., Schoneker D. R.: Review of the oral toxicity of polyvinyl alcohol (PVA). *Food and Chemical Toxicology*, **41**, 319–326 (2003). DOI: [10.1016/S0278-6915\(02\)00258-2](https://doi.org/10.1016/S0278-6915(02)00258-2)
- [11] Kelly C. M., DeMerlis C. C., Schoneker D. R., Borzelleca J. E.: Subchronic toxicity study in rats and genotoxicity tests with polyvinyl alcohol. *Food and Chemical Toxicology*, **41**, 719–727 (2003). DOI: [10.1016/S0278-6915\(03\)00003-6](https://doi.org/10.1016/S0278-6915(03)00003-6)
- [12] Wang Y., Hsieh Y.-L.: Crosslinking of polyvinyl alcohol (PVA) fibrous membranes with glutaraldehyde and PEG diacylchloride. *Journal of Applied Polymer Science*, **116**, 3249–3255 (2010). DOI: [10.1002/app.31750](https://doi.org/10.1002/app.31750)
- [13] Shaheen M. S., Yamaura K.: Preparation of theophylline hydrogels of atactic poly(vinyl alcohol)/NaCl/H₂O system for drug delivery system. *Journal of Controlled Release*, **81**, 367–377 (2000). DOI: [10.1016/S0168-3659\(02\)00085-8](https://doi.org/10.1016/S0168-3659(02)00085-8)
- [14] Kudo S., Otsuka E., Suzuki A.: Swelling behavior of chemically crosslinked PVA gels in mixed solvents. *Journal of Polymer Science Part B: Polymer Physics*, **48**, 1978–1986 (2010). DOI: [10.1002/polb.22076](https://doi.org/10.1002/polb.22076)
- [15] Reis A. V., Fajardo A. R., Schuquel I. T. A., Guilherme M. R., Vidotti G. J., Rubira A. F., Muniz E. C.: Reaction of glycidyl methacrylate at the hydroxyl and carboxylic groups of poly(vinyl alcohol) and poly(acrylic acid): Is this reaction mechanism still unclear? *The Journal of Organic Chemistry*, **74**, 3750–3757 (2009). DOI: [10.1021/jo900033c](https://doi.org/10.1021/jo900033c)
- [16] Valente A. J. M., Cruz S. M. A., Morán M. C., Murtinho D. B., Muniz E. C., Miguel M. G.: Release of DNA from cryogel PVA-DNA membranes. *Express Polymer Letters*, **4**, 480–487 (2010). DOI: [10.3144/expresspolymlett.2010.61](https://doi.org/10.3144/expresspolymlett.2010.61)
- [17] Martens P., Anseth K. S.: Characterization of hydrogels formed from acrylate modified poly(vinyl alcohol) macromers. *Polymer*, **41**, 7715–7722 (2000). DOI: [10.1016/S0032-3861\(00\)00123-3](https://doi.org/10.1016/S0032-3861(00)00123-3)
- [18] Reis A. V., Guilherme M. R., Mattoso L. H. C., Rubira A. F., Tambourgi E. B., Muniz E. C.: Nanometer- and submicrometer-sized hollow spheres of chondroitin sulfate as a potential formulation strategy for anti-inflammatory encapsulation. *Pharmaceutical Research*, **26**, 438–444 (2009). DOI: [10.1007/s11095-008-9732-y](https://doi.org/10.1007/s11095-008-9732-y)
- [19] Eastman S. A., Lesser A. J., McCarthy T. J.: Quantitative poly(vinyl alcohol) modification in ionic liquids: Esterification and urethanation with low surface tension producing reagents. *Macromolecules*, **43**, 4584–4588 (2010). DOI: [10.1021/ma100458v](https://doi.org/10.1021/ma100458v)
- [20] Zhao L., Xiong W., Liu M., Qi Z.: Study on superabsorbent of maleic anhydride/acrylamide semi-interpenetrated with poly(vinyl alcohol). *Polymer for Advanced Technologies*, **21**, 483–489 (2010). DOI: [10.1002/pat.1456](https://doi.org/10.1002/pat.1456)
- [21] Gao B. J., Lu J. H., Zhuang R. B., Zhang G. H.: Preparation of poly(vinyl amine)-grafted crosslinked poly(vinyl alcohol) microspheres. *Journal of Applied Polymer Science*, **114**, 3487–3494 (2009). DOI: [10.1002/app.30892](https://doi.org/10.1002/app.30892)
- [22] Ghugare S. V., Mozetic P., Paradossi G.: Temperature-sensitive poly(vinyl alcohol)/poly(methacrylate-*co*-*N*-isopropyl acrylamide) microgels for doxorubicin delivery. *Biomacromolecules*, **10**, 1589–1596 (2009). DOI: [10.1021/bm900185u](https://doi.org/10.1021/bm900185u)

- [23] Maris B., Verheden L., Van Reeth K., Samyn C., Augustijns P., Kinget R., Van den Mooter A.: Synthesis and characterisation of inulin-azo hydrogels designed for colon targeting. *International Journal of Pharmaceutics*, **213**, 143–152 (2001).
DOI: [10.1016/S0378-5173\(00\)00654-2](https://doi.org/10.1016/S0378-5173(00)00654-2)
- [24] Pitarresi G., Palumbo F. S., Giommona G., Casadei M. A., Micheletti Moracci F.: Biodegradable hydrogels obtained by photocrosslinking of dextran and polyaspartamide derivatives. *Biomaterials*, **24**, 4301–4313 (2003).
DOI: [10.1016/S0142-9612\(03\)00332-6](https://doi.org/10.1016/S0142-9612(03)00332-6)
- [25] Lee C-T., Kung P-H., Lee Y-D.: Preparation of poly(vinyl alcohol)-chondroitin sulfate hydrogel as matrices in tissue engineering. *Carbohydrate Polymers*, **61**, 348–354 (2005).
DOI: [10.1016/j.carbpol.2005.06.018](https://doi.org/10.1016/j.carbpol.2005.06.018)
- [26] Avci F. Y., Toida T., Linhardt R. J.: Chondroitin *O*-methyl ester: An unusual substrate for chondroitin AC lyase. *Carbohydrate Research*, **338**, 2101–2104 (2003).
DOI: [10.1016/S0008-6215\(03\)00348-3](https://doi.org/10.1016/S0008-6215(03)00348-3)
- [27] Kartal F., Akkaya A., Kilinc A.: Immobilization of porcine pancreatic lipase on glycidyl methacrylate grafted poly vinyl alcohol. *Journal of Molecular Catalysis B: Enzymatic*, **57**, 55–61 (2009).
DOI: [10.1016/j.molcatb.2008.06.016](https://doi.org/10.1016/j.molcatb.2008.06.016)
- [28] Iwafune M., Kakizaki I., Nakazawa H., Nukatsuka I., Endo M., Takagaki K.: A glycomic approach to proteoglycan with a two-dimensional polysaccharide chain map. *Analytical Biochemistry*, **325**, 35–40 (2004).
DOI: [10.1016/S0003-2697\(03\)00391-9](https://doi.org/10.1016/S0003-2697(03)00391-9)
- [29] Crispim E. G., Piai J. F., Rubira A. F., Muniz E. C.: Addition of methacryloil groups to poly(vinyl alcohol) in DMSO catalyzed by TEMED: Optimization through response surface methodology. *Polymer Testing*, **25**, 377–383 (2006).
DOI: [10.1016/j.polymertesting.2005.12.003](https://doi.org/10.1016/j.polymertesting.2005.12.003)
- [30] USP 23-NF18: U.S. Pharmacopeia: National formulary supplement. (1995).
- [31] Lin C-C., Metters A. T.: Hydrogels in controlled release formulations: Network design and mathematical modeling. *Advanced Drug Delivery Reviews*, **58**, 1379–1408 (2006).
DOI: [10.1016/j.addr.2006.09.004](https://doi.org/10.1016/j.addr.2006.09.004)
- [32] Sperling L. H.: Introduction to physical polymer science. Wiley, New York (2006).
- [33] Paradossi G., Cavalieri F., Capitani D., Crescenzi V.: Physicochemical characterization of chemical hydrogels based on PVA. *Journal of Polymer Science Part B: Polymer Physics*, **37**, 1225–1233 (1999).
DOI: [10.1002/\(SICI\)1099-0488\(19990615\)37:12<1225::AID-POLB4>3.0.CO;2-P](https://doi.org/10.1002/(SICI)1099-0488(19990615)37:12<1225::AID-POLB4>3.0.CO;2-P)
- [34] ASTM-F813-01: Standard Practice for direct contact cell culture evaluation of materials for medical devices (2005).
- [35] Malmonge S. M., Zavaglia C. A. C., Santos A. J., Wada M. L. F.: Citotoxicity evaluation for polyhema hydrogels: An in vitro study (in Portuguese). *Revista Brasileira de Engenharia Biomédica*, **15**, 49–54 (1999).
- [36] Crispim E. G., Piai J. F., Schüquel I. T. A., Rubira A. F., Muniz E. C.: Functionalization of poly(vinyl alcohol) by addition of methacryloyl groups: Characterization by FTIR and NMR and optimization of reaction conditions by RSM. *e-Polymers*, no.62 (2006).
- [37] Peppas N. A., Merrill E. W.: Crosslinked poly(vinyl alcohol) hydrogels as swollen elastic networks. *Journal of Applied Polymer Science*, **21**, 1763–1770 (1977).
DOI: [10.1002/app.1977.070210704](https://doi.org/10.1002/app.1977.070210704)
- [38] Elias H. G.: *Macromolecules: Structure and properties*. Plenum Press, New York (1983).
- [39] Fajardo A. R., Piai J. F., Rubira A. F., Muniz E. C.: Time- and pH-dependent self-rearrangement of a swollen polymer network based on polyelectrolytes complexes of chitosan/chondroitin sulfate. *Carbohydrate Polymers*, **80**, 934–943 (2010).
DOI: [10.1016/j.carbpol.2010.01.009](https://doi.org/10.1016/j.carbpol.2010.01.009)
- [40] Ritger P. L., Peppas N. A.: A simple equation for description of solute release II. Fickian and anomalous release from swellable devices. *Journal of Controlled Release*, **5**, 37–42 (1987).
DOI: [10.1016/0168-3659\(87\)90035-6](https://doi.org/10.1016/0168-3659(87)90035-6)
- [41] Yoshinari E., Furukawa H., Horie K.: Fluorescence study on the mechanism of rapid shrinking of grafted poly(*N*-isopropylacrylamide) gels and semi-IPN gels. *Polymer*, **46**, 7741–7748 (2005).
DOI: [10.1016/j.polymer.2005.01.100](https://doi.org/10.1016/j.polymer.2005.01.100)
- [42] Moura M. R., Guilherme M. R., Campese G. M., Radovanovic E., Rubira A. F., Muniz E. C.: Porous alginate-Ca²⁺ hydrogels interpenetrated with PNIPAAm networks: Interrelationship between compressive stress and pore morphology. *European Polymer Journal*, **41**, 2845–2852 (2005).
DOI: [10.1016/j.eurpolymj.2005.06.007](https://doi.org/10.1016/j.eurpolymj.2005.06.007)
- [43] Li Y., Zhang L., Zuo Y., Yang W. H., Shen J., Li Y.: Poly(*N*-isopropyl acrylamide)/chitosan composite membrane with smart thermoresponsive performance. *Materials Research Innovations*, **14**, 252–257 (2010).
DOI: [10.1179/143307510X12719005364828](https://doi.org/10.1179/143307510X12719005364828)
- [44] You J-O., Auguste D. T.: Conductive, physiologically responsive hydrogels. *Langmuir*, **26**, 4607–4612 (2010).
DOI: [10.1021/la100294p](https://doi.org/10.1021/la100294p)
- [45] Barthus R. C., Lira L. M., de Torresi S. I. C.: Conducting polymer- hydrogel blends for electrochemically controlled drug release devices. *Journal of the Brazilian Chemical Society*, **19**, 630–636 (2008).
DOI: [10.1590/S0103-50532008000400004](https://doi.org/10.1590/S0103-50532008000400004)

Mechanical and thermal properties of crab chitin reinforced carboxylated SBR composites

P. M. Visakh¹, M. Monti², D. Puglia², M. Rallini², C. Santulli^{3*}, F. Sarasini³, S. Thomas¹, J. M. Kenny²

¹Centre for Nanoscience and Nanotechnology, Mahatma Gandhi University Kottayam, Kerala, India

²University of Perugia, UDR INSTM, Department of Civil and Environmental Engineering, Strada di Pentima 4, 05100 Terni, Italy

³Department of Chemical Engineering Materials Environment, Sapienza-Universita di Roma, Via Eudossiana 18, 00184 Roma, Italy

Received 18 September 2011; accepted in revised form 1 December 2011

Abstract. The addition of small amounts (up to 9 wt%) of chitin microsized particles, originating from shellfish waste, to carboxylated styrene-butadiene rubber (XSBR) matrix (as received and annealed to 100°C) has been studied. In particular, this study concentrated on their mechanical (creep investigation by nanoindentation and dynamical-mechanical analysis), thermal (differential scanning calorimetry and thermogravimetry) and swelling behaviour (toluene absorption) and was completed by morphological characterisation by scanning electron microscopy and atomic force microscopy.

The results show that annealing has a limited effect on materials properties, effects which are further reduced by the addition of growing amounts of crab chitin. It should be noted that the limited filler content used in the study does not substantially modify the linear creep behaviour of XSBR for sufficiently long loading times. The thermal stability of the system does also appear to be preserved even with the maximum chitin content added, while it serves sufficiently as an effective barrier against aromatic solvent absorption.

Keywords: rubber, nanoindentation, crab chitin, thermal properties, solvent absorption

1. Introduction

Chitin is a high molecular weight polymer, mainly with linear structure, based on a polysaccharide compound containing an acetamide group, specifically β -(1 to 4) (N-acetyl -D- glucosamine). It is widely present in plants and animals, being the second most abundant biopolymer in nature after cellulose and therefore biodegradable: in addition to being biodegradable, chitin is highly crystalline and depending on its origin it occurs in three forms identified as α , β , and χ chitin [1]. Other positive qualities include non-toxicity, non-allergenicity, anti-microbial effect, insolubility in water and resistance to acids, alkalis, and many organic solvents, ver-

satile biological activity and excellent biocompatibility [2]. The above characteristics make chitin suitable for applications in a number of areas other than food industry, such as e.g., in biosensors, and in medical and pharmaceutical applications as wound-dressing material and device for controlled drug release [3].

Chitin can easily be isolated from crab shell, when it is found to be highly thixotropic and liquid crystalline [4]. When isolating the crystalline regions of chitin, referred to as whiskers, from the crab shells and squid pens by hydrochloric acid hydrolysis, it was found that these microfibrillar arrangements have quite uniform properties [5]. In the specific

*Corresponding author, e-mail: carlo.santulli@uniroma1.it

case of chitin whiskers extracted from crab shells, the distribution in length has been found to range from 100 to 500 nm, while diameter was between 10 and 80 nm, which implied that the average aspect ratio (length/diameter), was 10 ± 5 [6].

The introduction of these natural polymers as nanofillers in a rubber matrix has been suggested, to improve specific properties in some applications. In particular, they are likely to reduce the amount of swelling due to absorption in membranes [7], and can allow SBR to compete with vulcanised rubber, in that their reinforcing capability, depending on the aspect ratio of the chitin, can be comparable to the traditional inorganic nanofillers e.g., clay [8]. In addition, the compatibilization efficiency of styrene-butadiene matrices generally depends on the conditions of blend preparation and processing [9]. In particular, thermal annealing of rubber blends results often in a substantial hardening of the material, which is capable of providing a stronger interface for the possible introduction of reinforcement in the rubbery matrix [10].

If suitable conditions for compatibility are achieved, the active surface of natural nanofillers facilitates chemical derivation and grafting, and forms strong physical interaction with polymer matrix. This was explained by the fact that the whiskers take the appearance of a rigid network, which results from strong interactions between them, in particular from hydrogen bonds: the network is possibly governed by a percolation mechanism only at high temperature [11]. Unmodified chitin whiskers, obtained from squid pen [12] and crab shells [5] have been tested as the reinforcing elements in polymer matrices, such as polycaprolactone [13], acrylic resins [14] and natural rubber [4–6]. Modification of chitin whiskers by different chemical agents, in particular succinic anhydride, and different types of isocyanates, has also been attempted, with no substantial improvement for the introduction into a natural rubber matrix [15]. It has been suggested that this loss of performance is due to the partial destruction of the aforementioned three-dimensional network of chitin whiskers assumed to be present in the unmodified composites [16].

This work concentrates on the study of the mechanical and thermal properties of composites with crab chitin introduced into an XSBR latex: a number of studies of these properties for the pure unvulcan-

ized matrix are available, in particular [9, 17–20]. This study does also include the degradation scenario of these composites, in particular measuring their dynamical properties, their creep profile, their temperature degradation and their swelling by toluene absorption.

2. Materials and methods

2.1. Materials

2.1.1. Base materials

The XSBR latex used in this study was supplied by Apar Industries Ltd., Bombay, Maharashtra, India. Table 1 reports the most important features of this latex. α -Chitin powder was supplied by Marine Chemicals, Cochin, Kerala, India. All the chemical products needed for the chitin treatments, namely 3N-hydrochloric acid (HCl), potassium hydroxide (KOH – 5% solution), sodium hypochlorite (NaClO₂) (solution for bleaching) and 3N-sodium acetate buffer, were purchased by Indian chemical suppliers. In order to obtain nano-sized chitin whiskers, a process consisting in several steps was carried out.

Table 1. Properties of carboxylated styrene butadiene rubber latex

Dry rubber content (DRC)	47%
Total solid content (TSC)	50.7%
Styrene content	59%
pH	8.60
Mechanical stability	Good

2.1.2. Chitin deproteinisation

The first part of the process consists in the deproteinisation of the chitin. Firstly, the chitin powder was stirred and boiled with 5 wt% aqueous KOH solution for 6 h. Then it was rinsed with distilled water and filtered. Lamarque *et al.* [21] reported that the sodium hydroxide concentration influences the nanostructure of chitin whiskers. After this treatment, chitin was bleached with 17 g of NaClO₂ in 1 L of distilled water mixed with 27 g of NaOH in 75 mL of acetic acid completed with 925 mL of distilled water. The suspension was stirred at 80°C for 2 h. This procedure was repeated three times.

2.1.3. Preparation of nanochitin whiskers

The chitin whisker suspensions were prepared by hydrolyzing the purified chitin with 3N HCl at the boiling point for 1.5 h while stirred. After acid

hydrolysis the suspensions were dialyzed for 2 h in distilled water and then overnight in running water. An additional dialysis by dialysis bag for 12 h by changing the distilled water every 2 h was performed until a pH = 6 was reached. The dispersion of whiskers was completed by three successive ultrasonic treatments for 2 minutes each. The concentration of the chitin particles suspension was 2.88 g over the 40 mL batches, which means 7.2 wt%, then it was progressively diluted to obtain the other concentrations.

2.1.4. Preparation of composites

In order to obtain the blends, the XSBR latex and the chitin suspension were mixed together and stirred for 2 hours, then cast in Petri dishes. The solid nanocomposite films were obtained drying the solution in an oven at 40°C, allowing the water to evaporate.

In all the prepared composites, the XSBR latex volume fraction was kept constant, whereas the volume fraction of chitin whiskers suspension was tuned from 30 to 70 vol%, which correspond to a weight between 2.16 and 5.04 grams of chitin in 100 mL total XSBR latex. Throughout the present paper, the compositions of the composites are expressed in terms of volume percentages, for convenience. The pure XSBR matrix is also prepared and used as the control. To observe the effect of an annealing treatment on the produced materials, the neat XSBR and all the nanocomposite blends were heated to 100°C for 90 minutes, then tested and compared with the non-annealed ('as received') materials. This procedure has the aim of showing the effect of exposure to a temperature slightly exceeding the maximum service temperature, in particular showing the effect of high temperature washing (vapour vacuum cleaning) on the material, thinking of the below mentioned application of it in the textile field.

The annealing treatment can be supposed to yield an accelerated drying of the composites, also from

water collected by chitin, given that lower temperatures, usually 40 or 60°C, have been applied for that purpose in literature [22–23] and also harden the rubber matrix by removing the water content of the latex. Heating at this temperature is also likely to promote filler flocculation, as proposed in [24], to modify their geometry and evaluate the effect of this treatment on the mechanical properties. The flocculation effect for the filler has been revealed for equivalent systems in [9], demonstrating that even the addition of a few weight percent of synthesized clays, up to 2.5% of unmodified fluorohectorite, produces a slight but perceivable decrease of the viscosity.

Table 2 summarized all the studied materials with their composition.

2.2. Methods

2.2.1. DMA analysis

Dynamical mechanical analysis has been often performed on filled systems based on including unvulcanised rubber to determine the viscoelastic properties of the system [5, 17, 25, 26]. In this work, DMA was performed by using a Rheometric Scientific (Piscataway, NJ, USA) -ARES N2 rheometer. The sample size was 10 mm in width, 30 mm in length, and about 1.5 mm in thickness. The measurements were carried out in the dynamic time sweep test starting from $T = -40$ up to 80°C (heating rate = 5°C/min) and frequency fixed at 1 Hz and shear strain at 0.15%. The storage modulus, loss modulus and loss factor ($\tan\delta$) of the samples were measured.

2.2.2. SEM analysis

An assessment on the morphological aspects of the produced material was carried out with a field emission scanning electron microscope (FESEM) ZEISS (Carl Zeiss s.p.a., Arese, Italy) model Supra 25.

2.2.3. AFM examination

The chitin whiskers, as well as the nanocomposites, were also characterized using a Veeco (Plainview,

Table 2. Composition of the different samples used

XSBR latex [mL]	Chitin solution [mL]	Chitin content [g]	Chitin wt%	Samples
100	0	0	0	XSBR, XSBR-A
100	30	2.16	4.1	CW30, CW30-A
100	50	3.60	6.6	CW50, CW50-A
100	70	5.04	9.0	CW70, CW70-A

Samples marked with A have been annealed at 100°C

NY, USA) MultiMode scanning probe microscope with a Nanoscope V controller. For the analysis of chitin, a droplet of the aqueous whisker suspension (0.5% by weight) was dried on a mica surface prior to AFM examination. The nanocomposite films were microtomed using a diamond knife after embedding in epoxy resin and were analyzed directly. The images for the whiskers and the nanocomposites were collected using a tapping mode etched silicon tip, with a nominal spring constant of 5 N/m and a nominal frequency of 270 kHz.

2.2.4. Thermogravimetric analysis (TGA)

The thermal stability of the produced materials was investigated by means of thermogravimetric analysis (TGA). The measurements were performed with a thermogravimetric analyzer Seiko (Seiko Instruments, Inc., Chiba, Japan) model Exstar 6300 in nitrogen atmosphere, and consisted in dynamic scans at the heating rate of 20°C/min from 30 to 900°C. Bulk samples of about (10±1) mg were tested.

2.2.5. Differential scanning calorimetry (DSC)

Differential scanning calorimetry was performed using a differential scanning calorimeter MDSC TA (TA Instruments, Vimodrone, Italy) model Q200. The temperature range analyzed was –90 to 200°C.

2.2.6. Swelling experiments

Toluene absorption tests on as-received and annealed samples have also been carried out, with the idea of considering the durability of the matrix and its envisaged application, which was discussed above.

The kinetics of toluene absorption was determined for XSBR based composites. The specimens used were square shaped samples with 2 mm side and around 1–1.5 mm thick. The thickness, $2L$, of the film was therefore supposed to be thin enough so that the molecular diffusion was considered to be one-dimensional. After weighing, the samples were immersed in toluene. The samples were removed at specific intervals (t) and weighed (M_t) up to an equilibrium value (M_∞). The swelling rate of the samples was calculated by dividing the gain in weight ($M_t - M_0$) by the initial weight (M_0). Since these swelling experiments were more difficult to perform for unvulcanized materials (part of the sample could dissolve in toluene), the following analysis was also performed for these samples. Thin square shaped samples were first weighed (M_0) and then immersed in toluene for 48 h. They were subsequently dried for 12 h at 55–60°C and weighed again (M_0'). The 'sol' fraction (M_0'/M_0) and relative weight loss (RWL) $[M_0 - M_0']/M_0$ were then determined. This allowed estimating the fraction of XSBR bonded to the filler and the fraction of XSBR dissolved in toluene.

2.2.7. Nanoindentation creep testing

A NanoTest nanoindenter, supplied by MicroMaterials Inc. (Tampa, FL, USA), was employed to study the creep behaviour of the produced materials. This equipment consists of a pendulum-based depth sensing system, with the sample vertically mounted. A Berkovich-type three-sided pyramidal indenter was used. The indentation was load-controlled to 0.05 mN maximum load for 200 s as the holding period. All

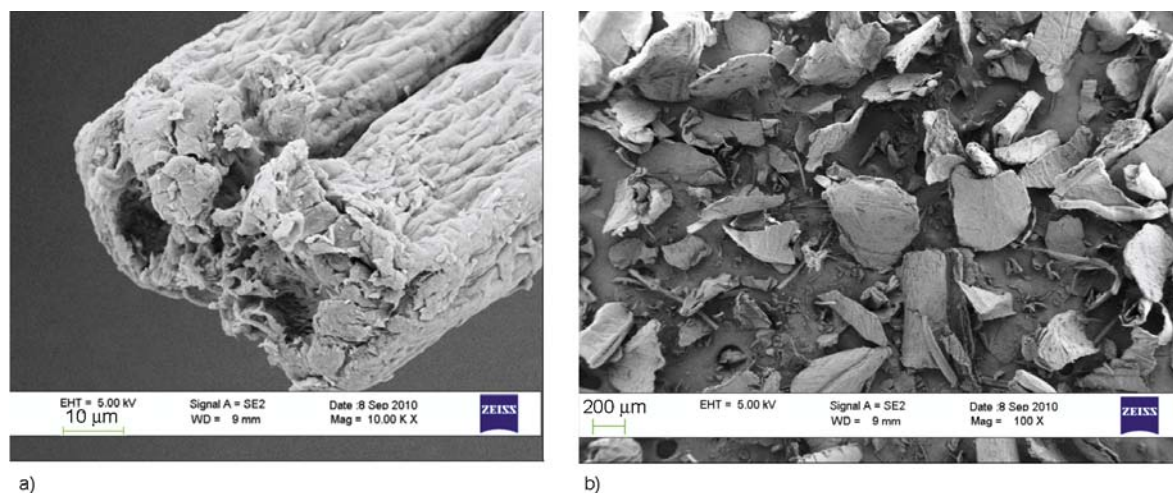


Figure 1. (a) Tip of a chitin whisker, (b) general appearance of chitin powder

the tests were performed at 23°C. Twenty tests were performed on each sample, in order to obtain a good reliability of the results.

3. Results

Commercial chitin from crab shells consists of a mixture of roughly spherical particles with diameter around 0.5–1 mm and ill-defined particles [4]. The treatment followed generated intertwined and spiralling chitin microfibrils, forming whiskers such as the one whose tip is reproduced in Figure 1a. However, the general appearance of chitin powder still includes a wide variability of particle geometries and sizes, as illustrated in Figure 1b.

The discussion of results obtained focused on the two effects of the addition of an increased quantity of crab chitin in the matrix and of XSBR rubber annealing. Crab chitin addition allowed using a waste product originating from seafood industries, while the matrix was annealed to prepare it to the envisaged use of XSBR as back coating for textiles and carpets, for which application an increased resistance to wear and to degradation due e.g., to solvent absorption, is desirable. Previous studies suggested that the addition of limited amounts of chitosan to natural rubber latex decreases benzene diffusivity, an effect which is likely to be observed also in this case for small amounts of chitin [24].

The four-element Burgers model has been used to approximate the creep behaviour in solid-filled rubber [27] and more recently also in natural fibre reinforced polymers [28, 29]. This model is commonly represented by the simultaneous presence of two

Table 3. Constants obtained from the creep model

Samples	K_1 [N/m]	K_2 [N/m]	η_1 [N·s/m]	η_2 [N·s/m]
XSBR	48.664	80.901	1279.90	23 104
XSBR-A	38.028	64.658	925.33	16 152
CW30	40.979	65.195	773.15	20 113
CW30-A	31.537	70.305	1154.00	22 019
CW50	31.279	60.763	985.45	19 678
CW50-A	53.239	103.150	1535.60	24 940
CW70	35.733	58.925	857.38	16 083
CW70-A	78.949	188.090	1981.00	41 791

elastic constants (springs): elastic recovery (K_1) and rubbery elasticity (K_2), and two viscous constants (dashpots): molecular ‘slip’ (η_1) and delayed elasticity (η_2). Respective values are reported in Table 3.

The model appears to closely match the experimental results of creep tests by nano-indentation (Figure 2), giving a representation as the function $H(t) = A \cdot \ln(B \cdot t + 1)$. Comparing the creep results between the as-received and annealed samples, annealing results in a highly increased resistance to indentation for the samples with higher chitin content (CW50 and CW70), an effect which is not observed for the pure XSBR and the CW30 sample. This is a perceivable trend, although the bulk values provided by nanoindentation are not directly comparable with the calculation of elastic modulus. This is due to the fact that it provides information on hardness and surface profile of modulus, surface-based information whose application to the material in general can be affected by the non uniformity of the matrix and further aggravated by the presence of the filler. As a general point, it can be suggested that filler flocculation is amongst the

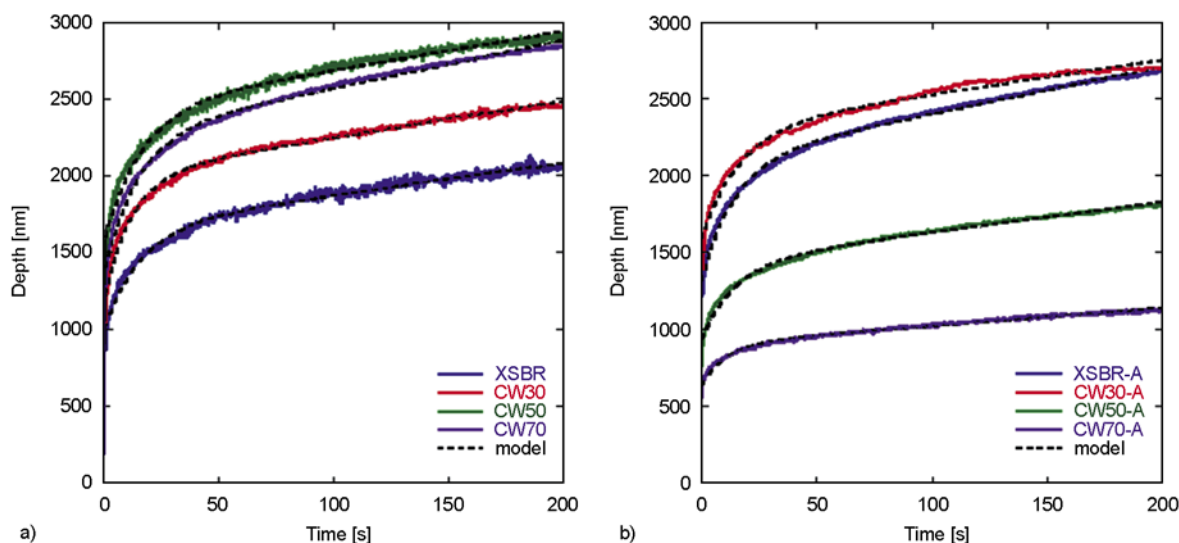


Figure 2. Nano-indentation curves for normal (a) and annealed samples (b)

Table 4. Comparison of the rigidity of normal and annealed samples

Compared samples	Depth difference after			
	50 s [nm]	100 s [nm]	150 s [nm]	200 s [nm]
XSBR-A vs. XSBR	580	650	630	640
CW30-A vs. CW30	270	250	320	230
CW50-A vs. CW50	-980	-1100	-1120	-1080
CW70-A vs. CW70	-1450	-1480	-1690	-1770

Table 5. DMA variables for the different samples

Material	T_{peak} [°C]	$\tan \delta$	$\Delta T_{0.5\text{peak}}$ [°C]
XSBR	-6.32	1.15	17.48
XSBR-30CW	-5.63	0.78	25.07
XSBR-50CW	-9.26	0.81	19.54
XSBR-70CW	-7.96	0.97	18.44
XSBR-A	-8.26	1.20	16.24
XSBR-30CWA	-7.57	0.95	19.09
XSBR-50CWA	-9.07	1.08	17.81
XSBR-70CWA	-8.21	0.78	20.45

Table 6. Storage and loss moduli for the different samples at 25°C

Material	G' [Pa] at 25°C	G'' [Pa] at 25°C
XSBR	$1.3905 \cdot 10^6$	$1.8260 \cdot 10^5$
XSBR-A	$1.4405 \cdot 10^6$	$1.4695 \cdot 10^5$
XSBR-CW30	$3.9459 \cdot 10^6$	$1.0366 \cdot 10^6$
XSBR-CW30A	$3.9459 \cdot 10^6$	$7.0493 \cdot 10^5$
XSBR-CW50	$8.8983 \cdot 10^6$	$3.0748 \cdot 10^6$
XSBR-CW50A	$6.2482 \cdot 10^6$	$1.1311 \cdot 10^6$
XSBR-CW70	$1.7701 \cdot 10^7$	$1.6984 \cdot 10^6$
XSBR-CW70A	$2.5251 \cdot 10^7$	$3.9928 \cdot 10^6$

Table 7. Values of glass transition temperature for the different samples

Material	T_g [°C] of XSBR from DSC analysis
XSBR	10.0
XSBR_A	13.8
CW30	14.2
CW30_A	13.3
CW50	12.2
CW50_A	14.6
CW70	16.0
CW70_A	16.7

causes of increased resistance to indentation provided by the annealed, therefore temperature-aged, samples [30].

By subtracting the depth of nano-indentation at times between 50 and 200 seconds between the as-received and the corresponding annealed sample,

the results reported in Table 4 are obtained, which further clarify the trend observed above. In particular, the rubber matrix does not appear to depart from linearity for high times of loading, as it would have probably be the case for higher filler contents [31]. In addition, annealing at temperatures exceeding the XSBR critical temperature (glass transition of the styrene phase) does result in an easier cracking of the matrix after annealing (Figure 3), an effect which appears mitigated nevertheless by the introduction of progressively growing amounts of crab chitin.

The DMA results (reported in Figure 4 and Table 5) confirm that, as expected, the increasing content of filler in the polymeric matrix has the effect of rising the G' modulus in the entire temperature range. The $\tan \delta$ values for the different systems are almost the same, confirming the calorimetric observations. The amplitude in terms of ΔT of the $\tan \delta$ peak at the half of the maximum value, indicated as $\Delta T_{0.5}$ (reported in the last column of Table 5) slightly grows, even with the introduction of the lowest quantity of chitin.

The annealing treatment has a weak effect on the loss modulus profile, in the sense that only a small increase of the G'' values is obtained in the entire temperature range due to the resulting stiffening. For comparison, the storage and loss modulus values measured at $T = 25^\circ\text{C}$ are reported in Table 6.

DSC results, reported in Table 7, demonstrate that glass transition temperature T_g has a slight growth with increasing chitin content, and some less perceivable increase is also observed as an effect of annealing, which was justified by matrix stiffening. The calorimetric results suggest that the annealing at 100°C maintained for 90 minutes does only slightly modify the mobility of the polymer chains, even in presence of chitin nanoparticles.

TGA and DTG measurements (Figures 5 and 6) demonstrate that chitin addition does not substantially change the thermal stability of XSBR matrix: in other words, the annealing process does not have a large influence on the maximum weight loss rate. The presence of the degradation peak of the chitin is visible in the DTG profile as a shoulder of the main peak at $360\text{--}375^\circ\text{C}$ (depending on the filler content), while the peak due to the matrix degradation remains virtually unchanged. These results confirmed that the thermal stability of the system is

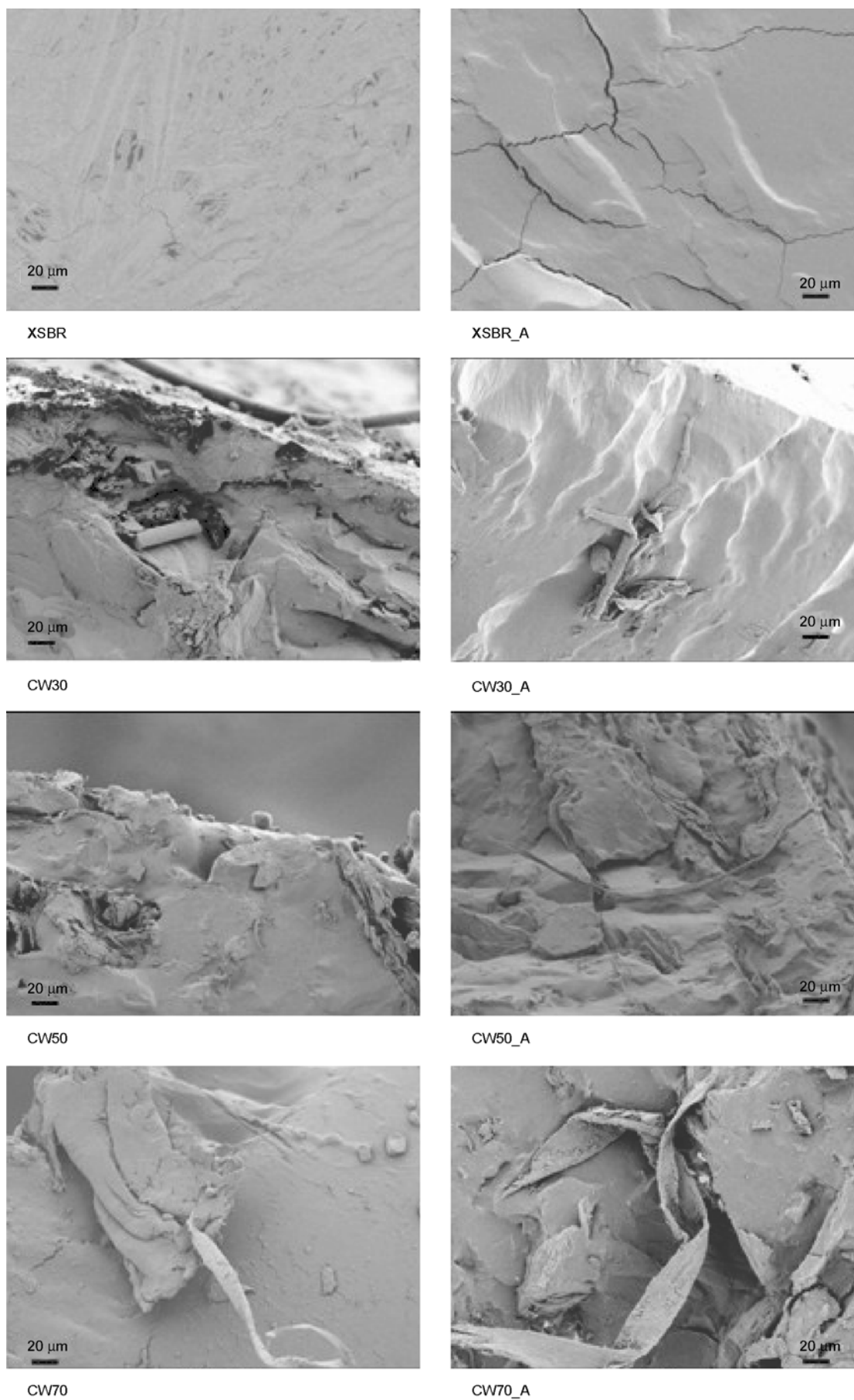


Figure 3. Comparison between as received (left) and annealed (right) SBR nanocomposites

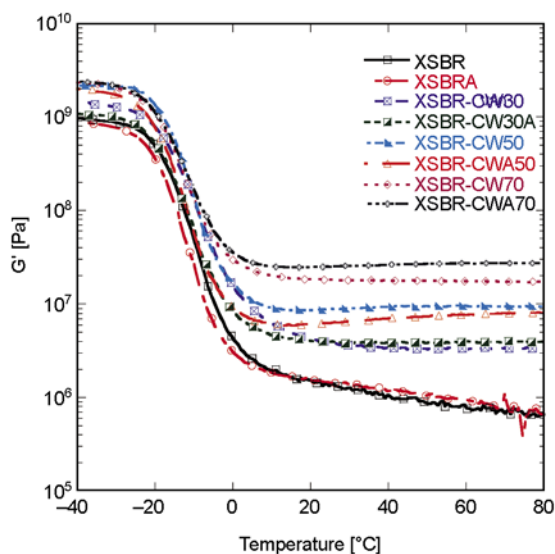


Figure 4. Storage modulus of the different samples

preserved, also with variable amounts of natural filler with thermally unstable behaviour. This can be considered as a positive outcome, since it demonstrated that the introduction of a natural filler, which is inherently thermally unstable, does not cause at these concentrations any change in the thermal stability of XSBR rubber.

Toluene absorption tests on as-received and annealed samples have also been carried out, with the idea of considering the durability of the matrix and its final application, which was discussed above. The selection of the solvent was done considering the matrix and its final application, not the filler. The sorption tests (Figure 7) demonstrate that the maximum weight gain is obtained for the unfilled XSBR matrix, while the decreasing slope in the curve

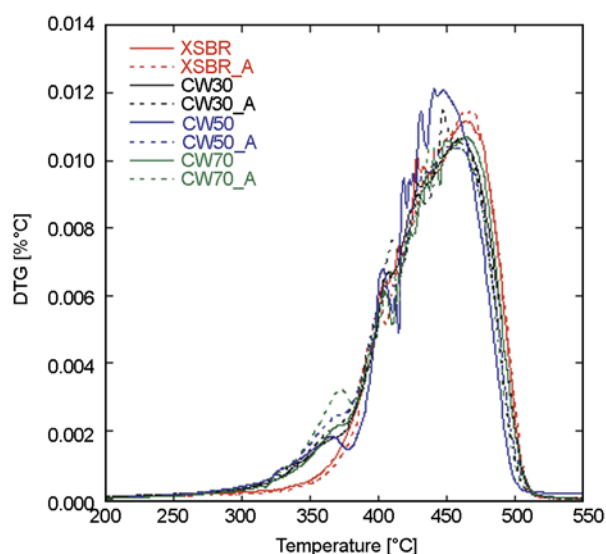


Figure 6. DTG of as-received and annealed samples

(weight gain vs time^{1/2}) is an indication of the effectiveness of the chitin as a barrier to the solvent uptake. In general, it has been shown already as XSBR samples filled with clay or silica micron-sized fillers showed reduced swelling rate owing to the tortuosity of the path [32].

The same result can be observed in experiment limited at 48 hours, point at which the systems start to lose their shape and going into solution due to the unvulcanized state of the rubber: the scattering of the different curves in Figure 7a is due to this condition. In particular, toluene absorption is decreased with growing chitin content in rubber. The larger effect is observed for the addition of the first 30%. The effect of annealing on this property appears to be not very consistent, apart from 70% samples,

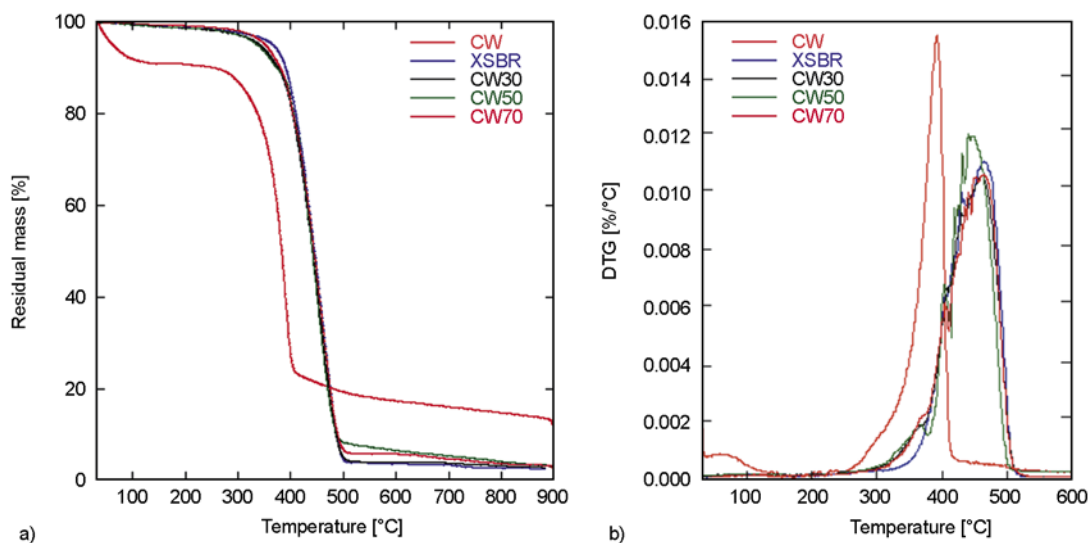


Figure 5. TGA and DTG results of as-received samples, compared with results from pure chitin (CW)

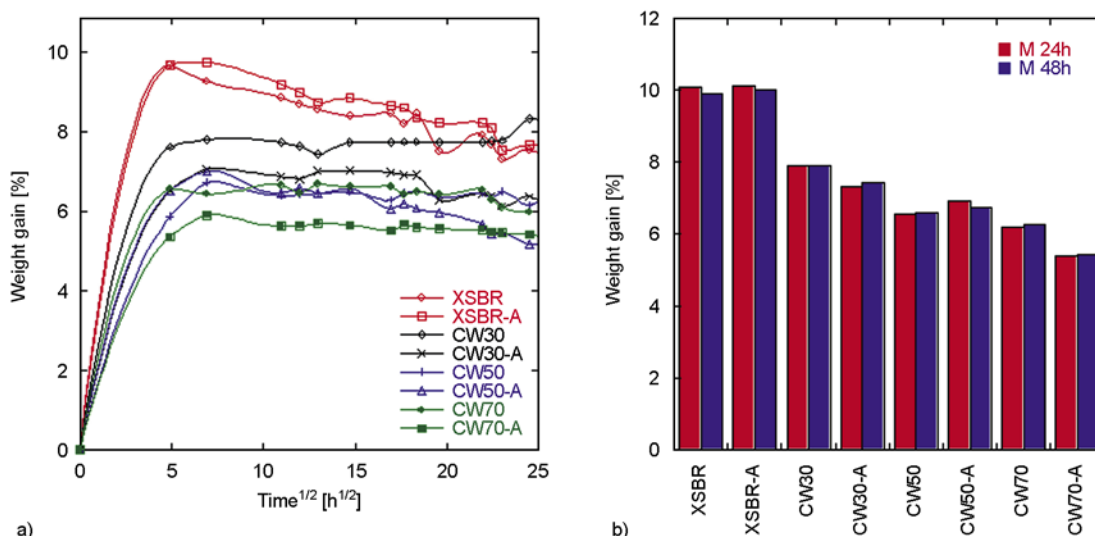


Figure 7. Weight gain during toluene absorption for 600 hours (a) and details of the comparison of 24 and 48 hours (b)

















Measurement time	M0	M48	Measurement time	M0	M48
XSBR57			XSBR_A		
CW30			CW30_A		
CW50			CW50_A		
CW70			CW70_A		

Figure 8. Aspect of samples before and after toluene absorption for 48 hours

where it may be due to reduced mobility of chitin filler, which does not allow allocating more solvent in the material. It is also noteworthy that the annealing does not ease geometry preservation during degradation due to toluene absorption (Figure 8). The morphological investigation of the samples by SEM (Figures 9 and 10) highlighted that the solvent absorption gives rise to an exfoliation of the rubber matrix, showing the weak interface between the XSBR and aggregates of chitin nanowhiskers, which have micrometric dimensions. This effect is not substantially worsened by the annealing treat-

ment (Figure 10), a finding that suggests once again that exposure to 100°C temperature for limited amounts of time does not significantly modify the properties of the material.

The observation of the chitin powder with the nanowhiskers was possible under AFM: this showed clearly the typical needle-like structure of the whiskers (Figure 11a) [33], while these are disposed non uniformly across the matrix (Figure 11b), a finding which may explain the aforementioned interface issues.

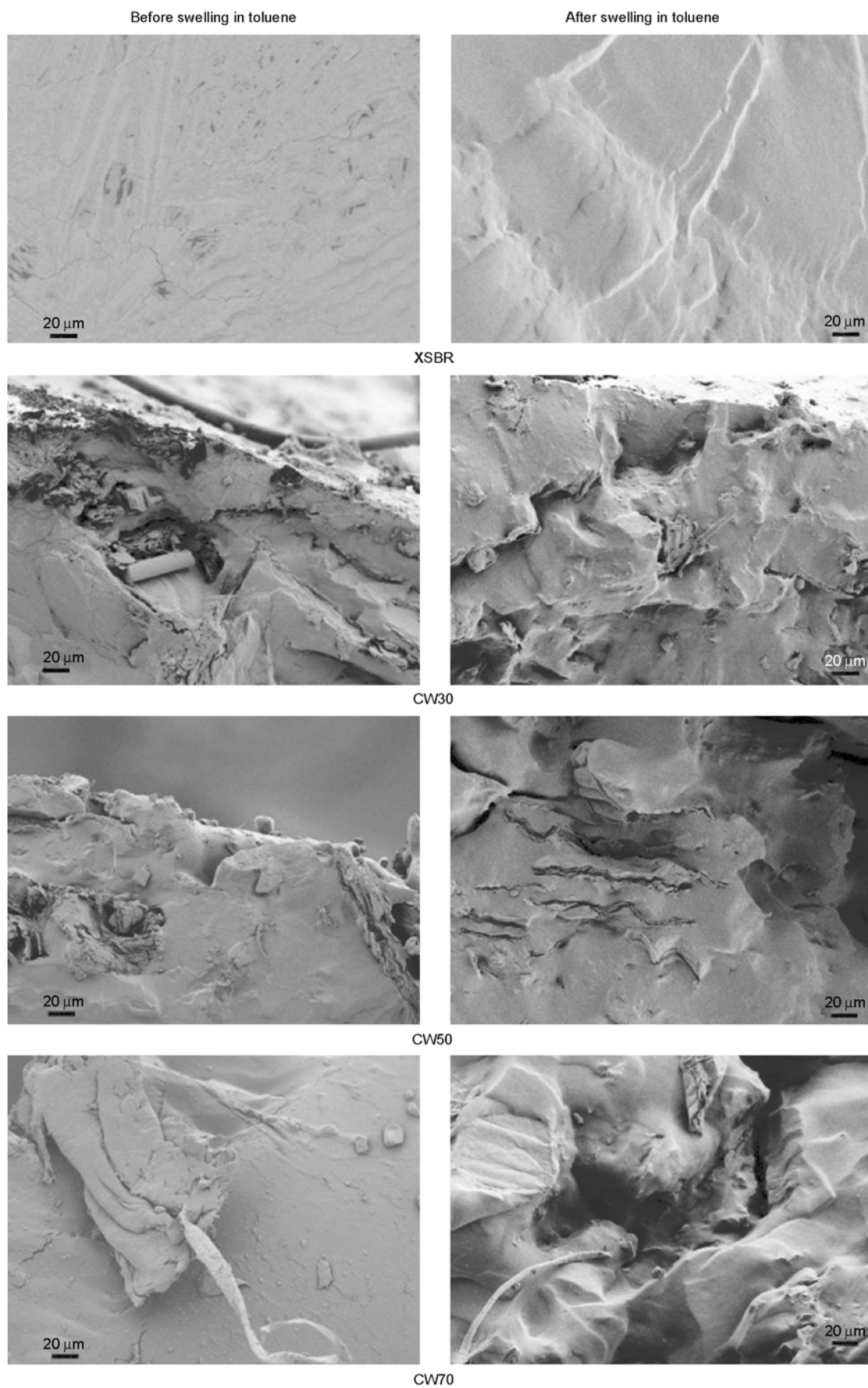


Figure 9. SEM micrographs of samples as received before and after toluene absorption for 48 hours

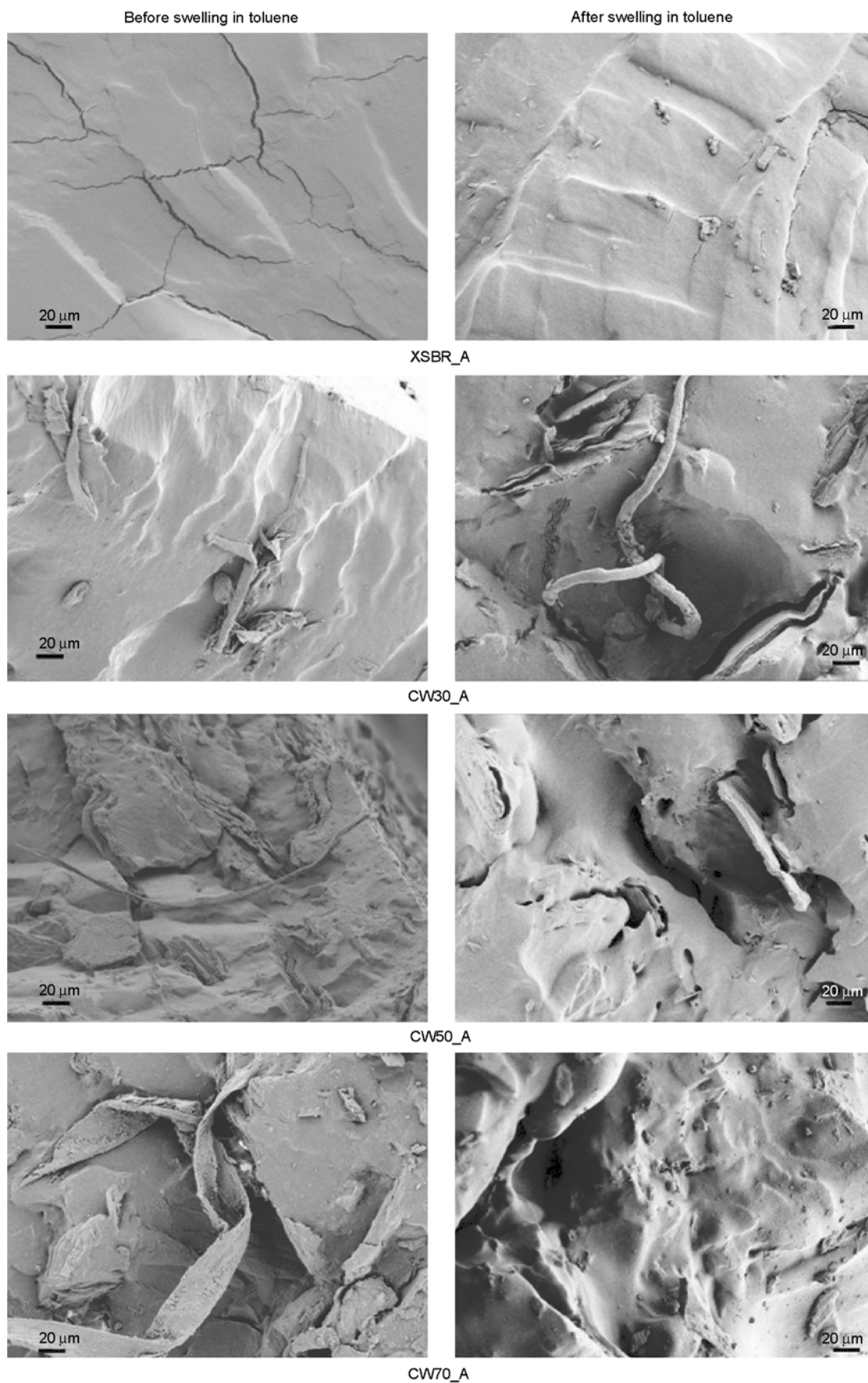


Figure 10. SEM micrographs of annealed samples before and after toluene absorption for 48 hours

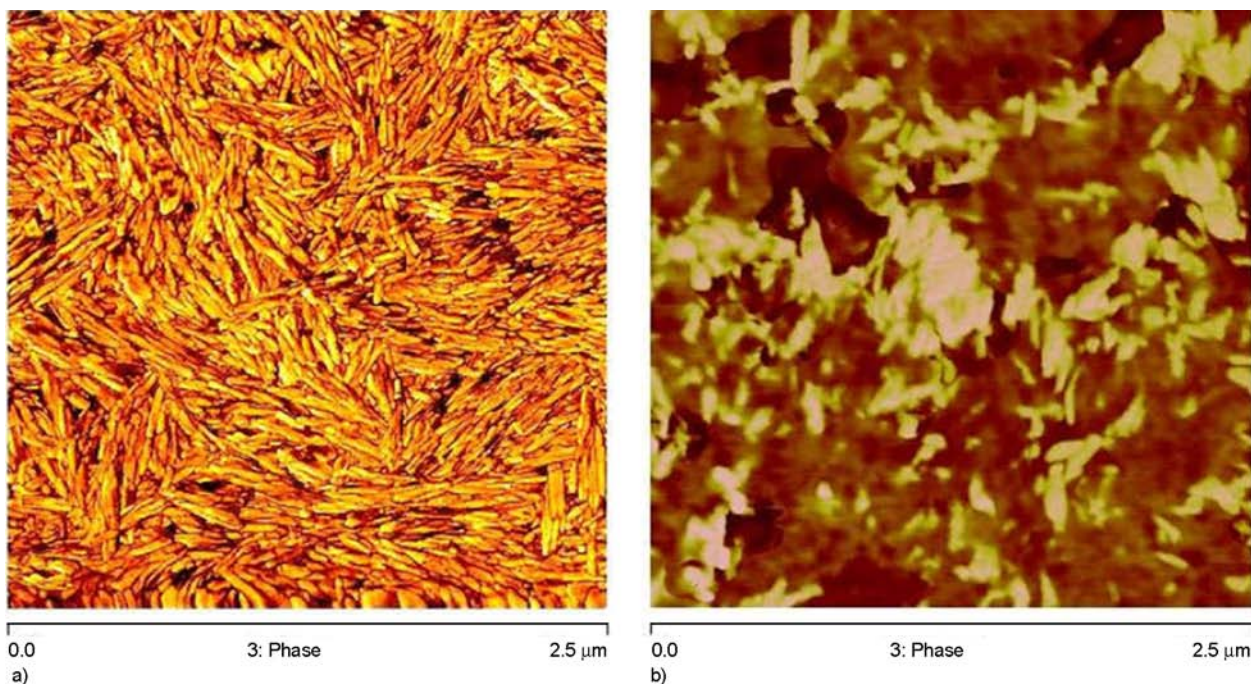


Figure 11. AFM imaging of: (a) a dilute suspension of nanochitin whiskers and (b) XSBR-CW50 (6.6 wt% chitin whisker nanocomposites)

4. Conclusions

This investigation was mainly aimed at evaluating the effect of the addition of small quantities of crab chitin from shellfish waste on the thermal, mechanical and morphological properties and swelling behaviour under toluene absorption of carboxylated styrene-butadiene rubber. A subsequent objective was also measuring the variation of the above properties as a consequence of annealing to 100°C, to give indication of the system resistance to service in the envisaged application (back coating for textiles and carpets).

The results show that crab chitin, also in very low amounts, offers some solvent barrier effect, while on the other side it does not substantially affect the thermal stability and the creep properties of the matrix. In addition, the system does not appear to be substantially modified by the exposure at high temperature for limited amounts of time, compatible with service needs (annealing was applied for 90 minutes).

This study can be suggestive for the investigation of the effect of introduction of different microsized fillers, originating from waste products, in this rubber matrix or in other similar blends.

References

- [1] Dufresne A.: Natural rubber green nanocomposites. in 'Rubber nanocomposites: Preparation, properties, and applications' (eds.: Thomas S., Stephen R.) Wiley, Singapore, 113–146 (2010). DOI: [10.1002/9780470823477.ch5](https://doi.org/10.1002/9780470823477.ch5)
- [2] Wang Z., Hu Q., Cai L.: Chitin fiber and chitosan 3D composite rods. *International Journal of Polymer Science*, **2010**, 369759/1–369759/7 (2010). DOI: [10.1155/2010/369759](https://doi.org/10.1155/2010/369759)
- [3] Chen L., Du Y., Wu H., Xiao L.: Relationship between molecular structure and moisture-retention ability of carboxymethyl chitin and chitosan. *Journal of Applied Polymer Science*, **83**, 1233–1241 (2002). DOI: [10.1002/app.2290](https://doi.org/10.1002/app.2290)
- [4] Nair K. G., Dufresne A.: Crab shell chitin whisker reinforced natural rubber nanocomposites. 1. Processing and swelling behavior. *Biomacromolecules*, **4**, 657–665 (2003). DOI: [10.1021/bm020127b](https://doi.org/10.1021/bm020127b)
- [5] Nair K. G., Dufresne A.: Crab shell chitin whisker reinforced natural rubber nanocomposites. 2. Mechanical behavior. *Biomacromolecules*, **4**, 666–674 (2003). DOI: [10.1021/bm0201284](https://doi.org/10.1021/bm0201284)
- [6] Visakh P. M., Thomas S.: Preparation of bionanomaterials and their polymer nanocomposites from waste and biomass. *Waste and Biomass Valorisation*, **1**, 121–134 (2010). DOI: [10.1007/s12649-010-9009-7](https://doi.org/10.1007/s12649-010-9009-7)

- [7] Stephen R., Varghese S., Joseph K., Oommen Z., Thomas S.: Diffusion and transport through nanocomposites of natural rubber (NR), carboxylated styrene butadiene rubber (XSBR) and their blends. *Journal of Membrane Science*, **282**, 162–170 (2006). DOI: [10.1016/j.memsci.2006.05.019](https://doi.org/10.1016/j.memsci.2006.05.019)
- [8] Shams M. I., Ifuku S., Nogi M., Oku T., Yano H.: Fabrication of optically transparent chitin nanocomposites. *Applied Physics A: Materials Science and Processing*, **102**, 325–331 (2010). DOI: [10.1007/s00339-010-5969-5](https://doi.org/10.1007/s00339-010-5969-5)
- [9] Stephen R., Alex R., Cherian T., Varghese S., Joseph K., Thomas S.: Rheological behavior of nanocomposites of natural rubber and carboxylated styrene butadiene rubber latices and their blends. *Journal of Applied Polymer Science*, **101**, 2355–2362 (2006). DOI: [10.1002/app.23852](https://doi.org/10.1002/app.23852)
- [10] Soares B. G., Cario F. O. Jr.: Reactive compatibilization of polystyrene/poly(ethylene-co-vinyl acetate) (EVA) blends. *Journal of Applied Polymer Science*, **99**, 14–22 (2006). DOI: [10.1002/app.21856](https://doi.org/10.1002/app.21856)
- [11] Junkasem J., Rujiravanit R., Grady B. P., Supaphola P.: X-ray diffraction and dynamic mechanical analyses of α -chitin whisker-reinforced poly(vinyl alcohol) nanocomposite nanofibers. *Polymer International*, **59**, 85–91 (2010). DOI: [10.1002/pi.2693](https://doi.org/10.1002/pi.2693)
- [12] Paillet M., Dufresne A.: Chitin whisker reinforced thermoplastic nanocomposites. *Macromolecules*, **34**, 6527–6530 (2001). DOI: [10.1021/ma002049v](https://doi.org/10.1021/ma002049v)
- [13] Feng L., Zhou Z., Dufresne A., Huang J., Wei M., An L.: Structure and properties of new thermoforming bionanocomposites based on chitin whisker-graft-polycaprolactone. *Journal of Applied Polymer Science*, **112**, 2830–2837 (2009). DOI: [10.1002/app.29731](https://doi.org/10.1002/app.29731)
- [14] Shams M. I., Ifuku S., Nogi M., Oku T., Yano H.: Fabrication of optically transparent chitin nanocomposites. *Applied Physics A: Materials Science and Processing*, **102**, 325–331 (2010). DOI: [10.1007/s00339-010-5969-5](https://doi.org/10.1007/s00339-010-5969-5)
- [15] Nair K. G., Dufresne A.: Crab shell chitin whiskers reinforced natural rubber nanocomposites. 3. Effect of chemical modification of chitin whiskers. *Biomacromolecules*, **4**, 1835–1842 (2003). DOI: [10.1021/bm030058g](https://doi.org/10.1021/bm030058g)
- [16] Dufresne A.: Processing of polymer nanocomposites reinforced with polysaccharide nanocrystals. *Molecules*, **15**, 4111–4128 (2010). DOI: [10.3390/molecules15064111](https://doi.org/10.3390/molecules15064111)
- [17] Stephen R., Thomas S., Raju K. V. S. N., Varghese S., Joseph K., Oommen Z.: Dynamic mechanical and dielectric properties of nanocomposites of natural rubber (NR), carboxylated styrene butadiene rubber (XSBR) latices and their blends. *Rubber Chemistry and Technology*, **80**, 672–689 (2007). DOI: [10.5254/1.3548187](https://doi.org/10.5254/1.3548187)
- [18] Stephen R., Siddique A. M., Singh F., Kailas L., Jose S., Joseph K., Thomas S.: Thermal degradation and ageing behavior of microcomposites of natural rubber, carboxylated styrene butadiene rubber latices, and their blends. *Journal of Applied Polymer Science*, **105**, 341–351 (2007). DOI: [10.1002/app.26042](https://doi.org/10.1002/app.26042)
- [19] Stephen R., Raju K. V. S. N., Rao M., Francis B., Joseph K., Thomas S.: Flow properties of unvulcanised natural rubber/carboxylated styrene butadiene rubber latices and their blends. *Journal of Applied Polymer Science*, **104**, 2528–2535 (2006). DOI: [10.1002/app.25855](https://doi.org/10.1002/app.25855)
- [20] Stephen R., Jose S., Joseph K., Thomas S., Oommen Z.: Thermal stability and ageing properties of sulphur and gamma radiation vulcanized natural rubber (NR) and carboxylated styrene butadiene rubber (XSBR) latices and their blends. *Polymer Degradation and Stability*, **91**, 1717–1725 (2006). DOI: [10.1016/j.polymdegradstab.2005.12.001](https://doi.org/10.1016/j.polymdegradstab.2005.12.001)
- [21] Lamarque G., Chaussard G., Domard A.: Thermodynamic aspects of the heterogeneous deacetylation of β -chitin: Reaction mechanisms. *Biomacromolecules*, **8**, 1942–1950 (2007). DOI: [10.1021/bm070021m](https://doi.org/10.1021/bm070021m)
- [22] Tomihata K., Ikada Y.: *In vitro* and *in vivo* degradation of films of chitin and its deacetylated derivatives. *Biomaterials*, **18**, 567–575 (1997). DOI: [10.1016/S0142-9612\(96\)00167-6](https://doi.org/10.1016/S0142-9612(96)00167-6)
- [23] Jang M-K., Kong B-G., Jeong Y-I., Lee C. H., Nah J-W.: Physicochemical characterization of α -chitin, β -chitin, and γ -chitin separated from natural resources. *Journal of Polymer Science Part A: Polymer Chemistry*, **42**, 3423–3432 (2004). DOI: [10.1002/pola.20176](https://doi.org/10.1002/pola.20176)
- [24] Johns J., Rao V.: Mechanical properties and swelling behavior of cross-linked natural rubber/chitosan blends. *International Journal of Polymer Analysis and Characterization*, **14**, 508–526 (2009). DOI: [10.1080/10236660903072797](https://doi.org/10.1080/10236660903072797)
- [25] Stephen R., Raju K. V. S. N., Nair S. V., Varghese S., Oommen Z., Thomas S.: Mechanical and viscoelastic behavior of natural rubber and carboxylated styrene-butadiene rubber latex blends. *Journal of Applied Polymer Science*, **88**, 2639–2648 (2003). DOI: [10.1002/app.12012](https://doi.org/10.1002/app.12012)

- [26] Chuayjuljit S., Luecha W.: XSBR/NR rubber blends filled with polystyrene-encapsulated nanosilica prepared by *in situ* differential microemulsion polymerization. *Journal of Elastomers and Plastics*, **43**, 407–427 (2011).
DOI: [10.1177/0095244311405001](https://doi.org/10.1177/0095244311405001)
- [27] Chen C-H., Chen Y-C.: The creep behavior of solid-filled rubber composites. *Journal of Polymer Research*, **1**, 75–83 (1994).
DOI: [10.1007/BF01378597](https://doi.org/10.1007/BF01378597)
- [28] Marcovich N. E., Villar M. A.: Thermal and mechanical characterization of linear low-density polyethylene/wood flour composites. *Journal of Applied Polymer Science*, **90**, 2775–2784 (2003).
DOI: [10.1002/app.12934](https://doi.org/10.1002/app.12934)
- [29] Nuñez A. J., Marcovich N. E., Aranguren M. I.: Analysis of the creep behavior of polypropylene-woodflour composites. *Polymer Engineering and Science*, **44**, 1594–1603 (2004).
DOI: [10.1002/pen.20157](https://doi.org/10.1002/pen.20157)
- [30] Bielinski D. M.: Application of microindentation to study ageing of rubber. *Kautschuk und Gummi Kunststoffe*, **62**, 50–54 (2009).
- [31] Bohm G. A., Tomaszewski W., Cole W., Hogan T.: Furthering the understanding of the non linear response of filler reinforced elastomers. *Polymer*, **51**, 2057–2068 (2010).
DOI: [10.1016/j.polymer.2010.01.047](https://doi.org/10.1016/j.polymer.2010.01.047)
- [32] Stephen R., Joseph K., Oommen Z., Thomas S.: Molecular transport of aromatic solvents through microcomposites of natural rubber (NR), carboxylated styrene butadiene rubber (XSBR) and their blends. *Composites Science and Technology*, **67**, 1187–1194 (2007).
DOI: [10.1016/j.compscitech.2006.05.009](https://doi.org/10.1016/j.compscitech.2006.05.009)
- [33] Gupta N. S.: *Chitin*. Springer, New York (2011).

Macro-micro relationship in nanostructured functional composites

A. Zanotto¹, A. Spinella¹, G. Nasillo¹, E. Caponetti^{1,2}, A. S. Luyt^{3*}

¹Centro Grandi Apparecchiature, UninetLab, Via Marini 14, 90128 Palermo Italy

²Dipartimento di Chimica “Stanislao Cannizzaro” Università degli studi di Palermo Viale delle Scienze 17, 90128 Palermo, Italy

³Department of Chemistry, University of the Free State, Private Bag X13, 9866 Phuthaditjhaba, South Africa

Received 11 October 2011; accepted in revised form 2 December 2011

Abstract. This paper examines the results of the characterization of two functional composites: Poly(methyl methacrylate) (PMMA)-Ce:YAG (yttrium aluminium garnet doped with cerium) and PMMA-cobalt hexacyanoferrate (CoHCF). The composites were prepared as possible emitters in the fields of lighting thermal sensors. The prepared composites were characterized using transmission electron microscopy (TEM), nuclear magnetic resonance (NMR) spectroscopy, thermogravimetric analysis (TGA), differential scanning calorimetry (DSC) and dynamic mechanical analysis (DMA) analyses to study the correlation between micro and macro characteristics. We found that the molecular interactions of the two different fillers with the matrix were localized in different sites of the polymer chains. Moreover, the composites showed an increased thermal strength and stiffness, in particular the PMMA-Ce:YAG composite.

Keywords: nanocomposites, PMMA, yttrium aluminium garnet doped with cerium (Ce:YAG), cobalt hexacyanoferrate (CoHCF), interfacial interaction

1. Introduction

The production of nanostructures, nanoparticles and, generally, nanostructured materials has become part of everyday scientific life, whether in the research or industrial laboratories. The embedding of nanofillers inside polymeric systems allows us to utilize the nano-features of (nanostructured) materials in addition to their functionality. Such combinations produce ductile materials possessing switchable functionalities, not only for basic research, but for the development of industrial applications.

The amount of filler used plays an important role in modifying the mechanical properties of polymers, creating new materials [1]. In functional composites the polymers allow the dispersed materials to better express their own qualities in three-dimensional space. The role of polymers is to guarantee a homo-

geneous distribution for the nanofiller to exhibit a big surface area for optical applications. During composite formation it is important that the dispersed material stays in suspension, allowing continuity in the system.

The macroscopic characteristics of the composite often reflect its own microstructure. The properties of composites depend on the unique filler properties and on the morphology and interface features of the composite [2]. Such composites will exhibit interesting electric, optical and magnetic properties. The characteristics of these systems depend on the compatibility of the constituents and the sizes of their contact surfaces.

One of the challenges of preparing nanocomposite materials is to mix compatible and homogeneous nanofillers in a polymer matrix, guaranteeing or

*Corresponding author, e-mail: LuytAS@qwa.ufs.ac.za
© BME-PT

improving the matrix performance. Poly(methyl methacrylate) (PMMA) is a commonly used thermoplastic matrix for fibres, sheet and particles. There have been several studies on PMMA-fibre composites prepared by in situ polymerization [3], solution mixing [4], or melt blending [5]. The last one is already an industrial process for fabricating carbon fibre-reinforced thermoplastic composites. A combination of solvent casting and melt mixing allowed to build composites with enhanced mechanical and electrical properties and exceptional fibre-alignment [6]. Platelets and sheets also influence the composite's thermal and mechanical properties, in relation to the material's composition and dispersion state within the matrix [7].

Musbah *et al.* [8] have just discovered that nanopowders of phosphors $Y_2O_3(Eu^{3+})$ embedded in a PMMA matrix, prepared using a laboratory mixing molder, influence almost linearly the optical and dynamic mechanical properties of the nanocomposites. The intensity of the luminescence emission spectra and storage modulus, loss modulus and glass transition temperature (T_g) of the polymer composites increased with increasing content of the nanophosphor powder.

We prepared two nanostructured composites, cobalt hexacyanoferrate (CoHCF) nanoparticles in PMMA, and yttrium aluminium garnet doped with cerium (Ce:YAG) nanoparticles in PMMA. CoHCF nanoparticles show thermochromic behaviour, exhibiting a significant and non-reversible colour change around 100°C. A new thermochromic optical sensor with memory could be developed from this new composite [9]. Ce:YAG, combined with GaN blue light emitting diodes (LED), is used for white light solid-state LED. In previous work it was described how the presence of filler (Ce:YAG) in the PMMA matrix can cause an organization of the structure into a lamellar shape around the particles [10]. This organization could influence the macro features of the composites.

The purpose of the present work was to study the possible relationships between macro- and micro-features of PMMA/CoHCF and PMMA/Ce:YAG nanocomposites by means of transmission electron microscopy (TEM) and nuclear magnetic resonance (NMR) spectroscopy, as well as thermal and thermo-mechanical analyses. PMMA was chosen as matrix

because of its transparency, ductility, recyclability and low price.

2. Experimental

2.1. Materials

Potassium hexacyanoferrate(III) $K_3[Fe(CN)_6]$ (Sigma-Aldrich ACS reagent, 244023, $\geq 99.0\%$, Schnellendorf, Germany), cobalt(II) chloride hexahydrate $CoCl_2 \cdot 6H_2O$ (Fluka Purum, crystallized, $\geq 98.5\%$, Schnellendorf, Germany) and 2,2-diethoxyacetophenone (Sigma-Aldrich, 227102, $> 95\%$, Schnellendorf, Germany), and methyl methacrylate (MMA) (Sigma-Aldrich, M55909, ≤ 30 ppm MEHQ as inhibitor, 99%, Schnellendorf, Germany) were all used as received. CoHCF nanoparticles were obtained by the reaction of potassium hexacyanoferrate and cobalt chloride hexahydrate. 16.5 mg of $K_3[Fe(CN)_6]$, dissolved into 5 mL of water (0.01 M) were added to 5 mL of stirred water containing 17.8 mg of $CoCl_2 \cdot 6H_2O$ (0.015 M) at room temperature. This instantly created a dark red suspension. $Y(NO_3)_3 \cdot 6H_2O$ (Sigma-Aldrich, 237957, 99.8%, Schnellendorf, Germany), $Al(NO_3)_3 \cdot 9H_2O$ (Sigma-Aldrich ACS reagent, 237973, $\geq 98\%$, Schnellendorf, Germany), and $Ce(NO_3)_3 \cdot 6H_2O$ (Sigma-Aldrich, 392219, 99.99%, Schnellendorf, Germany) were the sources of Y(III), Al(III), and Ce(III) ions, respectively. The other reagents were ammonia solution (E. Merck, 25 v/v%) and 2-methacrylic acid (MAA) (Sigma-Aldrich, 155721, 250 ppm MEHQ as inhibitor, 99%, Schnellendorf, Germany).

Ce:YAG nanopowder was prepared by dissolving yttrium, aluminium, and cerium nitrates in deionized water. The hydroxides were precipitated by dropwise addition of 5 M ammonia to the nitrates solution, under constant stirring, until a pH value of 8. The gelatinous precipitate thus obtained was filtered and washed several times with water to remove the residual ammonia and nitrate ions. Then the precipitate was dried at 50°C for 24 hours. The mixed hydroxides were calcined at 900°C for two hours.

PMMA nanocomposite preparation: A 5 wt% suspension of filler nanopowder in MMA and MAA monomers (molar ratio 4:1) was formed. 2,2-diethoxyacetophenone was added to start the photocuring process [3]. The dispersion was maintained under ultrasound and continuously irradiated

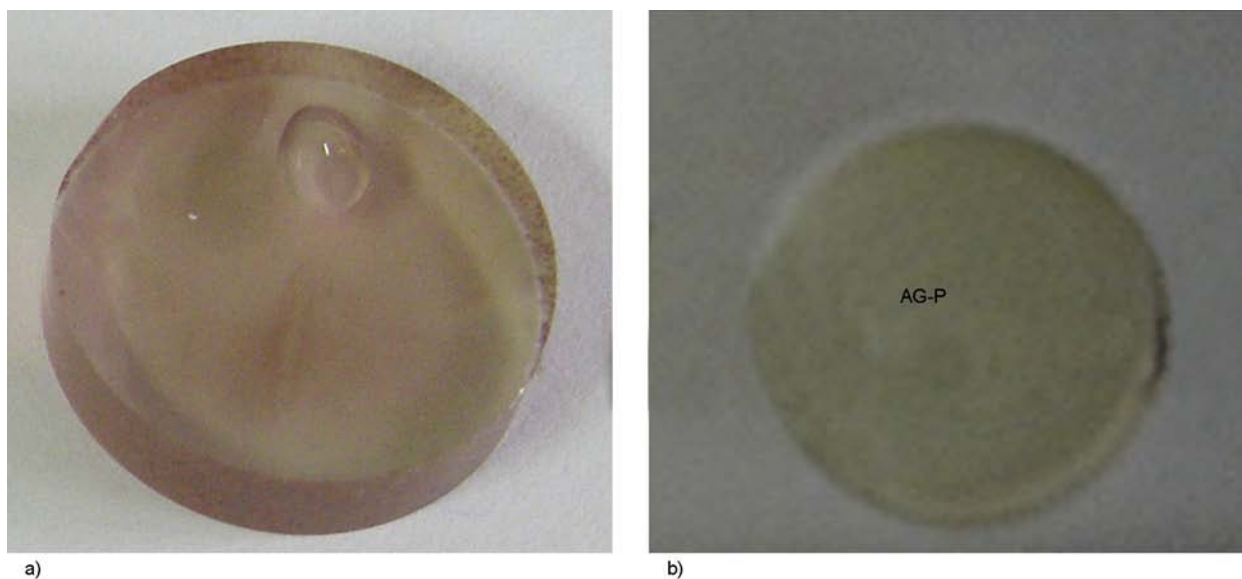


Figure 1. Picture of CoHCF-PMMA (a) and Ce:YAG-PMMA (b) composites

with a 256 nm lamp until polymerization occurred. A transparent coloured solid product, composed of the PMMA polymeric matrix containing nanoparticles, was obtained. A portion was cut and lapped to obtain a disk having a diameter of 1 cm. For the sake of comparison, pure PMMA was also prepared following the same procedure. The disks are shown in Figure 1.

2.2. Methods

2.2.1. Transmission electron microscopy (TEM)

TEM micrographs were recorded on a high-resolution transmission electron microscope (HR-TEM) JEOL JEM-2100 operating at 80 kV accelerating voltage. Elemental analysis was carried out using an Oxford Instruments energy dispersive X-ray detector (EDS). The composite was cut into thin slices using a Leica EM-UC6 ultramicrotome. The 200 nm slices were deposited on a 200-mesh copper grid, which was carbon-coated to better disperse the high energy electron beam.

2.2.2. Nuclear magnetic resonance (NMR) spectroscopy

^{13}C cross-polarization magic-angle spinning nuclear magnetic resonance (^{13}C $\{^1\text{H}\}$ CP-MAS NMR) spectra were obtained at room temperature using a Bruker Avance II 400 MHz (9.4 T) spectrometer operating at 100.63 MHz for the ^{13}C nucleus with a MAS rate of 13 kHz for 1024 scans, a contact time

of 1.5 μs , and a repetition delay of 2 s. The optimization of the Hartmann-Hahn condition was obtained using an adamantane standard. All samples were placed in a 4 mm zirconia rotor with KEL-F caps using silica as a filler to avoid inhomogeneities inside the rotor.

The proton spin-lattice relaxation time in the rotating frame $T_{1\rho}(\text{H})$ was indirectly determined, with a variable spin-lock pulse sequence, by carbon nucleus observation using a $90^\circ\text{-}\tau$ spin-lock pulse sequence prior to cross-polarization. Data acquisition was performed by ^1H decoupling with spin-lock pulse durations ranging from 0.1 to 7.5 ms and a contact time of 1.5 ms.

2.2.3. Differential scanning calorimetry (DSC)

Differential scanning calorimetry (DSC) analyses were carried out in a Perkin Elmer DSC7 differential scanning calorimeter under flowing nitrogen atmosphere (20 mL·min $^{-1}$). The instrument was calibrated using the onset temperatures of melting of indium and zinc standards, and the melting enthalpy of indium. Polymer samples (between 5 and 10 mg) were initially heated from 30 to 200°C at 10°C·min $^{-1}$, held at that temperature for 1 min to eliminate thermal history effects, and then cooled to 30°C at 10°C·min $^{-1}$. They were kept there for 1 min, heated again to 200°C at 10°C·min $^{-1}$, and cooled to 30°C at the same rate.

2.2.4. Thermogravimetric analysis (TGA)

Thermogravimetric analyses (TGA) were carried out in a Perkin Elmer TGA7 thermogravimetric analyser. Polymer samples (between 5 and 10 mg) were heated from 30 to 850°C at 20°C·min⁻¹ under flowing nitrogen (20 mL·min⁻¹).

2.2.5. Dynamic mechanical analysis (DMA)

DMA analyses were conducted in a Perkin Elmer Diamond DMA using a dual cantilever in the torsion mode. The experiments were done at a frequency of 1 Hz and a temperature range of 25 to

170°C. The sample dimensions were round disks of 10 mm diameter and 2.5 mm thick.

3. Results and discussion

A 4:1 polymeric blend of methylmethacrylate (MMA) and methacrylic acid (MAA) allowed the homogeneous dispersion of CoHCF nanoparticles and gave a dark red transparent composite, while Ce:YAG nanoparticles gave a yellow transparent composite (Figure 1).

Morphological and elemental characterization of a 200 nm thin slide of sample was carried out by

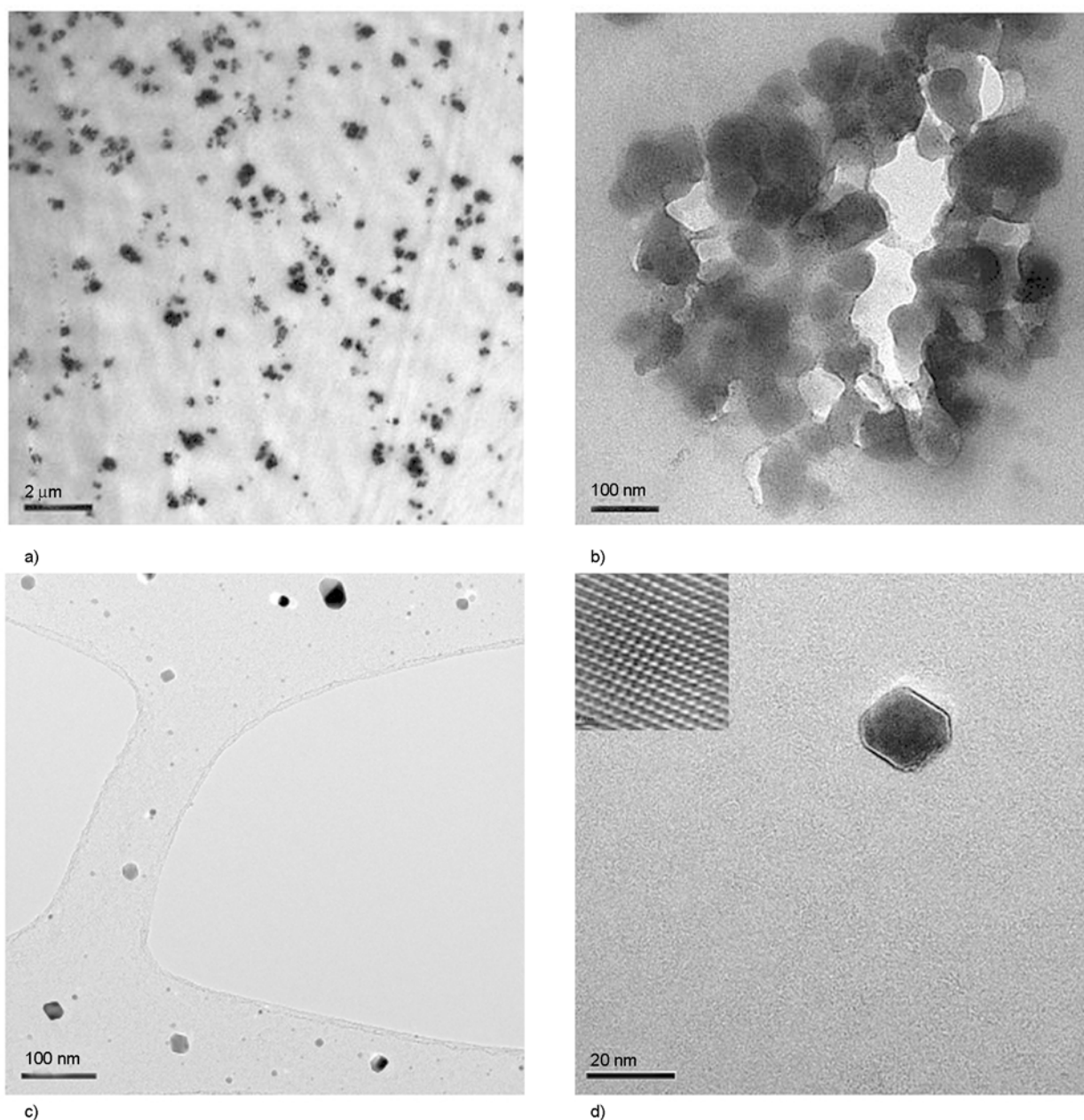


Figure 2. TEM micrographs at different enlargements of PMMA-CoHCF (a and b) and PMMA-Ce:YAG (c and d) nanocomposites. In the insert is a proof of the crystallinity of Ce:YAG.

TEM and EDS. The EDS investigations were necessary to confirm the composition of the samples. A representative example of a low enlargement micrograph is shown in Figure 2a, where a homogeneous distribution of CoHCF aggregates is observed. The CoHCF easily forms aggregates when the polar isopropanol-water solvent escapes during MMA polymerization. The reason is that in a concentrated environment the nanoparticles strongly attract each other and so the aggregates are more stable. The square structure of the CoHCF nanoparticles favours the square shape of the agglomerates. Figure 2c shows a homogeneous dispersion in the matrix of Ce:YAG nanoparticles with different sizes in the range 5–50 nm. In this case the nanoparticles are dry when dispersed in the monomer, and therefore remain dispersed during the polymerization process. Unfortunately the Ce:YAG powder, during cutting operation, creates lacerations in the 100 nm polymer slice.

A single aggregate of CoHCF nanoparticles in the composite is shown in Figure 2b. The CoHCF aggregates are constituted by 15–25 nanoparticles randomly displaced with regular dimensions between 40 and 60 nm. The nanoparticles have a quasi squared transversal section. Figure 2d shows a single Ce:YAG nanoparticle with an average diameter smaller than 20 nm. The insert in Figure 2d confirms a highly crystalline matter.

The interaction between the filler and the matrix was studied by ^{13}C -NMR CP-MAS spectroscopy and by acquiring spin-lattice relaxation times in the rotating reference system ($T_{1\rho}$). The ^{13}C -NMR spectra of pure PMMA and the composites are reported in Figure 3. In all the spectra there are the character-

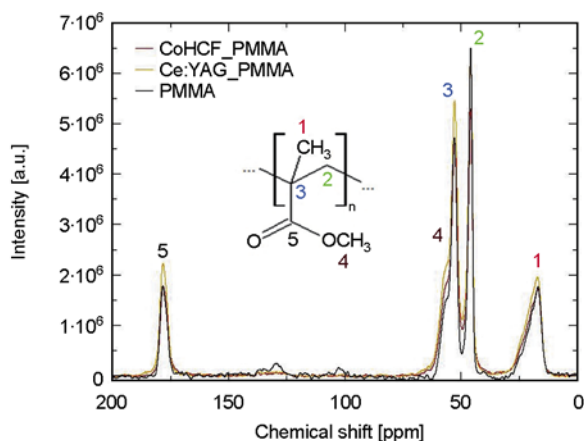


Figure 3. ^{13}C , $\{^1\text{H}\}$ CP-MAS NMR spectra of PMMA and its composites

istic peaks of the PMMA matrix in agreement with literature [11]. When comparing the spectra, no new signals, changes in peak shapes or chemical shifts are observed, so the presence of nanofiller did not induce chemical modifications in the polymeric matrix.

The NMR data show some specific interactions. The spin-lattice ($T_{1\rho}$) relaxation times in the rotating frame are sensitive to molecular motions that occur in the kHz range [12]. These motions are typically associated with arrangements of the polymeric chains that develop from collective motions of a large number of monomeric units [13]. Long range cooperative motions are those motions that define a polymer's response to mechanical perturbations [14, 15]. Moreover, $T_{1\rho}$ in the kHz frequency range is inversely proportional to the spectral density of the motion.

The $T_{1\rho}$ values of PMMA and the composites are reported in Table 1. The values in the table show an increase in the rigidity of both nanocomposites, probably due to immobilization of the polymer chains by means of filler-matrix interactions. The interactions are also locally different. The highest variation in the PMMA-CoHCF relaxation times is located in the quaternary (3) and methylenic (2) carbons on the backbone chain. An increase of $T_{1\rho}(\text{H})$ in PMMA-Ce:YAG occurs for peaks (4) and (5), the methoxylic and carbonylic groups. The interaction between the nanofiller and PMMA is principally localized around these nuclei.

The TGA curves of all three investigated samples are shown in Figure 4. It is clear that the presence of both CoHCF and Ce:YAG nanoparticles improves the thermal stability of PMMA. In the case of CoHCF the improvement is fairly insignificant, probably because the kinds of interaction between CoHCF and PMMA (as pointed out in the discussion of the NMR results) are not as strong as in the case of Ce:YAG, where there is an almost 50°C improvement in thermal stability. As shown in the discus-

Table 1. $T_{1\rho}(\text{H})$ values for all the peaks in the ^{13}C spectra of PMMA, PMMA-CoHCF and PMMA-Ce:YAG

Peak	ppm	$T_{1\rho}(\text{H})$ [ms]		
		PMMA	CoHCF/PMMA	Ce:YAG-PMMA
1	16.4	6.6±0.2	20.4±0.4	9.0±0.4
2	45.5	7.0±0.2	44.2±0.2	12.8±0.2
3	52.7	7.6±0.3	71.9±0.3	13.6±0.3
4	55.1	7.2±0.2	15.0±0.4	15.0±0.4
5	178.1	6.4±0.4	24.8±0.7	24.8±0.7

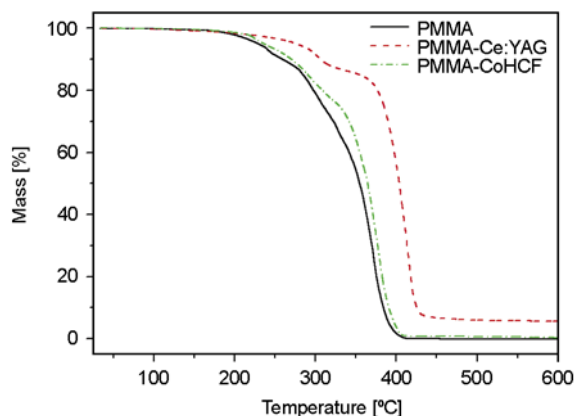


Figure 4. TGA curves of PMMA and its composites

sion above, there is a much better dispersion of Ce:YAG nanoparticles in PMMA, and a much stronger interaction between PMMA and Ce:YAG. This will not only immobilize the polymer chains but also the free radicals that take part in the degradation process. This stronger interaction is probably also the result of a local structured distribution of PMMA chains around the Ce:YAG nanoparticles [10].

The second heating DSC curve of PMMA-CoHCF (Figure 5) shows a shift in T_g to a higher temperature by about 6°C. These results are reported in the Table 2. The higher glass transition temperature indicates the immobilization of the polymer chains because of their interaction with the nanoparticles. The DSC curve of PMMA-Ce:YAG shows an

Table 2. Glass transition temperatures for the different investigated samples

Sample	T_g [°C]
PMMA	84.1
PMMA-CoHCF	89.8
PMMA-Ce:YAG	119.5

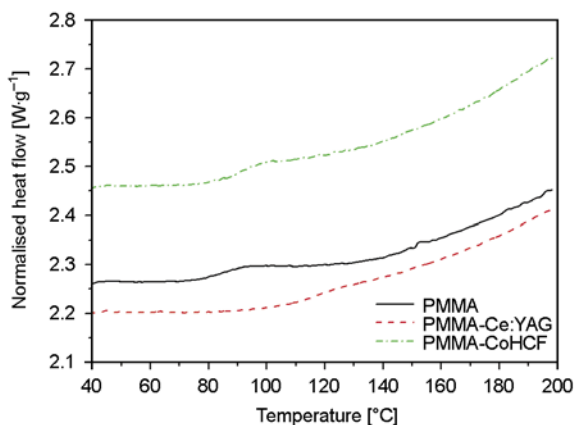


Figure 5. Second heating DSC curves of PMMA and its composites

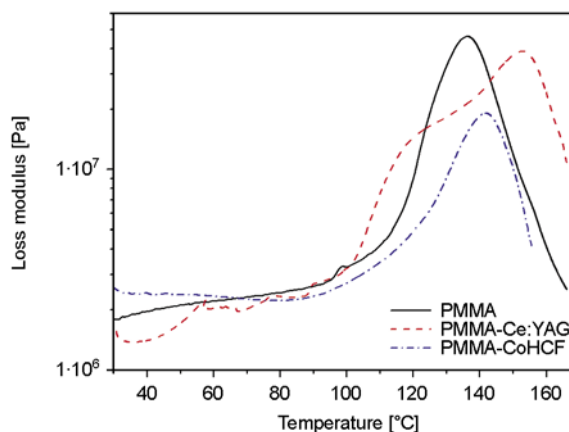


Figure 6. DMA loss modulus curves of PMMA and its composites

increase of 35°C in the glass transition temperature compared to that of the pure polymer. This transition is, however, not very well resolved. This shows that the interaction between the Ce:YAG nanoparticles and the PMMA chains, and the resultant immobilization of the polymer chains, was much stronger. The DMA loss modulus curves in Figure 6 confirm the DSC observations of the changes in the glass transition in the presence of the nanofillers. In this case, however, the T_g are significantly higher than those observed in the DSC curves, but such behaviour was observed before [16, 17], and there could be a number of reasons for this. However, the important thing is that the difference between the T_g values for PMMA and PMMA-CoHCF is 6°C, as was also observed from the DSC curves. The difference between these values for PMMA and PMMA-Ce:YAG is, however, only 17°C from the DMA curves, but it is quite possible that the T_g value from the DSC curve of PMMA-Ce:YAG is not completely correct because of the badly resolved glass transition.

4. Conclusions

Both the investigated PMMA-Ce:YAG and PMMA-CoHCF composites show a homogeneous distribution of nanoparticles inside the polymer. The CoHCF is mostly agglomerated, while the Ce:YAG shows more dispersed nanoparticles. The presence of these nanofillers improved the thermal stability of PMMA for both CoHCF and Ce:YAG, and in particular PMMA-Ce:YAG shows a 50°C improvement in thermal stability. The T_g of both composites were higher than that of the matrix, with the largest

increase observed for PMMA-Ce:YAG. The interactions of CoHCF with PMMA are localized around the quaternary and methylenic carbons on the backbone chain, and those for PMMA-Ce:YAG are around the methoxylic and carbonylic groups.

Acknowledgements

The National Research Foundation of South Africa and the University of the Free State are acknowledged for financial support of this project.

References

- [1] Tjong S. C.: Structural and mechanical properties of polymer nanocomposites. *Materials Science and Engineering R: Reports*, **53**, 73–197 (2006).
DOI: [10.1016/j.mser.2006.06.001](https://doi.org/10.1016/j.mser.2006.06.001)
- [2] Hussain F., Hojjati M., Okamoto M., Gorga R. E.: Review article: Polymer-matrix nanocomposites, processing, manufacturing, and application: An overview. *Journal of Composite Materials*, **40**, 1511–1575 (2006).
DOI: [10.1177/0021998306067321](https://doi.org/10.1177/0021998306067321)
- [3] Jia Z., Wang Z., Xu C., Liang J., Wei B., Wu D., Zhu S.: Study on poly(methyl methacrylate)/carbon nanotube composites. *Materials Science and Engineering A*, **271**, 395–400 (1999).
DOI: [10.1016/S0921-5093\(99\)00263-4](https://doi.org/10.1016/S0921-5093(99)00263-4)
- [4] Stéphan C., Nguyen T. P., de la Chapelle M. L., Lefrant S., Journet C., Bernier P.: Characterization of singlewalled carbon nanotubes-PMMA composites. *Synthetic Metals*, **108**, 139–149 (2000).
DOI: [10.1016/S0379-6779\(99\)00259-3](https://doi.org/10.1016/S0379-6779(99)00259-3)
- [5] Jin Z., Pramoda K. P., Xu G., Goh S. H.: Dynamic mechanical behavior of melt-processed multi-walled carbon nanotube/poly(methyl methacrylate) composites. *Chemical Physics Letters*, **337**, 43–47 (2001).
DOI: [10.1016/S0009-2614\(01\)00186-5](https://doi.org/10.1016/S0009-2614(01)00186-5)
- [6] Haggenueller R., Gommans H. H., Rinzler A. G., Fischer J. E., Winey K. I.: Aligned single-wall carbon nanotubes in composites by melt processing methods. *Chemical Physics Letters*, **330**, 219–225 (2000).
DOI: [10.1016/S0009-2614\(00\)01013-7](https://doi.org/10.1016/S0009-2614(00)01013-7)
- [7] Potts J. R., Dreyer D. R., Bielawski C. W., Ruoff R. S.: Graphene-based polymer nanocomposites. *Polymer*, **52**, 5–25 (2011).
DOI: [10.1016/j.polymer.2010.11.042](https://doi.org/10.1016/j.polymer.2010.11.042)
- [8] Musbah S. S., Radojević V. J., Borna N. V., Stojanović D. B., Dramićanin M. D., Marinković A. D., Aleksić R. R.: PMMA-Y₂O₃ (Eu³⁺) nanocomposites: Optical and mechanical properties. *Journal of the Serbian Chemical Society*, **76**, 1153–1161 (2011).
DOI: [10.2298/JSC100330094M](https://doi.org/10.2298/JSC100330094M)
- [9] Zanotto A., Matassa R., Saladino M. L., Berrettoni M., Giorgetti M., Zamponi S., Caponetti E.: Cobalt hexacyanoferrate–poly(methyl methacrylate) composite: Synthesis and characterization. *Materials Chemistry and Physics*, **120**, 118–122 (2010).
DOI: [10.1016/j.matchemphys.2009.10.032](https://doi.org/10.1016/j.matchemphys.2009.10.032)
- [10] Saladino M. L., Zanotto A., Martino D. C., Spinella A., Nasillo G., Caponetti E.: Ce:YAG nanoparticles embedded in a PMMA matrix: Preparation and characterization. *Langmuir*, **26**, 13442–13449 (2010).
DOI: [10.1021/la9042809](https://doi.org/10.1021/la9042809)
- [11] Eijkelenboom A. P. A. M., Maas W. E. J. R., Veeman W. S., Werumeus Buning G. H., Vankan J. M. J.: Triple-resonance fluorine-19, proton, and carbon-13 CP-MAS NMR study of the influence of PMMA tacticity on the miscibility in PMMA/poly(vinylidene fluoride) (PVF2) blends. *Macromolecules*, **25**, 4511–4518 (1992).
DOI: [10.1021/ma00044a009](https://doi.org/10.1021/ma00044a009)
- [12] Edzes H. T., Veeman W. S.: ¹³C NMR spin-lattice relaxation in solid poly(methyl methacrylate). *Polymer Bulletin*, **5**, 255–261 (1981).
DOI: [10.1007/BF00254711](https://doi.org/10.1007/BF00254711)
- [13] Boyer R. F.: Dependence of mechanical properties on molecular motion in polymers. *Polymer Engineering and Science*, **8**, 161–185 (1968).
DOI: [10.1002/pen.760080302](https://doi.org/10.1002/pen.760080302)
- [14] Farrar T. C., Becker E. D.: Pulse and fourier transform NMR. Academic Press, New York (1971).
- [15] Campbell I. D., Dwek R. A.: Biological spectroscopy. The Benjamin Cummings Publishing Corporation, Menlo Park (1984).
- [16] Yazdi M. H., Lee-Sullivan P.: Determination of dual glass transition temperatures of a PC/ABS blend using two TMA modes. *Journal of Thermal Analysis and Calorimetry*, **96**, 7–14 (2009).
DOI: [10.1007/s10973-008-9831-3](https://doi.org/10.1007/s10973-008-9831-3)
- [17] Narine S. S., Kong X., Bouzidi L., Sporns P.: Physical properties of polyurethanes produced from polyols from seed oils: I. Elastomers. *Journal of the American Oil Chemists' Society*, **84**, 55–63 (2007).
DOI: [10.1007/s11746-006-1006-4](https://doi.org/10.1007/s11746-006-1006-4)

On the performance of a viscoelastic constitutive model for micro injection moulding simulations

A. Gava, G. Lucchetta*

University of Padova, Department of Innovation in Mechanics and Management, Via Venezia, 1 - 35131 Padova, Italy

Received 16 September, 2011; accepted in revised form 5 December 2011

Abstract. The numerical simulation of the injection moulding process involving microstructures presents several challenges, mainly due to the surface effects that dominate the flow behaviour at the microscale. In this paper a new approach, which employs weld lines as flow markers, is used to evaluate whether the numerical codes that are normally used to simulate the conventional injection moulding process, are suitable to characterize the melt flow patterns in the filling of micro features. The Cross-WLF viscous model and the Giesekus viscoelastic model were evaluated using 3D models of a micro part implemented in two different numerical codes. A micro cavity was designed in order to compare the results of numerical simulations and experiments. While the viscous simulations were found to be inappropriate for multi-scale structures, the accuracy of micro filling predictions was significantly improved by implementing a viscoelastic material model.

Keywords: *rheology, modelling and simulation, micro injection moulding*

1. Introduction

Due to their cost effectiveness and rapid response, numerical simulations have become an increasingly important tool for the evaluation of part design, mould geometry and processing parameters in injection moulding. Numerical investigations are able to estimate aspects of the physical model which otherwise would be difficult to quantify. They allow quick responses on what will be the effects of process parameters changes on the final part. Although Computer Aided Engineering (CAE) has been used with increasing success in the design and manufacture of polymer products and processes, the simulation of the injection moulding process involving microstructures (μ IM) presents many challenges. The flow behaviour of polymer melts in mould micro cavities is not fully understood. It is believed that, due to the large surface-to-volume ratio, surface effects dominate the flow behaviour at the microscale [1]. Kemann *et al.* [2] showed that stan-

dard injection moulding simulation packages are not able to describe all of the effects in micro-moulding. The rheological data used in current packages are obtained from macroscopic experiments and they are not suitable for modelling microscale flows. In fact, when flowing in micro channels a polymer has a strong tendency to slip [3]. If a classic no-slip boundary condition is used in current packages, the consequences of wall slip cannot be predicted. Furthermore, the microscale dimensions of features and rapid filling rates typically occurring within micro cavities, ensure that the values of shear rate, experienced by the polymer during the micro moulding process, are orders of magnitude higher than those experienced in conventional injection moulding. The extensional behaviour in contraction flow or the pressure influence on the viscosity cannot be neglected as well. Also, the mould/melt heat transfer coefficient was found to be a critical factor in determining the filling lengths [4]. A

*Corresponding author, e-mail: giovanni.lucchetta@unipd.it
© BME-PT

significant decrease in the Nusselt number was observed concerning the laminar flow in microscale channels. This means that a constant heat transfer coefficient may not be applicable to the heat transfer simulation involving flow through microscale channels.

The assumption of a generalized Newtonian fluid is generally used for traditional injection moulding because the importance of elasticity compared to viscous effects is negligible. Because of high deformation rates during the injection phase of high speed micro injection moulding, it is expected that elastic effects will occur. Therefore there is a need to translate the complex rheological behaviour of polymeric fluids into suitable equations, and to use these models to predict flow in micro cavities. During the last decade substantial progress has been made in the numerical simulation of viscoelastic flows. Extensions to non-isothermal and three-dimensional viscoelastic simulations are in progress [5]. Several constitutive equations have been proposed, but none of them has been proven to be superior to others [6].

The main objective of this work is to evaluate whether the present numerical commercial codes are suitable to characterize melt flow patterns in a micro-cavity, using both Autodesk Moldflow Insight[®], i.e. a dedicated simulation software, and a general purpose fluid dynamic finite element (FEM) code such as Ansys Polyflow[®]. This paper also reports on the suitability of 3D general purpose computational fluid dynamic (CFD) software to be used for injection moulding simulations.

The approach proposed to compare the predictions of numerical simulations to moulding results (Figure 1) consists in the determination of the flow pattern by using weld lines as flow markers. This is an alternative technique to the ‘short shots’ method, which predicts the shape of the free surfaces with a large approximation due to stress relaxation and thermal contraction.

2. Experimental setup and data acquisition

The mould micro cavity considered in this study was designed to create an effective response variable to compare the results of numerical simulations and experiments. Obstacles as high as the total depth of the cavity were created. In this way, the melt flow was not allowed to climb over the features and when the separated melt fronts rejoined, at some downstream location, weld lines were formed. Geometries and dimensions (Figure 2) were selected according to existing industrial devices (blood separators and micro pumps) and in order to exalt such factors that change their relevance when shifting from conventional to micro injection moulding, such as:

- elongational flow,
- heat transfer in different thickness,
- wall slip,
- elastic behaviour of polymers.

In the first part of the cavity, a convergent geometry was created in order to pull out the extensional flow and elastic behaviour of the melt in convergent/divergent geometries. A step was created in the middle part of the cavity in order to originate a three

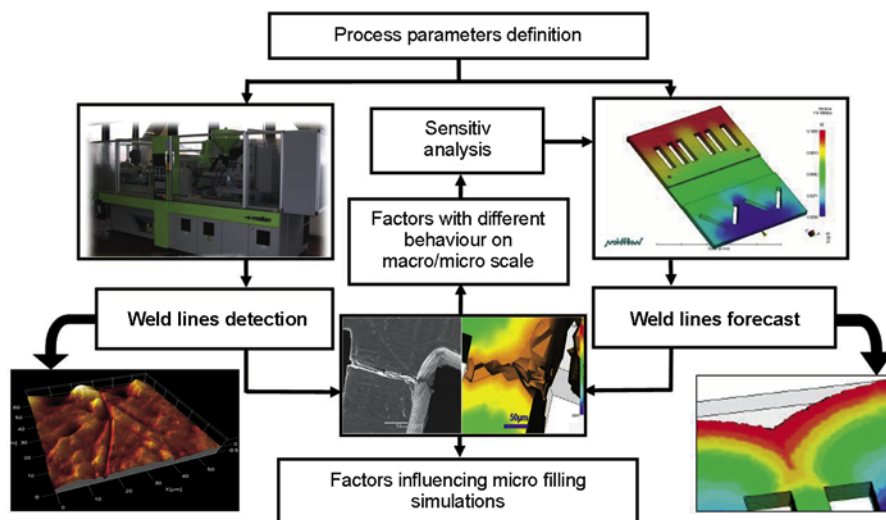


Figure 1. Proposed approach for the filling validation

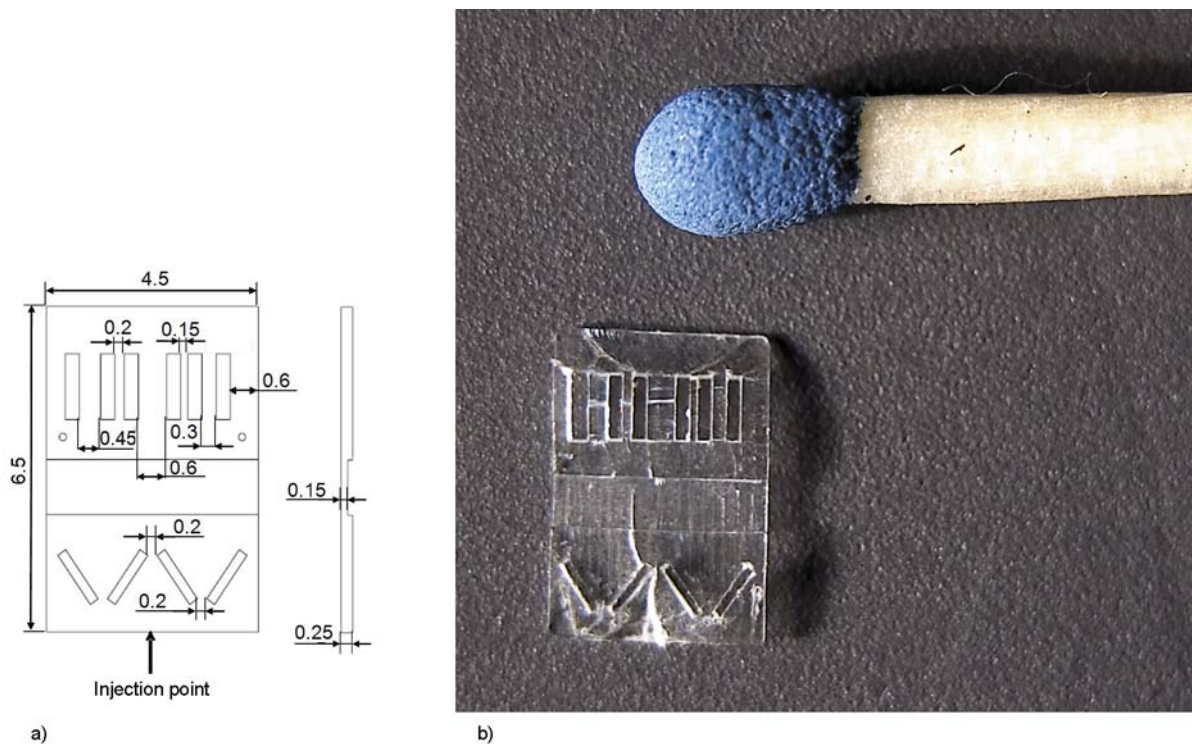


Figure 2. Micro part design (part volume 6 mm³) (a) and manufactured part (b)

dimensional flow and to align the flow front before the micro channels entrance; furthermore, the direction of the expected weld line, after the two holes, could give information regarding the shape of the flow front in the second part of the cavity.

Channels as wide as 150, 200, 300, 450 and 600 μm were created in the second part. Heat transfer in variable thickness and different rheological models were considered. The gate (400 μm wide and 250 μm thick) was realised as small as possible, in order to approximate it as an injection point.

The experiments were performed using a high fluidity class polystyrene, the PS 143 E produced by BASF (Ludwigshafen, Germany). Polystyrene is relevant in micro injection moulding for its very low viscosity, good biocompatibility, high optical clarity, high transparency and high impact strength compared to silicon or glass. The polymer was injected into the mould cavity setting a constant speed profile of 350 mm/s. The melt temperature in the feeding zone was maintained at 230°C. The mould temperature was controlled by a heater and maintained at 70°C.

In order to obtain a closer control on the boundary conditions and a good comparison between simulations and experiments, temperature and pressure transducers were positioned near the cavity surface.

The following parameters were acquired during the injection moulding process:

- hydraulic pressure,
- ram position,
- cavity pressure near gate,
- cavity surface temperature.

The pressure and temperature transducers were mounted in the fixed mould part.

In order to analyse the filling of the micro cavity, the position and direction of weld lines were used as measurable outputs. To describe the shape of the weld lines, an accurate measurement of the weld line path on the sample was required. The investigation strategy consisted in detecting the X and Y coordinates of points on the weld lines with an optical coordinate measurement machine (CMM) (Video Check IP 400, Werth Messtechnik, Giessen, Germany) and to plot them in a determined and repeatable reference system.

Measuring uncertainty was estimated taking into account the optical CMM calibration on the measured dimensional range, repeatability of the measurement on 5 repetitions, CMM resolution, definition of the measurand and the influence of the temperature (i.e. expansion of the plastic due to temperature variations). The combined expanded measuring uncertainty, calculated with a coverage factor $k = 2$

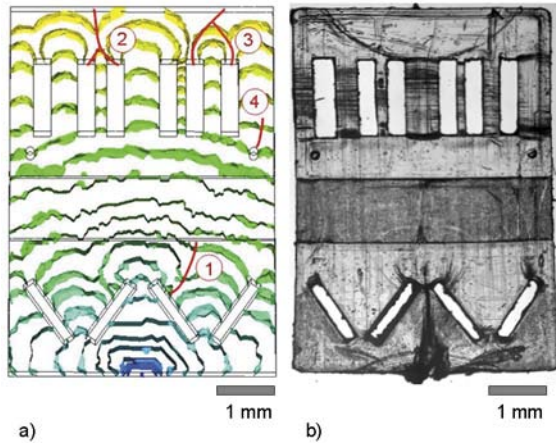


Figure 3. Moldflow[®] filling simulation results (a) and injection moulded part (b)

(level of confidence 95%), resulted in 4 μm on the *X* direction and in 3 μm on the *Y* direction. The investigated area and the injection moulded part are represented in Figure 3 [7].

3. Viscous and viscoelastic material characterization

In order to have a closer control on the boundary conditions setup and to improve numerical simulation results, the PS 143 E by BASF was characterized both by means of a rotational and a capillary rheometer.

Steady shear measurements were performed on a dual bore capillary rheometer (Rheo 2500, Ceast, Pianezza, Italy) at three different temperatures (190, 210 and 230°C) with a shear rate range of 100 to 10000 s⁻¹. The shear-dependent viscosity data were fitted to the Cross model (Figure 4, Equation (1)):

$$\eta_s = \frac{\eta_0}{1 + \left(\frac{\eta_0 \dot{\gamma}}{\tau^*}\right)^{1-n}} \quad (1)$$

where η_0 is the viscosity at zero shear and τ^* and n are data-fitted coefficients. The effect of temperature on viscosity was accounted by means of the Williams–Landel–Ferry (WLF) model (as defined by Equations (2)–(4)):

$$\eta_0 = D_1 \exp\left[\frac{-A_1(T - T^*)}{A_2 + (T - T^*)}\right] \quad (2)$$

$$T^* = D_2 + D_3 \cdot P \quad (3)$$

$$A_2 = \tilde{A}_2 + D_3 \cdot P \quad (4)$$

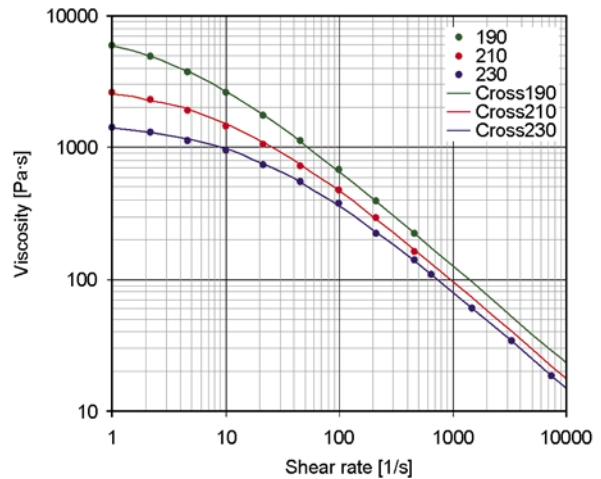


Figure 4. Experimental data and Cross-WLF fitting for the steady shear viscosity of PS 143E

Table 1. Cross-WLF model constants for PS 143E

	Cross		WLF		
n	0.25433	D_1 [Pa·s]	$9.47833 \cdot 10^{26}$	A_1	56.342
η_0 [Pa·s]	1548.89	D_2 [K]	428.15	\tilde{A}_2 [K]	2.192
τ^* [Pa]	31210.18	D_3 [K/Pa]	$2.1 \cdot 10^{-7}$		

where D_1 , D_2 , D_3 , A_1 and \tilde{A}_2 are constants to be determined while T^* is a reference temperature [8]. Model constants implemented in the numerical simulations are summarized in Table 1. Pressure dependence of viscosity was measured by using a throttle apparatus arranged in series with the die of the capillary rheometer [8]. Data obtained from experiments in a pressure range of 40 MPa were fitted according to the Cross model and the D_3 coefficient was estimated as $2.1 \cdot 10^{-7}$ K/Pa.

Due to the high deformation rates, extensional deformations also play a significant role in the process. Thereby, for the viscous simulation the Moldflow[®] ‘unified’ viscosity model for mixed shear and extension deformations was used. In this model the apparent viscosity is modelled as a function of the extension rate and the shear viscosity using the extension viscosity model coefficients. These coefficients were determined using experimental pressure measurements in convergent flow. The apparent viscosity, η_a , is modelled according to Equation (5):

$$\eta_a(T, P, \dot{\gamma}, \dot{\epsilon}) = f(\dot{\epsilon}) \eta_s(T, P, \dot{\gamma}) \quad (5)$$

where η_s is the shear viscosity calculated by the Cross-WLF model and f is a transition function defined by Equation (6):

$$f(\dot{\epsilon}) = 1 + \frac{A \cdot \dot{\epsilon}}{B + \dot{\epsilon}} \quad (6)$$

where the elongational rate is determined from the entrance pressure loss in a capillary according to the Cogswell approach [9], while A and B are data-fitted coefficients respectively related to the magnitude of the elongational effect and to the extension rate of the transition to strong elongational stresses (Table 2).

On the other hand, for the viscoelastic simulation dynamic experiments were performed on a rotational rheometer (ARES, TA Instruments, New Castle, USA) at three different temperatures (190, 210 and 230°C) in a frequency range $\omega = 0.1\text{--}100\text{ s}^{-1}$. A parallel disk geometry was chosen rather than a cone plate apparatus for practical reasons. The samples, prepared by compression moulding of the pellets, were maintained under nitrogen atmosphere to avoid polymer degradation by oxidation. Measurements were performed in frequency sweep mode with a 5% deformation amplitude. Three measurement points per decade were taken at increasing frequencies. The rheological functions were shifted to a master-curve at reference temperature of 230°C using the time temperature superposition [10]. The horizontal shift factor $a_T(T, T_{ref})$ follows from the loss angle (δ) and the vertical shift factor $b_T(T, T_{ref})$ from the dynamic modulus (G_d) (see Equations (7) and (8)):

$$\delta(\omega, T) = \delta(\omega_{a_T}, T_{ref}) \quad (7)$$

$$G_d(\omega, T) = b_T G_d(\omega_{a_T}, T_{ref}) \quad (8)$$

The shift factors obtained experimentally (Table 3) were plotted as a function of temperature and fitted according to the WLF equation.

Dynamic experiments allowed to determine the relaxation spectrum, i.e. the set of relaxation times,

Table 2. Extension viscosity coefficients for PS 143E

Coefficients	A	B
	0.309	297.26

Table 3. Horizontal and vertical shift factors obtained from experimental data

Temperature [°C]	a_T	b_T
190	8.62998	1.25456
210	2.70511	1.21066
230	1	1

by fitting with experimental data the expressions predicted by the viscoelastic Giesekus model in the case of small-amplitude oscillatory shear flow. The Giesekus model was selected because it gives satisfactory predictions in the standard rheometrical tests that appear most relevant for the flow under consideration [11]. The Giesekus model, belonging to the class of Maxwell-type differential constitutive equations, is capable of describing the complex rheological behaviour of a material at various deformation histories. By introducing several uncoupled or coupled discrete relaxation modes it can be shown that the area of concordance between predictions of the model and experimental results for polymer solutions can be considerably extended [12]. The model can be written as shown by Equation (9):

$$\lambda \overset{\nabla}{\bar{\tau}} + \left(\bar{I} + \frac{\alpha \lambda}{\eta_v} \bar{\tau}_v \right) \bar{\tau}_v = 2 \eta_v \bar{D}(\bar{u}) \quad (9)$$

where λ is the relaxation time, $\bar{\tau}_v$ is the viscoelastic part of the extra-tensor, η_v is the viscoelastic contribution to viscosity, α is a dimensionless mobility parameter and \bar{D} is the rate of strain tensor [11]. Multiple relaxation times have been used in order to better fit the viscoelastic behaviour at different shear rates and improve accuracy of simulation results. Complex viscosity, loss and storage moduli were fitted according to a 4-mode Giesekus model (Figure 5).

In the model, nonlinear effects are introduced by taking into account an average anisotropy of the molecular conformation during flow. The strength of influence to the conformation and the retroaction

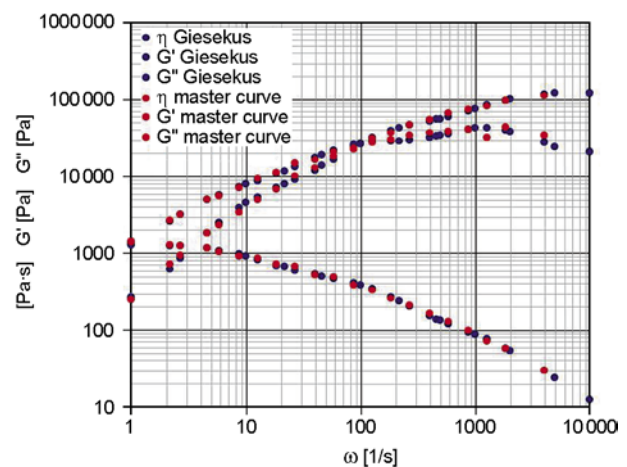


Figure 5. Comparison of complex viscosity, loss and storage moduli predicted by a 4-mode Giesekus model with experimental data for PS at reference $T = 230^\circ\text{C}$

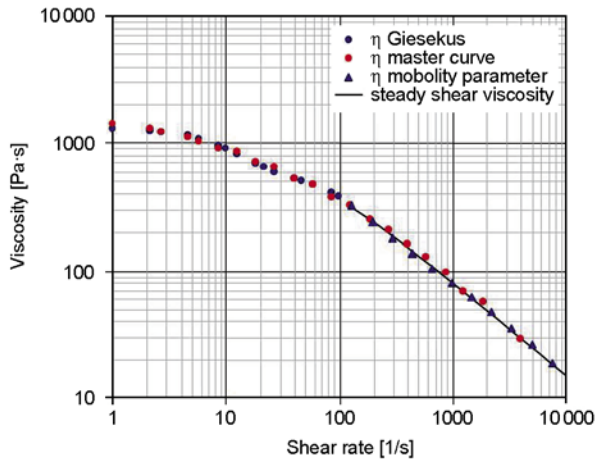


Figure 6. Fitting of non-linear parameter. Comparison of steady shear viscosity (as a function of shear rate) with linear viscosity (as a function of frequency).

to the flow is determined by an anisotropic mobility parameter α . At $\alpha = 0$ the isotropic Maxwell model is recovered. When α is set to unity the model predicts similar behaviour in elongation flows as the corotational Maxwell model. At intermediate values of α , the Giesekus model fits steady and transient shear flows better than any other differential constitutive equation [5]. A best fit for the α parameter (Figure 6) was obtained by minimizing the deviation from the steady shear experiments conducted on the capillary rheometer with the function defined by Equation (10):

$$R = \sum_{j=1}^N \left[\left(\frac{G'(\omega_j)}{G'_{exp,j}} - 1 \right)^2 + \left(\frac{G''(\omega_j)}{G''_{exp,j}} - 1 \right)^2 \right] \quad (10)$$

where j indicates the individual data points. The knowledge of both the flow field and the fluid properties determines the character of the flow. In particular, the Deborah number is used to characterize the fluid elasticity, which is defined as the ratio of the material characteristic relaxation time λ to the characteristic flow time t (Equation (11)):

$$De = \frac{\lambda}{t} \quad (11)$$

The weighted relaxation time was calculated as shown by Equation (12):

$$\lambda = \frac{\sum_{i=1}^4 \eta_i \lambda_i}{\sum_{i=1}^4 \eta_i} \quad (12)$$

The estimated Deborah number is 11.6. This value confirms the hypothesis that the filling behaviour is influenced by viscoelastic effects. In this case the value calculated for the Deborah number is not comparable to values typical of the conventional injection moulding process. This establishes that the elastic behaviour of the polymer melt has to be considered.

4. Numerical simulations

As a first approach a three-dimensional finite element Moldflow[®] analysis was performed in order to simulate the micro injection moulding process. The main material functions considered are the ‘unified’ viscosity model and the two-domain Tait model for the pvT data. Non-Newtonian, non-isothermal flow solutions were obtained by solving the momentum, mass and energy governing equations. No-slip boundary conditions were imposed on the cavity walls filled by the polymer, while on the unfilled part, a free boundary condition allowed for the formation of the typical fountain flow. The melt temperature is a potential problematic parameter in terms of modelling. In practice, the melt temperature is only indirectly controlled through the barrel temperature zones. It was therefore decided to consider it as equal to the barrel temperature. The mould temperature was defined as the mean value of the mould surface acquired by the temperature transducers. The simulations were performed implementing the ram speed profile as set in the machine. The numerical simulation was carried out using the 3D mesh shown in Figure 7. A sensitivity analysis of software simulation to the mesh dimension was conducted. It was decided, as a result, to mesh the

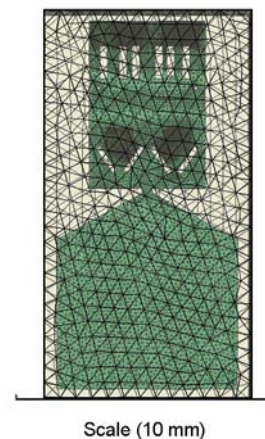


Figure 7. Mesh of the 3D model considered in Moldflow[®] simulation

part model together with the feeding system and to decrease the mesh size in the cavity zones where the weld lines were experimentally detected.

As a second approach a three dimensional viscoelastic simulation was performed in the Ansys Polyflow[®] environment. Polyflow[®] is a finite-element program primarily designed for the analysis of industrial flow processes dominated by non-linear viscous phenomena and viscoelastic effects. The theoretical foundation is provided by the general principles of continuum mechanics, together with phenomenological and kinetic theoretical models for describing the rheological behaviour of the fluid.

The model was created and meshed in Gambit[®] and simulations were performed in Polydata[®] implementing the same previous boundary conditions. Stress (one stress field for each mode, or relaxation time), velocity and pressure are computed simultaneously. Furthermore, the problem involves flow, heat transfer by conduction and convection and heat generation by viscous dissipation. Energy, momentum and mass governing equations were solved in the fluid domain implementing the viscoelastic properties of the material.

In the viscoelastic simulation, the total extra-stress tensor $\bar{\tau}$ is divided into a purely viscous part (Newtonian) and a viscoelastic part (Equation (13)):

$$\bar{\tau} = \bar{\tau}_n + \bar{\tau}_v \quad (13)$$

where the subscripts n and v stand for Newtonian and viscoelastic contributions, respectively. The Newtonian part, which can be seen as the stress response associated with fast relaxation modes, is written as shown by Equation (14):

$$\bar{\tau}_v = 2\eta_n \bar{D}(\bar{u}) \quad (14)$$

$\bar{\tau}_v$ is computed according to the Giesekus model [11].

When a multi-mode viscoelastic model is used, the total extra-stress tensor is decomposed into a sum of individual viscoelastic components and any purely-viscous component. To prevent ambiguous definition of purely-viscous component, the corresponding viscosity factor is defined together with the first mode. Consequently, the remaining modes will not contain any purely-viscous components.

In this work a numerical analysis was performed defining three solid and one fluid sub-domains (Figure 8):

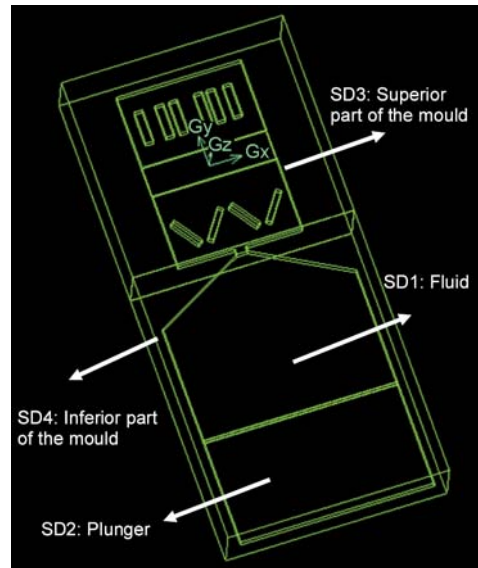


Figure 8. Sub-domains definition defined on Polyflow[®] environment

- a fluid domain (SD1)
- a plunger (SD2)
- the inferior part of the mould (SD3)
- the superior part of the mould (SD4).

The finite element meshes are represented in Figure 9. Three dimensional finite elements are defined for fluid gob, mould and plunger. In particular the fluid domain and the superior part of the mould are meshed by triangles while the inferior part of the mould and the plunger are meshed by quadrilaterals. The 3D mesh model is represented in the initial configuration, before pressing the fluid. At a prescribed time the plunger moves downwards and presses this fluid domain in the mould cavity.

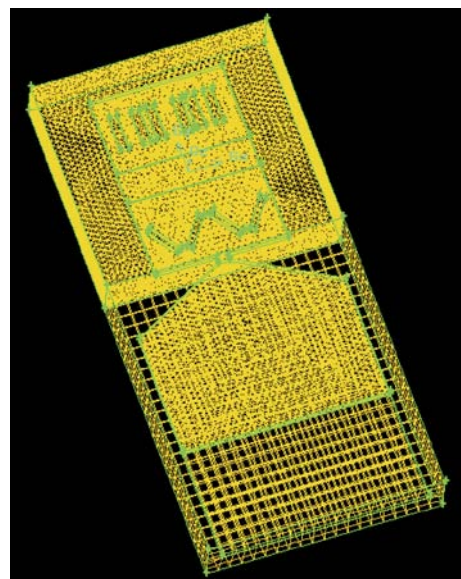


Figure 9. Finite element mesh of the model in Polyflow[®] environment

A major difficulty to be overcome in the simulation arises from the fact that the filling domain evolves considerably over time. The position of the front is an unknown, which means that the limit of the domain under investigation (i.e. filled with polymer melt) is an unknown. This is called a free surface problem and has given rise to a large number of methods, which can be classified into two categories. The first approach consists in using control volumes defined on a fixed mesh, covering the entire domain to be filled, with the use of an additional variable representing the volume fraction of the injected polymer within the control volumes (and without front discretization). The second approach is based on accurately tracking the flow front and adapting the mesh, at each time step, in order to cover only the filled domain. This latter front tracking-remeshing approach was selected to solve the micro injection moulding problem, since an accurate representation of the front at an affordable computational cost was required in this small scale problem. Indeed, the second class of methods requires refined finite element meshes in the front vicinity. Besides this, the exact position of front meetings was intrinsically interesting as related to the weld line position. The fluid domain was, therefore, considered as a free surface and a Lagrangian remeshing technique was applied. In the Polyflow[®] environment, remeshing techniques are based only on the positions and displacements of the boundary nodes, and not on kinematic considerations, unless a Lagrangian or streamwise method is used for remeshing. Tangential remeshing preserves the original node distribution along a surface for three dimen-

sional moving domains. In transient iterative parameters a maximum value of 10^{-6} s was set as the time step in order to contain deformation of the elements before remeshing.

5. Results

An extensive measurement campaign of the experimental and simulated weld lines positions was carried out covering weld lines located in several areas of the micro component. Two different outputs were considered: the weld line number 1 and the line 1 of the weld line number 3. These two weld lines were selected because they originate in zones of the micro cavity where the elastic behaviour of the fluid should not be neglected. In correspondence with the first part of the micro cavity, a contraction flow is opposed to an expansion flow. Two different streamlines were acquired at 1.2 ms both in Moldflow[®] (yellow) and in Polyflow[®] (red) simulations (Figure 10). In the expansion flow, the streamline in the viscoelastic simulation reveals a more elastic behaviour if compared to the viscous simulation. On the other hand, the streamline at the contraction exit is delayed due to normal stresses and resistance to elongational deformation during the contraction flow. As a consequence, the viscoelastic numerical weld line moves towards the experimental one. As a second case, the horizontal line in the 150 μm wide micro channel was considered. Figure 11 shows how the viscous numerical simulation overpredicts the ease at which the polymer would flow through this channel; on the other hand, the viscoelastic one underpredicts (with a lower absolute error) the weld line position. The dif-

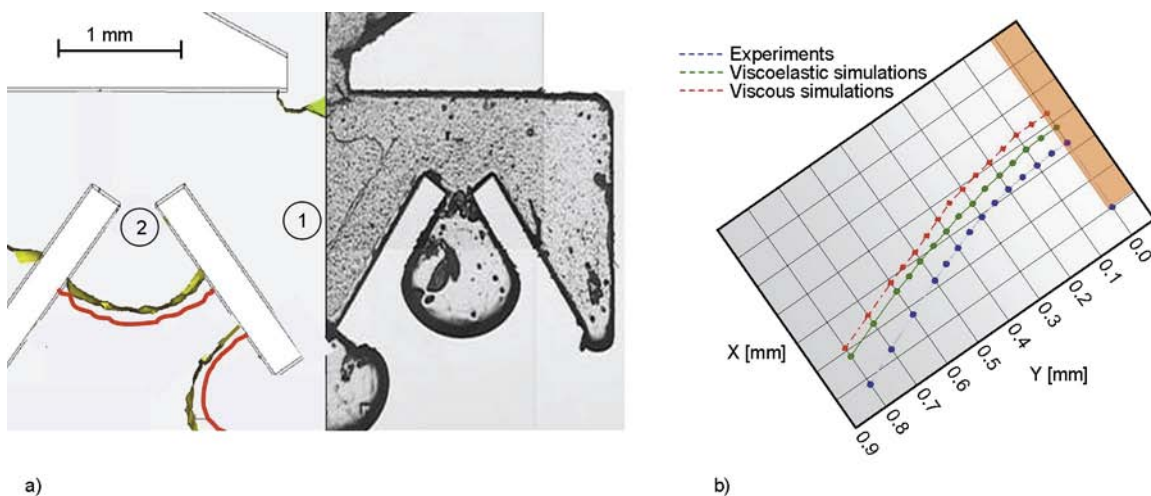


Figure 10. Streamlines at 1.2 ms (a) and subsequent weld line formation (b)

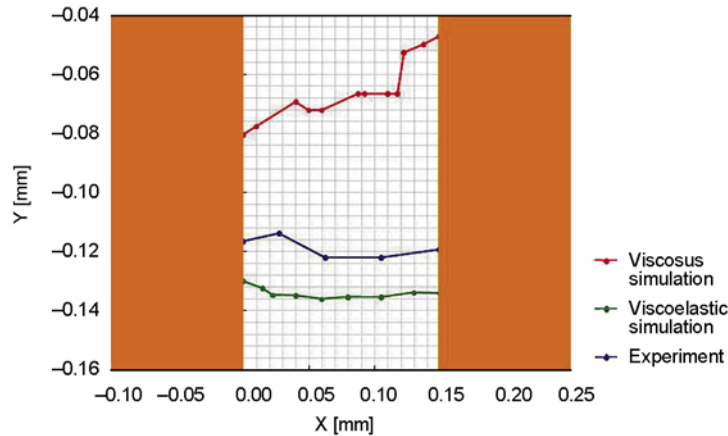


Figure 11. Line 1 of the weld line number 3

ference may be justified considering geometrical constraints and the viscoelastic nature of the polymer itself. Normal stresses and resistance to elongational deformation reduce the filling length in the micro channel. This effect is not as clear as in the other channels with higher dimensions, because as the channel dimensions decrease the material appears to be more rigid due to the constraints at the wall.

Differences between numerical and experimental results may be related to inadequate boundary conditions. No-slip conditions were imposed on the cavity walls filled by the polymer whereas wall slip is expected to occur due to the increased shear stress. A complete validation of the approach will be possible when more reliable models about local viscosity and heat transfer will be available.

6. Conclusions

In this paper a new approach, which employs weld lines as flow markers, is used to evaluate whether the commercially available numerical codes are suitable to characterize the melt flow patterns in the micro moulding process. A micro cavity was designed and manufactured in order to create an effective response variable to compare the results of numerical simulations and experiments. Conventional three dimensional simulations were tested and found to be inappropriate for multi-scale structures, typically in micro-injection moulded parts. It was expected that differences between experiments and numerical investigations would be due to the assumption of a generalized Newtonian fluid, generally used for traditional injection moulding, where

the importance of the material elasticity compared to viscous effects appears to be negligible. Because of high deformation rates during the injection phase, it was expected that viscoelastic effects might occur.

Careful material characterization was conducted by means of both capillary and rotational rheometry and data obtained were fitted according to a non linear viscoelastic model (Giesekus model). Three dimensional viscoelastic numerical simulations were then performed to evaluate whether the implementation of a viscoelastic material model could improve the accuracy of micro filling simulations. Improvements in the viscoelastic simulation results were observed in predicting the weld lines position. Further differences between experiments and numerical simulations are to be related to the absence of a robust local heat transfer model.

References

- [1] Ho C-M., Tay Y-C.: Micro-electro-mechanical-systems (MEMS) and fluid flows. *Annual Review of Fluid Mechanics*, **30**, 579–612 (1998). DOI: [10.1146/annurev.fluid.30.1.579](https://doi.org/10.1146/annurev.fluid.30.1.579)
- [2] Kemmann O., Weber L., Jeggy C., Magotte O., Dupret F.: Simulation of the micro injection molding process. in 'Proceedings of SPE Annual Technical Conference – ANTEC 2000. Orlando, Florida, USA' 576-580 (2000).
- [3] Chien R-D., Jong W-R., Chen S-C.: Study on rheological behavior of polymer melt flowing through micro-channels considering the wall-slip effect. *Journal of Micromechanics and Microengineering*, **15**, 1389–1396 (2005). DOI: [10.1088/0960-1317/15/8/003](https://doi.org/10.1088/0960-1317/15/8/003)

- [4] Yu L., Koh C. G., Lee L. J., Koelling K. W., Madou M. J.: Experimental investigation and numerical simulation of injection molding with micro-features. *Polymer Engineering and Science*, **42**, 871–888 (2002).
DOI: [10.1002/pen.10998](https://doi.org/10.1002/pen.10998)
- [5] Peters G. W. M., Schoonen J. F. M., Baaijens F. P. T., Meijer H. E. H.: On the performance of enhanced constitutive models for polymer melts in a cross-slot flow. *Journal of Non-Newtonian Fluid Mechanics*, **82**, 387–427 (1999).
DOI: [10.1016/S0377-0257\(98\)00173-6](https://doi.org/10.1016/S0377-0257(98)00173-6)
- [6] Larson R. G.: A critical comparison of constitutive equations for polymer melts. *Journal of Non-Newtonian Fluid Mechanics*, **23**, 249–269 (1987).
DOI: [10.1016/0377-0257\(87\)80021-6](https://doi.org/10.1016/0377-0257(87)80021-6)
- [7] Gava A., Tosello G., Hansen H. N., Salvador M., Lucchetta G.: A new approach for the validation of filling simulations in micro injection moulding. in ‘Proceedings of the 9th International Conference on Numerical Methods in Industrial Forming Processes – NUMIFORM, Porto, Portugal’ 307–312 (2007).
DOI: [10.1063/1.2740829](https://doi.org/10.1063/1.2740829)
- [8] Cardinaels R., Van Puyvelde P., Moldenaers P.: Evaluation and comparison of routes to obtain pressure coefficients from high-pressure capillary rheometry data. *Rheologica Acta*, **46**, 495–505 (2007).
DOI: [10.1007/s00397-006-0148-5](https://doi.org/10.1007/s00397-006-0148-5)
- [9] Macosko C. W.: *Rheology: Principles, measurements and applications*. Wiley-VCH, New York (1994).
- [10] Ferry J. D.: *Viscoelastic properties of polymers*. Wiley, New York (1980).
- [11] Giesekus H.: A simple constitutive equation for polymer fluids based on the concept of deformation-dependent tensorial mobility. *Journal of Non-Newtonian Fluid Mechanics*, **11**, 69–109 (1982).
- [12] Armstrong R. C., Brown R. A., Quinzani L. M., McKinley G. H., Byars J. A.: Measurement of velocity and stress fields in complex polymer flows. in ‘Proceedings of the XI International Congress on Rheology, Brussels, Belgium’ 16–23 (1992).

Molecular composition and properties of impact propylene copolymers

A. J. van Reenen*, N. C. Basson

Department of Chemistry and Polymer Science, University of Stellenbosch, Provate Bag X1, 7602 Matieland, South Africa

Received 30 August 2011; accepted in revised form 12 December 2011

Abstract. Impact polypropylene copolymers (IPCs) are important commercial materials, but their morphology and molecular architecture are not yet fully understood. In this study the focus was on selectively removing specific fractions from the original IPC, recombining the remaining fractions, and studying the properties and morphology of these recombined polymers. It was found that some properties of the samples changed remarkably, depending on the fraction of material that was removed before recombination. In a similar fashion, morphological changes could be observed. For example, the degree of phase separation and the crystalline morphology of the recombined materials varied noticeably. It was further established that specific copolymer fractions present in the original polymer affect not only the morphology of the final polymer, but also the hardness and impact resistance.

Keywords: mechanical properties, impact propylene copolymers, temperature rising elution fractionation, molecular composition, morphology

1. Introduction

The complex nature of impact propylene copolymers (IPCs) is well documented. Due to the complex nature of the polymer, it is not that easy to understand the relationship between the molecular structure and the physical (macroscopic) properties of the polymers in question.

Numerous groups have studied the polymerization kinetics and morphological development of polypropylene (PP) with solid catalysts. This relates to the final product obtained during the preparation of IPCs, as the first phase comprises the preparation of an isotactic polypropylene (iPP) matrix. The iPP particles comprise agglomerated granules that are, in turn, made up of microparticles that are bound together [1–11]. Between the microparticles there are sub-micron sized pores, while micron-sized pores are present between the granules. By contrast,

only a handful of papers on the morphology or kinetics of IPCs have appeared in the open literature. Examples are those of Kakugo *et al.* [12], and Simonazzi *et al.* [13]. An excellent, independent study was conducted at the University of Wisconsin-Madison, and reported by Debling and Ray [14]. Additional papers that deal with the morphology of the IPCs are those by McKenna and coworkers [15, 16] and Urdamilleta *et al.* [16]. From the available literature it is quite clear that the morphology of the ‘as-polymerized’ reactor powders is quite different from the morphology that is obtained after the first processing step [17]. This is an aspect of the morphological and chemical composition development that still needs more investigation, but one that is not dealt with in this paper. It can, in general, be concluded that the preparation of an IPC comprises, after the preparation of the iPP phase as

*Corresponding author, e-mail: ajvr@sun.ac.za
© BME-PT

microparticles, the formation of a ‘copolymer phase’, which comprises rubbery as well as crystalline materials. This copolymer phase is not trapped inside the microparticles, but flows into the sub-micron pores and into the larger pores between the granules. The extent of this migration depends on both the nature of the copolymer phase (molecular weight and molecular weight distribution) and the chemical composition distribution of the copolymer phase. The chemical composition aspect is one which will, *inter alia*, determine whether or not there is some ‘compatibilization’ between the iPP matrix and the rubbery phase at work [18, 19]. There have been a number of papers on morphology of physical blends of iPP with other polymers [20–25], as well as the macroscopic relationship between structure and property of the IPCs, and it is clear that the impact properties of these polymers are influenced by the size and distribution of the rubber particles in the polymer after processing [26–34]. The final morphology of the polymer can also be influenced by processing parameters [35–38].

In our view, there is still a lack of fundamental understanding of how the molecular composition of the polymer influences the macroscopic properties of the IPCs. In this paper we report the results of a study where we selectively removed fractions of a commercial IPC and studied the effect thereof on the morphology and selected properties of the IPCs. We did not investigate the relationship between the morphology of the reactor powders and the final morphology of the processed polymer; that is in fact part of an on-going investigation. We have in the past successfully fractionated commercial polyolefins by preparative temperature rising elution fractionation (prep-TREF) [39, 40]. We therefore applied prep-TREF to a commercial IPC and selectively removed fractions of the polymer before recombining the rest of the material for analysis and testing.

2. Experimental section

The equipment used for the preparative TREF experiments was designed and built in-house [36]. The polymer (3 g of propylene impact copolymer CMR 648, Sasol Polymers, Secunda, South Africa, ethylene content 14.87%) was dissolved in 300 mL xylene (Technical grade, KIMIX Chemicals, Epping, South Africa) at 135°C. Stabilizer (2% w/w mixture

of Irganox1010 and Irgafos168, supplied by Sasol Polymers, Modderfontein, South Africa) added to limit degradation. After complete dissolution the polymer solution was added to pre-heated sand (–50+70 mesh grade of Silica Sand, Sigma Aldrich, Munich, Germany) in a 1L reactor. The sand/polymer solution mixture was then cooled at 1°C/hour from 130 to 25°C. The sand was separated from the solvent, and the polymer remaining in solution isolated by removing the solvent under reduced pressure. This was denoted the 25°C fraction. Further fractions were collected in the second step at given temperature intervals (40, 60, 80, 90, 100, 110, 120, 130 and 140°C) by eluting the polymer from the sand with xylene at the required temperature. Polymer fractions were isolated by precipitation with acetone and drying under reduced pressure.

A reference material was prepared (E-REF) by recombining all the fractions from a prep-TREF experiment. In a series of other experiments, one fraction was removed from the material isolated from the prep-TREF experiment and the rest of the fractions recombined. The notations for all the materials prepared in this fashion are presented in Table 1. For further analyses, samples were prepared by injection moulding disks (Haake Minijet II, Thermo Scientific, USA). These disks were used for hardness measurements, DMA analyses, DSC analyses and ¹³C NMR spectroscopy in selected cases. Sections of the disks were used for SEM analyses (surface analyses only) and small sections were used to anneal samples in the DSC prior to microtoming, staining and TEM analyses. It needs to be pointed out that roughly 3–4 g was used in each TREF experiment, so the amount of material that could be obtained after fraction removal and recombination was very limited. This obviously also limits the amount of physical testing that was possible, and as such tensile tests, impact toughness etc could not be conducted.

The bulk and the recombined materials, as well as the fractions obtained from TREF experiments were fully characterized by ¹³C NMR, DSC, high-temperature SEC.

High temperature ¹³C NMR analyses were done on a Varian Unity Inova, 600 MHz NMR spectrometer, with 1,1,2,2-tetrachloroethane *d*₂, (Sigma Aldrich, Munich, Germany) as solvent.

Molecular weight determinations were done with a PL-GPC 220 high-temperature chromatograph (Varian Polymer Laboratories, USA), measurements were performed at 160°C (1, 2, 4 trichlorobenzene stabilized with 0.0125% 2, 6-di-tert-butyl-4-methylphenol (BHT)) at a flow rate of 1 mL/min⁻¹. Columns were packed with a polystyrene/divinylbenzene copolymer (PL gel MIXED-B [9003-53-6]) from Varian Polymer Laboratories.

Morphology was studied by both transmission electron microscopy (TEM) and scanning electron microscopy (SEM). A Reichert Ultracut S microtome were used to prepare samples (previously annealed in the DSC) for TEM (Leo[®] 912 TEM). Ruthenium (III) chloride hydrate powder (Merck Chemicals, Darmstadt, Germany), were used to prepare a ruthenium oxide vapour to stain the samples prior to the TEM analyses. A Leo[®] 1430VP Scanning Electron Microscope was used to do the SEM analysis on the samples, with sample disks being prepared by injection moulding (Haake Mini-jet II, Thermo Scientific, USA). Thermal analyses were conducted using a Q100 DSC, (TA Instruments, New Castle, USA). The DSC was also used to perform isothermal heat treatment for selected samples before TEM analyses.

DMA analyses were conducted using a Perkin Elmer 7e DMA (Perkin Elmer, Waltham, USA). Samples were cooled to -80°C and then heated to 140°C. The heating rate was 5°C/min and a nitrogen purge gas with a flow rate of 28.0 mL/min was used. The static force used was 110 mN, with a static force tension of 120%. The dynamic force was 100 mN, the amplitude 10.0 µm, and the frequency 1.00 Hz.

Hardness values were determined using a UHL type VMH-002 microhardness tester (AMS Laboratory Technologies, Cape Town, South Africa), using an indentation load of 10 gf (0.01 N), an indentation speed of 25 µm/s and a dwell time of 15 seconds for each sample. An average of 10 measurements was used.

3. Results

A typical prep-TREF profile is presented in Figure 1.

It is clear that about 25% of the material remains soluble at room temperature (25°C fraction). About half the polymer sample elutes at 110 and 120°C.

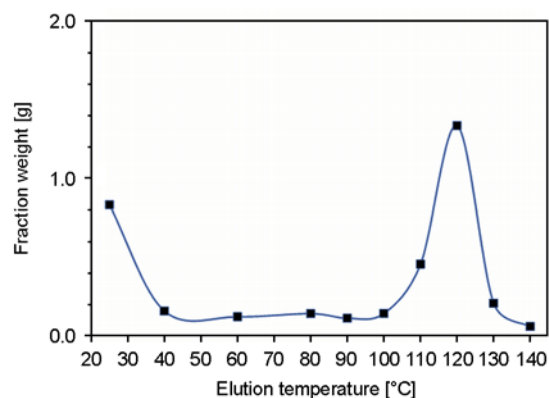


Figure 1. A typical p-TREF profile of the impact copolymer

The soluble part of the polymer is normally assumed to be rubbery and non-crystalline in nature, while the fractions eluting at the higher temperatures are more highly crystalline. The fractions of the material that elute in the range 40 to 80°C are less crystalline than those that elute at higher temperatures, and are regarded as being propylene/ethylene copolymers of limited crystallinity.

The overall contribution of these so-called copolymer fractions to the total weight of the polymer is between 15 and 20%, 50–60 % by weight is crystalline iPP and 25% is soluble, rubbery material, possibly non-crystallisable PP-PE copolymers, or low molecular weight isotactic PP and EPR rubber. For the purpose of this study, we decided to take each the fractions of each TREF run, remove a specific fraction and then to recombine the rest of the material. The fractions that were to be removed were the 25°C fraction, the copolymer fractions at which elute at 60, 80 and 90°C, and the 100, 110 and 120°C fractions, which comprise mostly the iPP matrix of the impact copolymer. Of real interest to us was the effect that removing the copolymer fractions would have on the properties of the resultant recombined materials. For practical purposes the polypropylene matrix (crystalline fractions) and the rubbery material need to be present, as these fractions give the material its main properties.

The overview of the properties of some of the fractions (as an example of a typical TREF run) are shown in Table 1. Due to limited amounts of material, full characterization by ¹³C NMR was not possible for all the fractions.

As was expected, most of the ethylene is present in the soluble (25°C) and the copolymer fractions (60 and 80°C). Also of interest here is the wide molecu-

Table 1. Characterization data for selected fractions obtained by prep-TREF

TREF fraction	M _w	PD	Ethylene content ¹ [mole%]	Fraction weight [g]	Ethylene in fraction ² [w% of total]	T _m [°C]	X _c ³ [%]
25°C	123 902	1.85	38.9	0.8268	82.00		
60°C	73 914	1.70	34.1	0.1175	10.30	86.3	1.85
80°C	112 201	4.33	20.3	0.1375	6.67	104.6	12.1
90°C	211 376	10.0	4.49	0.1083	1.03	144.6	35.7
100°C	168 959	7.15	n/d	0.1384	n/d	154.0	49.8
110°C	93 841	2.13	n/d	0.4521	n/d	154.2	59.2
120°C	246 752	2.81	n/d	1.3309	n/d	161.4	66.9

¹Determined by ¹³C NMR; ²Determined as weight% of the total amount of ethylene present in the 25, 60, 80 and 90°C fractions, ³calculated from DSC compared to perfectly crystalline PP. n/d Not detected

lar weight distribution in the copolymer fractions (4.3–10). It must be noted that the ethylene content is given as a concentration, and that one needs to take into account the size of the fractions that were analyzed in order to get a complete picture of the distribution of ethylene in the copolymer, and whilst the 40°C fraction is not considered here, the distribution of the ethylene that we did analyze is also shown in Table 2, where it is displayed as a percentage of the whole. From this it is quite clear that almost all the ethylene is in the soluble (25°C) fraction. It must also be noted that the ethylene content quoted is determined by ¹³C NMR, and does not distinguish between the molecular species where the ethylene is found. There are distinct differences between the spectra of the 25 and the 60°C fractions, for example (Figures 2a and b). See for example here the area indicated by the rectangle on the spectra. The peaks in this area relate mostly to different configurations of ethylene and propylene units occurring in copolymers of the two monomers. The peak assignments for the ¹³C NMR spectra are

given in Table 3. These assignments were made according to literature [41–45]. Assignments for the methylene carbons in Table 3 are identified by the letter *S* and a pair of Greek letters that indicate its distance in both directions from the nearest tertiary carbons. A methyl carbon is identified by the letter *M* and a tertiary carbon is labelled by the letter *T*. The monomer sequence type is indicated in right-hand column of Table 3 (*P* = propylene, *E* = ethylene). Table 2 gives a summary of the materials that were created by fractionation, fraction removal and recombination. The reference material (denoted E-REF) was the material containing all the TREF fractions (no fractions removed).

In general the trends in terms of crystallization temperature, melting point and crystallinity is what is expected considering the nature of the material that was removed, but what is interesting is appearance of two crystallization peaks when we remove some of the more crystalline material (Less 90C, Less 110C and Less 120C). In this instance, the Less 90C material is of the most interest to us, as

Table 2. Selected data for the materials prepared by fraction removal and recombination

Polymer	TREF fraction removed	Material removed [%]	M _w	PD	T _c [°C]	T _m [°C]	X _c ² [%]
E-REF	None		252 971	4.06	116.26	160.54	49.89
Less 25C	25°C	27.50	140 850	2.45	114.92	159.33	54.85
	40°C ²	4.36	–	–			
Less 60C	60°C	3.33	173 536	2.63	114.90	159.60	54.79
Less 80C	80°C	3.90	157 116	2.49	113.36	159.79	43.28
Less 90C	90°C	3.07	165 685	2.33	106.5/109.8 ³	148.70	35.20
Less 100C	100°C	3.93	163 587	2.53			40.62
Less 110C	110°C	12.83	117 200	2.31	105.6/110.1 ³	149.30	37.40
Less 120C	120°C	37.77	202 950	2.98	107.1/111.6 ³	149.30	23.10
	130°C ¹	5.76	–				
	140°C ¹	1.58					

¹These fractions were not removed to create recombined materials. ²Determined by DSC, relative to 100% crystalline PP. ³2 crystallization peaks observed.

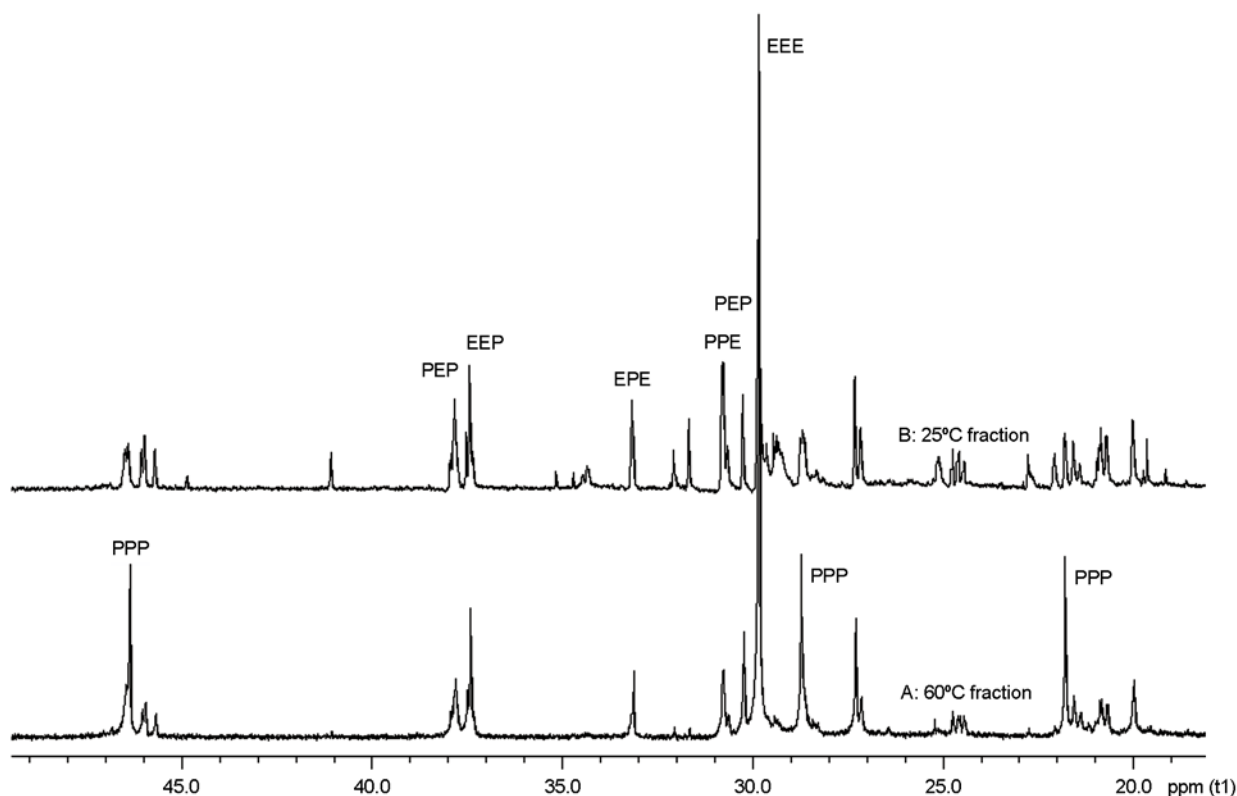


Figure 2. The ^{13}C NMR spectra of the 60°C (lower curve) and the 25°C (upper curve) fraction obtained by p-TREF. Monomer sequences are indicated on the spectra.

the more crystalline fractions constitute the bulk of the material, and as such cannot be removed without altering the nature of the material significantly. Using the values presented in Table 3 and the spectra presented in Figure 2, we can see that, for example the 60°C prep-TREF fraction shows that the ratio of the EEP:PEP peaks at around 37–38 ppm is different to that of the 25°C fraction. Similarly the presence of the peaks associated with PP homopolymer (20.5–21., 27.5–28.7 and 45–46 ppm) is much more evident in the 60°C fraction. This illustrates the difference in chemical composition distribution of a partially crystalline fraction and the soluble fraction.

The mechanical properties of the materials are presented in Figures 3 and 4. Figure 3 gives the hardness values for the materials. The hardness of the reference material is given in the bar on the left. The values are given as relative hardness values (HV) and are derived by the instrument.

It is quite obvious that removing the rubbery, soluble material completely leads to a large increase in hardness (Less 25C sample), but this is expected and has little practical significance, as the rubbery material is an essential part of the material. The

Table 3. ^{13}C NMR assignments for propylene and ethylene sequences in IPCs

Assignment	Chemical shifts [ppm]	Sequence type
$S_{\alpha\alpha}$	45.14–46.32	PPP
$S_{\alpha\gamma}$	37.70–37.90	PEP
$S_{\alpha\delta}$	37.08–37.70	EEP
$T_{\delta\delta}$	33.03–33.20	EPE
$T_{\beta\delta}$	30.40–30.78	PPE
$S_{\gamma\delta}$	30.00–30.31	PEP
$S_{\delta\delta}$	28.61–29.79	EEE
$T_{\beta\beta}$	27.49–28.66	PPP
$S_{\beta\beta}$	27.20–27.40	PEP
$M_{\beta\beta}$	20.45–21.58	PPP
$M_{\beta\gamma}$	20.60–20.98	PPE
$M_{\gamma\gamma}$	19.90–20.70	PEP

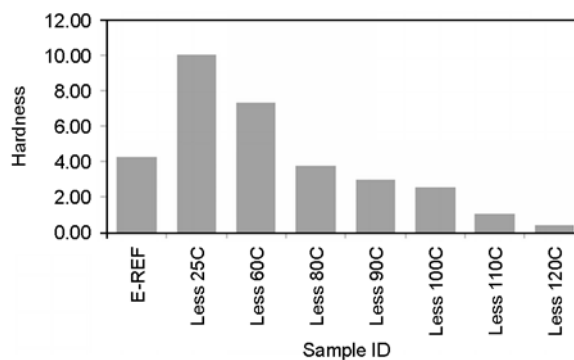


Figure 3. The microhardness values (HV) for the reference material and the recombined polymers

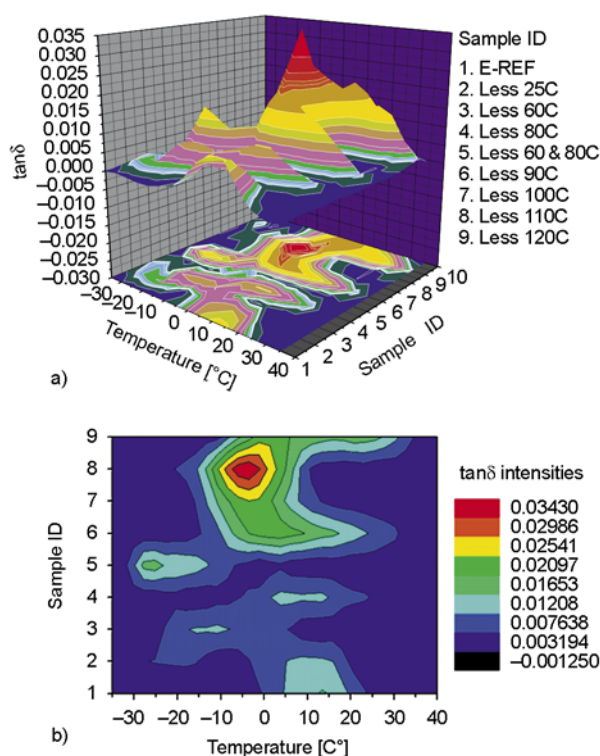


Figure 4. (a) The 3D map of the $\tan \delta$ data of the recombined materials, (b) the 2D projection map of the 3D plot of the $\tan \delta$ values of samples

same is true for removing the 60°C fraction, as this is essentially also rubbery material, but with some crystalline material present. Of real interest is that we can remove the 80 and 90°C fractions and still maintain hardness values that are similar to that of the reference material. This is particularly interesting if we take into consideration the DMA results.

The DMA results are presented in Figure 4. In order to relate these results to the impact resistance of the polymers we used the size (area under the curve) and peak position of the $\tan \delta$ peaks for the reference material and the recombined polymers to give a 3D plot (Figure 4a) as well as a 2D projection of the 3D plot of the same data (Figure 4b).

Figures 4a and 4b shows how the T_g ($\tan \delta$) transition regions shift from the one sample to the next, and also clearly maps the broadness and separation of the samples. From the top down of the map in Figure 4b we can see that removing the crystalline materials leads to an increase in the intensity of the $\tan \delta$ transition, without significantly altering the position of the transition. This is to be expected, as removing the crystalline material should have that effect. Removing most of the polymer is, however, of little practical significance, and in this regard we

find the effect of removing the 60 to 90°C fractions (sample ID 3-6) significant. We can see real changes in the position and number of $\tan \delta$ peaks, which indicates that these fractions play a significant role in the final morphology of the polymer in question. It appears as if the removal of the copolymer fractions influences the degree of phase separation between the more rubbery material and the crystalline iPP matrix. In the case where the 60°C prep-TREF fraction is removed, the $\tan \delta$ peak moves to a significantly lower value, and the entire transition becomes much broader. The $\tan \delta$ peak value moves closer to the expected T_g value for EPR rubber, which would be in the region of -30 to -40°C. This indicates that there is now a significant phase separation between the iPP matrix and the rubbery EPR phase. The broadness of the transition (-30 to 8°C) also suggests that the DMA shows that this peak is due to both the EPR phase as well as the iPP phase. If the 80°C prep-TREF fraction is removed the $\tan \delta$ peak moves back to around the same value of the reference material. This indicates that this molecular fraction does not influence the phase behaviour of the EPR fraction to the same extent as the 60°C fraction. When both the 60 and 80°C are removed (sample ID 5) there is significant phase separation, with a well-developed $\tan \delta$ peak at around -30°C. Whilst these changes do necessarily represent measurable changes in physical properties, they do represent changes in morphology, which could conceivably be related to changes in impact behaviour of the polymer in question. If this is taken in conjunction with the hardness values, we can see that we can affect the hardness properties without adversely affecting the (as evidenced by the DMA data) impact properties of the polymer, particularly in the case of removing the 60 and 80°C fractions individually or together (sample ID 5). These two fractions represent about 7% of the total of the polymer.

In order to correlate the mechanical and chemical analyses of the materials with the morphology, we conducted SEM and TEM analyses. Some selected results are presented in Figures 5a–c and 6a–c.

The SEM micrographs show the rubbery particles present as small white bumps in the reference material (Figure 5a). For the Less 60C and Less 80C samples we see crevices in the surface of the material (Figures 5b and 5c. The crevices appear larger for the sample where the 60°C prep-TREF fraction

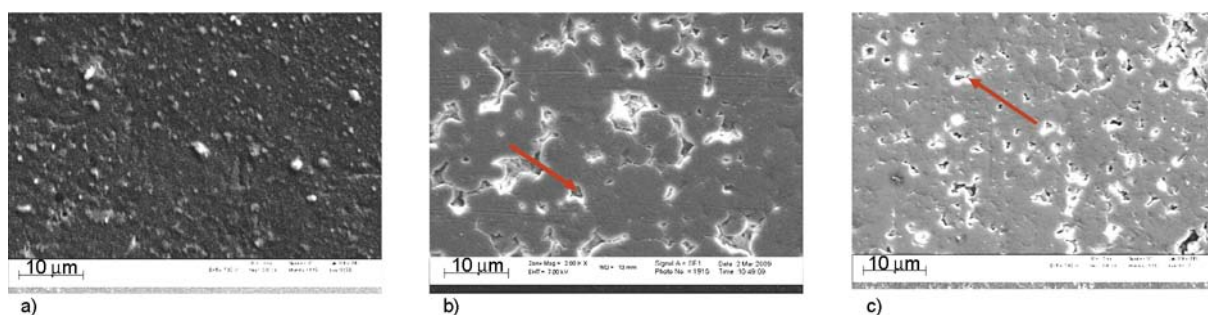


Figure 5. SEM micrographs (2000× magnification) of (a) E-REF, (b) Less 60C and (c) Less 80C. The arrows indicate crevices. Scale bar is 10 μm.

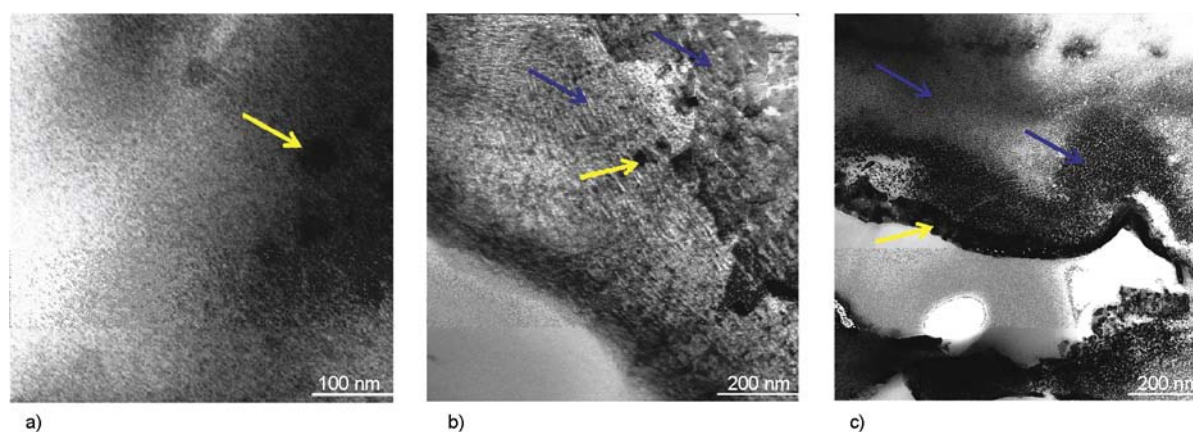


Figure 6. TEM micrographs of (a) E-REF, (b) Less 60C and (c) Less 80C. Polymers were isothermally crystallized and stained. Darker areas indicate more amorphous materials. Dark arrows indicate crystalline structures while the light arrows indicate rubbery particles.

was removed. This indicates phase separation on the molecular scale. The TEM micrographs of samples that were isothermally crystallized indicated phase separation on a completely different scale to the SEM images. Here the rubbery particles are about 20–30 nm in diameter, which indicates the way that phase separation occurs also at a much smaller scale than can be seen in the SEM micro-

graphs. What interested us here was the apparent phase separation amongst crystalline regions in the copolymer.

In Figure 6a the reference material quite clearly shows small amorphous, rubbery inclusions spread through the more crystalline matrix. Where copolymer fractions have been removed, the isothermally crystallized fractions clearly show a distinct phase

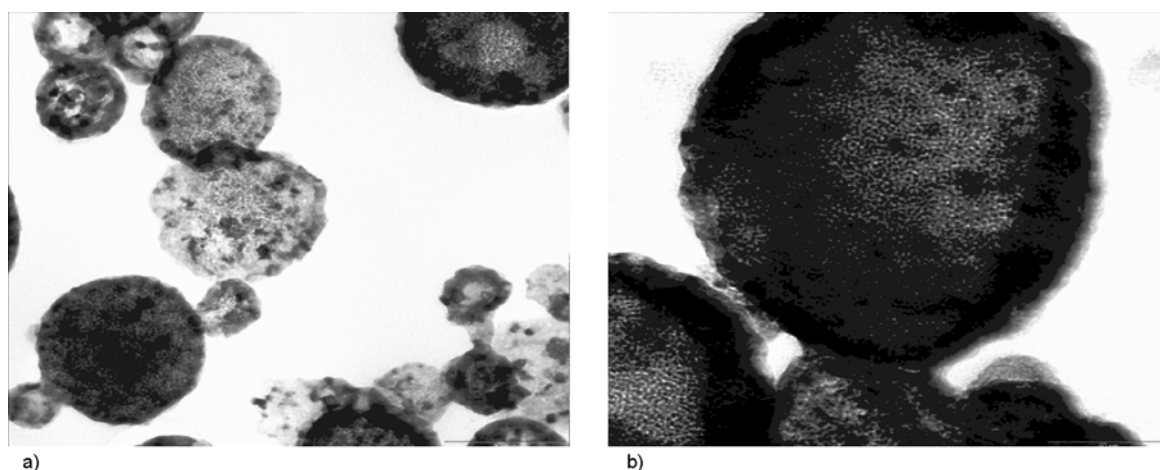


Figure 7. TEM micrograph of the Less 110C material (a) scale bar = 100 nm, (b) scale bar = 50 nm

separation between different crystalline phases (dark arrows in Figures 6b and c), as well as distinctly separate rubbery segments (Figure 6c), indicated by the light arrows. In Figure 6c, in particular, we see a complete segregation of the rubber particles and two distinct crystalline phases. These TEM micrographs clearly show that the copolymer fractions play a role not only as compatibilizers between the more rubbery and the more crystalline areas in the impact copolymer, but also between materials of differing crystallizability. For interest's sake, we also include a TEM micrograph of the Less 110C material, where a significant amount of the crystalline material was removed before recombination (Figure 7).

In Figure 7 we can see that we now have structures that almost resemble 'core-shell' particles, where there appears to be crystalline material encapsulated in a rubber matrix.

4. Conclusions

Overall, it was found that removing fractions and recombining material led to significant changes in morphology (as observed by SEM and TEM), as well as mechanical properties. The IPC materials are designed to be impact resistant materials that retain their temperature resistance and strength properties of the parent iPP, so removal of the EPR phase and the highly crystalline phase of the polymer are academically interesting, but of little practical significance. It is therefore the effect of the removal of the copolymer fractions (constitutes 20–25% of the overall polymer material) that is of the most interest from a practical standpoint. It is quite clear that the effect of removing those fractions that were isolated by TREF at 60, 80 and 90 °C could have practical implications. These copolymer fractions clearly influence the phase-separation behaviour of the material significantly. It therefore appears that we could alter the hardness/impact balance of this particular copolymer by subtle alterations to those molecular species present in the copolymer that elute in the 60 to 80 °C range during TREF separation.

Results of TEM studies on the isothermally crystallized samples were quite revealing. A staining regimen was developed that allowed us to see distinct phase differences on the samples analyzed. Removal of the copolymer fractions could be seen to have

significant effects on the morphology of the samples, and clear phase boundaries could be seen in the absence of these fractions.

Acknowledgements

The authors gratefully acknowledge funding from the National Research Foundation of South Africa, as well as Sasol Polymers, South Africa for funding and materials donated.

References

- [1] Rincon-Rubio L. M., Wilen C-E., Lindfors L-E.: A kinetic model for the polymerization of propylene over a Ziegler-Natta catalyst. *European Polymer Journal*, **26**, 171–176 (1990).
DOI: [10.1016/0014-3057\(90\)90183-5](https://doi.org/10.1016/0014-3057(90)90183-5)
- [2] Tait P., Jaber I., Loontjens A.: Studies on the polymerization of propylene using highly active magnesium chloride supported Ziegler-Natta catalysts: Effects of alkyl concentration on the polymerization rate and on the active centre concentration. *Studies in Surface Science and Catalysis*, **56**, 11–27 (1990).
DOI: [10.1016/S0167-2991\(08\)61613-4](https://doi.org/10.1016/S0167-2991(08)61613-4)
- [3] Bukatov G. D., Zaikovskii V. I., Zakharov V. A., Kryukova G. N., Fenelonov V. B., Zagrafskaya R. V.: The morphology of polypropylene granules and its link with the titanium trichloride texture. *Polymer Science in the U.S.S.R.*, **23**, 599–606 (1982).
DOI: [10.1016/0032-3950\(82\)90049-1](https://doi.org/10.1016/0032-3950(82)90049-1)
- [4] Ferrero M. A., Sommer R., Spanne P., Jones K. W., Conner W. C.: X-ray microtomography studies of nascent polyolefin particles polymerized over magnesium chloride-supported catalysts. *Journal of Polymer Science A: Polymer Chemistry*, **31**, 2507–2512 (1993).
DOI: [10.1002/pola.1993.080311011](https://doi.org/10.1002/pola.1993.080311011)
- [5] Galli P., Haylock J. C.: Continuing initiator system developments provide a new horizon for polyolefin quality and properties. *Progress in Polymer Science*, **16**, 443–462 (1991).
DOI: [10.1016/0079-6700\(91\)90025-G](https://doi.org/10.1016/0079-6700(91)90025-G)
- [6] Hock C. W.: How TiCl₃ catalysts control the texture of as-polymerized polypropylene. *Journal of Polymer Science Part A-1: Polymer Chemistry*, **4**, 3055–3064 (1966).
DOI: [10.1002/pol.1966.150041212](https://doi.org/10.1002/pol.1966.150041212)
- [7] Kakugo M., Sadatoshi H., Yokoyama M., Kojima K.: Transmission electron microscopic observation of nascent polypropylene particles using a new staining method. *Macromolecules*, **22**, 547–551 (1989).
DOI: [10.1021/ma00192a006](https://doi.org/10.1021/ma00192a006)
- [8] Kakugo M., Sadatoshi H., Sakai J., Yokoyama M.: Growth of polypropylene particles in heterogeneous Ziegler-Natta polymerization. *Macromolecules*, **22**, 3172–3177 (1989).
DOI: [10.1021/ma00197a046](https://doi.org/10.1021/ma00197a046)

- [9] Noristi L., Marchetti E., Baruzzi G., Sgarzi P.: Investigation on the particle growth mechanism in propylene polymerization with MgCl₂-supported Ziegler–Natta catalysts. *Journal of Polymer Science Part A: Polymer Chemistry*, **32**, 3047–3059 (1994).
DOI: [10.1002/pola.1994.080321606](https://doi.org/10.1002/pola.1994.080321606)
- [10] Wristers J.: Nascent polypropylene morphology: Polymer fiber. *Journal of Polymer Science: Polymer Physics Edition*, **11**, 1601–1617 (1973).
DOI: [10.1002/pol.1973.180110809](https://doi.org/10.1002/pol.1973.180110809)
- [11] Wristers J.: Direct examination of polymerization catalyst by electron scanning microscopy. *Journal of Polymer Science: Polymer Physics Edition*, **11**, 1619–1629 (1973).
DOI: [10.1002/pol.1973.180110810](https://doi.org/10.1002/pol.1973.180110810)
- [12] Kakugo M., Sadatoshi H., Sakai J.: Morphology of nascent polypropylene produced by MgCl₂ supported Ti catalyst. *Studies in Surface Science and Catalysis*, **56**, 345–354 (1990).
DOI: [10.1016/S0167-2991\(08\)61638-9](https://doi.org/10.1016/S0167-2991(08)61638-9)
- [13] Simonazzi T., Cecchin G., Mazzullo S.: An outlook on progress in polypropylene-based polymer technology. *Progress in Polymer Science*, **16**, 303–329 (1991).
DOI: [10.1016/0079-6700\(91\)90021-C](https://doi.org/10.1016/0079-6700(91)90021-C)
- [14] Debling J. A., Ray W. H.: Morphological development of impact polypropylene produced in gas phase with a TiCl₄/MgCl₂ catalyst. *Journal of Applied Polymer Science*, **81**, 3085–3106 (2001).
DOI: [10.1002/app.1761](https://doi.org/10.1002/app.1761)
- [15] McKenna T. F., Bouzid D., Matsunami S., Sugano T.: Evolution of particle morphology during polymerisation of high impact polypropylene. *Polymer Reaction Engineering*, **11**, 177–197 (2003).
DOI: [10.1081/PRE-120021074](https://doi.org/10.1081/PRE-120021074)
- [16] Bouzid D., Gaboriaud F., McKenna T. F.: Atomic force microscopy as a tool to study the distribution of rubber in high impact poly(propylene) particles. *Macromolecular Materials and Engineering*, **290**, 565–572 (2005).
DOI: [10.1002/mame.200400248](https://doi.org/10.1002/mame.200400248)
- [17] Urdampilleta I., González A., Iruin J. J., de la Cal J. C., Asua J. M.: Morphology of high impact polypropylene particles. *Macromolecules*, **38**, 2795–2801 (2005).
DOI: [10.1021/ma047413v](https://doi.org/10.1021/ma047413v)
- [18] Fan Z-Q., Zhang Y-Q., Xu J-T., Wang H-T., Feng L-X.: Structure and properties of polypropylene/poly(ethylene-co-propylene) in-situ blends synthesized by spherical Ziegler–Natta catalyst. *Polymer*, **42**, 5559–5566 (2001).
DOI: [10.1016/S0032-3861\(01\)00062-3](https://doi.org/10.1016/S0032-3861(01)00062-3)
- [19] Cai H., Luo X., Chen X., Ma D., Wang J., Tan H.: Structure and properties of impact copolymer polypropylene. II. Phase structure and crystalline morphology. *Journal of Applied Polymer Science*, **71**, 103–113 (1999).
DOI: [10.1002/\(SICI\)1097-4628\(19990103\)71:1<103::AID-APP13>3.0.CO;2-5](https://doi.org/10.1002/(SICI)1097-4628(19990103)71:1<103::AID-APP13>3.0.CO;2-5)
- [20] Yang D., Zhang B., Yang Y., Fang Z., Sun G., Feng Z.: Morphology and properties of blends of polypropylene with ethylene-propylene rubber. *Polymer Engineering and Science*, **24**, 612–617 (1984).
DOI: [10.1002/pen.760240814](https://doi.org/10.1002/pen.760240814)
- [21] Jang B. Z., Uhlmann D. R., Vander Sande J. B.: Rubber-toughening in polypropylene. *Journal of Applied Polymer Science*, **30**, 2485–2504 (1985).
DOI: [10.1002/app.1985.070300617](https://doi.org/10.1002/app.1985.070300617)
- [22] van Gisbergen J. G. M., Meijer H. E. H., Lemstra P. J.: Structured polymer blends: 2. Processing of polypropylene/EDPM blends: Controlled rheology and morphology fixation via electron beam irradiation. *Polymer*, **30**, 2153–2157 (1989).
DOI: [10.1016/0032-3861\(89\)90241-3](https://doi.org/10.1016/0032-3861(89)90241-3)
- [23] Choudhary V., Varma H. S., Varma I. K.: Polyolefin blends: Effect of EPDM rubber on crystallization, morphology and mechanical properties of polypropylene/EPDM blends. 1. *Polymer*, **32**, 2534–2540 (1991).
DOI: [10.1016/0032-3861\(91\)90332-D](https://doi.org/10.1016/0032-3861(91)90332-D)
- [24] Choudhary V., Varma H. S., Varma I. K.: Effect of EPDM rubber on melt rheology, morphology and mechanical properties of polypropylene/HDPE (90/10) blend. 2. *Polymer*, **32**, 2541–2545 (1991).
DOI: [10.1016/0032-3861\(91\)90333-E](https://doi.org/10.1016/0032-3861(91)90333-E)
- [25] D’Orazio L., Mancarella C., Martuscelli E., Sticotti G., Massari P.: Melt rheology, phase structure and impact properties of injection-moulded samples of isotactic polypropylene/ethylene-propylene copolymer (iPP/EPR) blends: Influence of molecular structure of EPR copolymers. *Polymer*, **34**, 3671–3681 (1993).
DOI: [10.1016/0032-3861\(93\)90052-C](https://doi.org/10.1016/0032-3861(93)90052-C)
- [26] Chiang W-Y., Yang W-D., Pukánszky B.: Polypropylene composites. II: Structure-property relationships in two- and three-component polypropylene composites. *Polymer Engineering and Science*, **32**, 641–648 (1992).
DOI: [10.1002/pen.760321002](https://doi.org/10.1002/pen.760321002)
- [27] Manson J. A., Sperling L. H.: *Polymer blends and composites*. Plenum Press, New York (1976).
- [28] Bucknall C. B.: *Toughened plastics*. Applied Science Publishers, London (1977).
- [29] Prentice P.: Morphology of ethylene-propylene copolymers. *Polymer*, **23**, 1189–1192 (1982).
DOI: [10.1016/0032-3861\(82\)90377-9](https://doi.org/10.1016/0032-3861(82)90377-9)
- [30] Yeh P-L., Birley A-W., Hemsley D. A.: The structure of propylene-ethylene sequential copolymers. *Polymer*, **26**, 1155–1161 (1985).
DOI: [10.1016/0032-3861\(85\)90244-7](https://doi.org/10.1016/0032-3861(85)90244-7)
- [31] Wang L., Huang B.: Structure and properties of propylene-ethylene block copolymers and the corresponding blends. *Journal of Polymer Science Part B: Polymer Physics*, **28**, 937–949 (1990).
DOI: [10.1002/polb.1990.090280610](https://doi.org/10.1002/polb.1990.090280610)

- [32] Besombes M., Menguel J-F., Delmas G.: Composition analysis of an ethylene–propylene block copolymer by fractionation and turbidity measurements at the lower critical solubility gap. *Journal of Polymer Science Part B: Polymer Physics*, **26**, 1881–1896 (1988).
DOI: [10.1002/polb.1988.090260906](https://doi.org/10.1002/polb.1988.090260906)
- [33] Karger-Kocsis J., Kiss L., Kuleznev V. N.: Optical microscopic study on the phase separation of impact-modified PP blends and PP block copolymers. *Polymer Communications*, **25**, 122–126 (1984).
- [34] Tocháček J., Jančář J., Kalfus J., Zbořilová P., Buráň Z.: Degradation of polypropylene impact-copolymer during processing. *Polymer Degradation and Stability*, **93**, 770–775 (2008).
DOI: [10.1016/j.polymdegradstab.2008.01.027](https://doi.org/10.1016/j.polymdegradstab.2008.01.027)
- [35] Jiang T., Chen H., Ning Y., Kuang D., Qu G.: Study on morphology of high impact polypropylene prepared by in situ blending. *Journal of Applied Polymer Science*, **101**, 1386–1390 (2006).
DOI: [10.1002/app.22581](https://doi.org/10.1002/app.22581)
- [36] Nakatani H., Manabe N., Yokota Y., Minami H., Suzuki S., Yamaguchi F., Terano M.: Studies of thermal oxidative degradation of polypropylene impact copolymer using the temperature rising elution fractionation method. *Polymer International*, **56**, 1152–1158 (2007).
DOI: [10.1002/pi.2254](https://doi.org/10.1002/pi.2254)
- [37] Tan H., Li L., Chen Z., Song Y., Zheng Q.: Phase morphology and impact toughness of impact polypropylene copolymer. *Polymer*, **46**, 3522–3527 (2005).
DOI: [10.1016/j.polymer.2005.02.088](https://doi.org/10.1016/j.polymer.2005.02.088)
- [38] Chen Y., Chen Y., Chen W., Yang D.: Evolution of phase morphology of high impact polypropylene particles upon thermal treatment. *European Polymer Journal*, **43**, 2999–3005 (2007).
DOI: [10.1016/j.eurpolymj.2007.04.026](https://doi.org/10.1016/j.eurpolymj.2007.04.026)
- [39] Harding G. W., van Reenen A. J.: Fractionation and characterisation of propylene-ethylene random copolymers: Effect of the comonomer on crystallisation of poly(propylene) in the γ -phase. *Macromolecular Chemistry and Physics*, **207**, 1680–1690 (2006).
DOI: [10.1002/macp.200600242](https://doi.org/10.1002/macp.200600242)
- [40] Harding G. W., van Reenen A. J.: Polymerisation and structure–property relationships of Ziegler-Natta catalysed isotactic polypropylenes. *European Polymer Journal*, **47**, 70–77 (2011).
DOI: [10.1016/j.eurpolymj.2010.10.019](https://doi.org/10.1016/j.eurpolymj.2010.10.019)
- [41] Xu J., Feng L., Yang S., Wu Y., Yang Y., Kong X.: Separation and identification of ethylene-propylene block copolymer. *Polymer*, **38**, 4381–4385 (1997).
DOI: [10.1016/S0032-3861\(96\)01021-X](https://doi.org/10.1016/S0032-3861(96)01021-X)
- [42] Feng Y., Hay J. N.: The characterisation of random propylene–ethylene copolymer. *Polymer*, **39**, 6589–6596 (1998).
DOI: [10.1016/S0032-3861\(97\)10171-9](https://doi.org/10.1016/S0032-3861(97)10171-9)
- [43] Feng Y., Hay J. N.: The measurement of compositional heterogeneity in a propylene–ethylene block copolymer. *Polymer*, **39**, 6723–6731 (1998).
DOI: [10.1016/S0032-3861\(98\)00129-3](https://doi.org/10.1016/S0032-3861(98)00129-3)
- [44] Prasad J. V.: Characterization of propylene-ethylene block copolymers using solid state ^{13}C -NMR spectroscopy. *Journal of Polymer Science Part A: Polymer Chemistry*, **30**, 2033–2036 (1992).
DOI: [10.1002/pola.1992.080300929](https://doi.org/10.1002/pola.1992.080300929)
- [45] Cheng H. N.: Carbon-13 NMR analysis of ethylene-propylene rubbers. *Macromolecules*, **17**, 1950–1955 (1984).
DOI: [10.1021/ma00140a012](https://doi.org/10.1021/ma00140a012)